ABSTRACT

Effects of Nozzle Geometry and Extrudate Swell
on Fiber Orientation in Fused Deposition Modeling Nozzle Flow

Blake P. Heller, M.S.M.E.

Mentor: Douglas E. Smith, Ph.D.

Fused Deposition Modeling (FDM) is a rapidly growing Additive Manufacturing (AM) technology using extruded thermoplastics to produce intricate three-dimensional parts from digital data. Adding discrete fibers to FDM filament feedstock improves mechanical properties of FDM parts; however, little is known about processing and tooling effects on fiber orientation defined by velocity gradients within the polymer melt flow. This research simulates axisymmetric FDM extrudate swell extending from the nozzle exit by adjusting the radial location of the free surface to minimize the integrated free surface stress. Fiber orientation within the polymer melt is calculated from velocity gradients evaluated along streamlines in the fluid domain using orientation tensors, the fast exact closure, and isotropic rotary diffusion. Results quantify the influence of nozzle geometry and extrudate swell on fiber orientation in the extruded polymer. Parametric studies of nozzle geometry show sharp contractions in nozzle geometry near its exit significantly increases average fiber alignment.

A Study of the Effects of Nozzle Geometry and Extrudate Swell
on Fiber Orientation in Fused Deposition Modeling Nozzle Flow

by

Blake P. Heller, B.S.

A Thesis

Approved by the Department of Mechanical Engineering

_____

William Jordan, Ph.D., Chairperson

Submitted to the Graduate Faculty of
Baylor University in Partial Fulfillment of the
Requirements for the Degree
of

Master of Science in Mechanical Engineering

Approved by the Thesis Committee

_____

Douglas E. Smith, Ph.D., Chairperson

_____

David A. Jack, Ph.D.

_____

Ian Gravagne, Ph.D.

Accepted by the Graduate School

August 2015

_____

J. Larry Lyon, Ph.D., Dean

Page bearing signatures is kept on file in the Graduate School.

Copyright © 2015 Blake P. Heller

All rights reserved

TABLE OF CONTENTS

LIST OF FIGURES

LIST OF TABLES

ACKNOWLEDGMENTS

I would like to first thank my advisor Dr. Douglas Smith for all of his support and guidance through this project. As well I would like to thank Dr. David Jack for his help in answering my many questions, and for the use of his MATLAB code for the calculation of fiber orientation. I would like to also thank Dr. Ian Gravagne for his willingness to be a member of my thesis committee and for his help on the improvement of the thesis content. A special thanks goes to all of my office mates that keep the office environment as stress free and lighthearted as possible. Last, I would like to thank my wife and family for all their support and understanding for the long hours I have spent away to complete this work.

DEDICATION

To my loving wife who
has supported and kept me focused through all my endeavors

CHAPTER ONE

Introduction

1.1 Research Objective and Motivation

Fused Deposition Modeling (FDM) is perhaps the fastest growing technology in the area of Additive Manufacturing (AM). Additive manufacturing is defined as any process that uses only the addition of materials to build a finished part. The greatest attribute of additive manufacturing is intricate three dimensional parts can often be created using less material and energy without the need for tooling or molding devices. Materials used in additive manufacturing vary greatly and include, metals, plastics, concrete, and eventually human tissue. All additive manufacturing processes use a similar structure for the creation of parts from digital data. Users can create essentially any part using a Computer Aided Design (CAD) software such as SolidWorks (Dassault Systems, LLC, Velizy, France), PTC Creo (PTC, Inc.,Needham, MA), or AutoDesk Inventor (Autodesk, Inc., San Rafael, CA). A solid model is saved as an .stl file, which stands for a "stereolithography" file, which divides the given part into a number of triangular components that define the surface of the object. The respective software will then translate the .stl file into a series of layers that define the designed part.

There are many types of additive manufacturing technologies, but undoubtedly the most popular techniques are Selective Laser Sintering (SLS), Stereolithography

(SLA), Laminated Object Manufacturing (LOM), and Fused Deposition Modeling (FDM) [1].

Selective Laser Sintering (SLS) is an AM technique which consists of a sealed chamber of powdered material with a window over the printing platform. A laser is positioned above the window and the beam is directed towards the material platform. The material in the chamber is brought to a temperature slightly below its melting point and spread over a plate in a thin layer. The laser is then directed to selective positions which increases the temperature of the material above its melting point. Part shape is defined by the location of laser exposure. This is done successively until the part has been completed. The benefits of SLS printing are that plastics, metals, and ceramics can all be printed and printing is performed with high dimensional accuracy. Disadvantages of SLS printing include a final part having a porous structure and a large amount of material waste during processing.

Stereolithography (SLA) uses a liquid material bath that is exposed to the beam of a UV laser in select locations. The solidified liquid is built layer by layer until the part is complete. The benefits of SLA printing are fast print times with high dimensional accuracy and little material waste. Disadvantages of SLA printing include low material strength, poor thermal properties, and comparatively high material costs. Another major issue with SLA printing is photopolymer printing materials can contain up to 100 times the heavy metal (Antimony) content of other polymers which could lead to environmental and health concerns [2].

Laminated Object Manufacturing (LOM) is an AM technique in which separate layers of an adhesive coated material are glued together and cut to a specified shape using

a knife or laser. The benefits of LOM are low cost of materials and relatively large parts can be made easily. The issues of LOM include a low dimensional accuracy in comparison to other AM methods and the need for post processing.

Fused Depostion Modeling (FDM) is an AM technology that uses a filament based feedstock. This feedstock is fed into a liquefier, melted, and then extruded as a bead onto a moving platform. The platform moves in the plane perpendicular to and relative to the extrusion nozzle to create a single layer. The platform then is moved away from the nozzle as successive layers of plastic material are deposited. Material deposition is repeated layer by layer to create the final part. FDM printing uses G-code, which is numerical information passed from a computer to the printer, to define the print paths necessary to create the final part from the .stl file. The advantages of FDM printing are the ability to scale the technology for creation of large parts, low cost part production, and the use of industrial grade environmentally stable printing materials. Disadvantages of FDM printing include interlayer voids caused by the extrusion of parallel cylindrical polymer beads, interlayer adhesion problems seen between molten polymer layers and previously deposited partially cooled polymer layers, warping and delamination's due to thermal gradients in the printed part, and the overall strength of a part printed with a virgin polymer.

The research in this thesis addresses how the virgin polymer product can be enhanced by the introduction of discrete fiber reinforcement. The addition of discrete fiber reinforcement is by no means a new topic to the world of reinforced polymers, but can aid in the effectiveness of FDM printing as an emerging additive manufacturing technology. The addition of discrete fibers has been shown to improve material properties

of a virgin polymer. The material properties affected by the addition of discrete fibers include an increase in elastic modulus, toughness, and total strength. Specifically, the addition of carbon fibers to the virgin polymer will decrease the amount of warping and delamination's in the printed part [3].

To assess the value of adding discrete fibers to the polymer melt, the orientation of the discrete fibers must be calculated. Calculation of the orientation of discrete fibers in various fluids and suspensions (Newtonian and Non-Newtonian dilute, semi-dilute, and concentrated suspensions) have been previously calculated by many researchers [4, 5, 6, 7, 8] and is well understood. Work has gone into calculating the motion of a single fiber in the polymer melt flow [9, 10], two fibers [11], and multiple fibers [7].

To properly define the final fiber orientation state in a finished part we must consider two factors related to the FDM manufacturing process. The first factor to consider is the extrudate swell phenomena. As a fluid passes from a pressurized vessel to a free jet there is a natural expansion of the fluid. This expansion is called die, or extrudate, swell which causes a change in the velocity in both the radial and longitudinal directions of the flow seen as a swell of the fluid at the exit of the nozzle. Expansion flow such as that occurring in extrudate swell has been shown to decrease the alignment of the fibers in the direction of the flow and increase the alignment transverse to the flow [42, 43, 44] which is studied further in this thesis. The other factor to consider relates to the nozzle convergence zone upstream from the nozzle which effects the flow of plastic during processing. Prior research and results in the current research shows that fiber orientation changes considerably in expansion and contraction flows. The change in the velocity gradients in these areas causes the orientation of the fibers to rapidly align with

the flow of the polymer. Another consideration necessary in the modeling of the extrudate swell and fiber orientation is the boundary conditions at the point of initial expansion. The fluid undergoes major changes as it transitions from the no-slip boundary within the nozzle to the free surface no stress boundary outside of the nozzle exit. This change in boundary condition creates a singularity in the velocity field in the problem that cannot be avoided. The effect of the singularity on the final free surface stress can only be minimized not completely removed. Several researchers have previously developed their own approach to reducing the effects of the singularity [12, 13, 14].

Nixon et al. [15] originally modeled the fiber orientation in an FDM nozzle problem using Moldflow (Moldflow Corporation, Framingham, Massachusetts) which is a stand-alone injection molding software with fiber orientation calculation capabilities. The problem presented by Nixon et al., was modeled as a carbon micro fiber (CMF) filled fluid being injected into an open mold until the mold is 99.9% filled. The author states "[P]ost-nozzle, fibers tend to be aligned similarly in the global perspective. However, these results are meaningless due to the lack of material cooling once the material has been ejected from the nozzle as well as the lack of open-air boundary condition that would be present in a realistic FDM process." The work done for the current thesis defines the free jet surface and its effect on the resultant fiber orientation as well as the effect of an FDM nozzle geometry. Also a more in depth study and discussion of the effects of the nozzle geometry and the calculated free jet surface on the final fiber orientation state will be presented.

The goal of this thesis is to provide a model for the calculation of fiber orientation through the FDM nozzle fluid domain. The extrudate swell is calculated using a

minimization technique to zero the stress along the free surface boundary extending from the nozzle exit. The fiber orientation is then calculated through an axisymmetric representation of the full fluid domain which includes the nozzle geometry and calculated extrudate swell regions. Fiber orientation in the fluid domain is calculated using orientation tensors popularized by Advani-Tucker [10] with the Fast Exact Closure [17] assuming Folgar-Tucker [7] isotropic rotary diffusion. A study of the effects of changes in the nozzle geometry is then completed to define in more depth the effect of each portion of the nozzle (convergence zone, straight tube, and exit expansion). The calculations run in the following thesis define the effects of nozzle geometry and extrudate swell on the resultant fiber orientation.

1.2 Order of Thesis

Chapter One presents an overview of the research task to be approached and the overall objective of the presented thesis. Chapter Two discusses the literature that has been previously published pertaining to the established numerical and analytical models that effect the research topic discussed in the thesis. Chapter Three presents the method and implementation used to properly define the extrudate swell free jet surface for a straight tube and a FDM nozzle. Chapter Four gives the models used to calculate fiber orientation in the straight tube and FDM nozzle, as well as how the nozzle shape and extrudate swell affects the resultant fiber orientation. The results and conclusions from the fiber orientation models are also discussed. Chapter Five provides a parametric study of the effects of nozzle geometry on the average final orientation state of the extruded polymer bead. Lastly the thesis will conclude with Chapter Six which includes results and

discussion about the findings of the research, the applicability to current FDM processes, and recommendations for future work.

CHAPTER TWO

Literature Review

Fused Deposition modeling is a method of rapid prototyping that has great potential for many uses in the industrial field. Due to how new the field of fiber reinforced FDM research is there is a small amount of literature that pertains to this thesis, but the interesting and applicable information will be addressed here. There is, on the other hand decades of literature on the subject of extrudate swell and fiber orientation to be reviewed and discussed. To properly define the orientation of fibers flowing in a polymer melt, through a FDM extrusion nozzle, there must be a thorough understanding of all factors that affect that this fiber filled melt. Properly defining the die swell is pivotal to the understanding of the polymer jet extruded by the FDM nozzle. The exact values of the extrudate swell for Newtonian and Non-Newtonian fluids are important in the design and manufacturing of extrusion dies. For this reason die swell, also known as extrudate swell, has been studied extensively for the last fifty years. An overview of the analytical and numerical models defining extrudate swell and fiber orientation as well as the associated strengths and weaknesses of the accepted models is discussed below.

2.1 Fused Deposition Modeling in Additive Manufacturing

There is a wide variety of Rapid Prototyping (RP), more recently referred to as, Additive Manufacturing (AM), technologies that are currently used in industry. Selective Laser Sintering (SLS), Stereolithography (SLA), Digital Laser Metal Sintering (DLMS),

Laminated Object Manufacturing (LOM), and Fused Deposition Modeling (FDM) are the most popular RP methods [1]

The most popular and perhaps the most promising method is Fused Deposition Modeling [18]. The low material cost and ability to create intricate three dimensional shapes make this technology an exciting additive manufacturing technique. While being a promising prospect there are many issues with FDM printing that still need to be addressed. These issues include interlayer adhesion, interlayer voids, warping, delaminations, and unsatisfactory material properties for virgin polymers used in printing. The main areas that have been researched thus far are print parameter optimization and the addition of second phase particles to increase the mechanical properties of the print material.[18, 19]

2.1.1 Print Parameter Optimization

Print parameter research seeks to optimize the major variables in the printing process to improve mechanical properties, efficiency of the machines, and quality of the final printed part. This allows for increase in viability of FDM printing as an effective industrial tool. Thrimurthulu et al.[20] studied two major print parameters. The first parameter was print path optimization which seeks to decrease print times by decreasing the number of passes per layer and selection of the most effective print path. The second parameter looks at the effect of layer thickness on the surface finish of the part. The author minimizes a weighted sum of the print time and surface roughness to optimize the final print properties of the part depending on the preference of the print job. A weight of 1 for print time would use the largest layer thickness and shortest print paths to complete

the part as fast as possible while a weight of 0 would focus on the best possible surface finish. Other studies, such as the study by Sood et al. [21], seeks to increase the mechanical properties of the printed part by optimizing print parameters. The studied print parameters and definitions taken from Sood et al. [21] are given as:

- Orientation: Part build orientation or orientation refers to the inclination of part in a build platform with respect to X, Y, Z axis. X and Y axis are considered parallel to the build platform and Z axis is along the direction of part build.
- Layer thickness – is a thickness of layer deposited by nozzle and depends on the type of nozzle used.
- Raster angle – is a direction of raster relative to the X axis of the build table
- Part Raster Width – is the width of raster pattern used to fill interior regions of part curves
- Raster to Raster Gap - is the gap between two adjacent rasters on the same layer

The optimization of the above factors allows for parts that have improved mechanical properties with better surface finishes and parts that are more viable for industry use. This research area is important to the progression of FDM printing, but due to its limited use in this thesis, will not be discussed further.

2.1.2 Addition of Second Phase Particles

The addition of second phase particles to the virgin print material to increase mechanical properties is of interest for this thesis. Increasing the mechanical properties such as, thermal conductivity, ductility, tensile strength, and toughness is a necessity to make FDM printed parts viable in industry. One major point that needs to be made is that the addition of the second phase particles can be problematic when the volume fractions become too great. This causes nozzle clogging, agglomerations, and other issues which result in a failure in the printed part [22, 19].

2.1.2.1 Thermal Conductivity

The purpose of increasing thermal conductivity of the printing material is to decrease the surface roughness of the printed part and increase the heat dissipation properties of the final printed parts. One of the major applications for FDM printing is the creation of part tooling for injection molding; therefore, decreasing surface roughness of the printed part and increasing the heat dissipation are major concerns. Heat buildup in the injection molding process decreases the efficiency of the mold and poor surface finish on the molded part are unwanted properties which are improved with an increased thermal conductivity.

A study conducted by Nikzad et al. [22] looked at the addition of copper and iron particles to virgin ABS. The copper and iron particles were included in sizes of 10μm and 45μm, and in volume fractions of 5%, 10%, 20%, 30%, and 40%. A noticeable change in thermal conductivity of the material was not seen below 20% volume fraction of copper particles and 30% volume fraction of iron particles. Above these volume fractions, Nikzad et al. reported an order of magnitude improvement in thermal conductivity which the authors attribute to "a break in the thermal resistance of ABS and the creation of conductive chains in the matrix." The authors also note that agglomerations can occur at too high of a volume fraction which can cause voids that reduce thermal conductivity. It is understood that these voids would also decrease the structural integrity of the printed part which is unwanted.

2.1.2.2 Strength and Toughness

The purpose of increasing the strength and toughness of the printing material is to create parts that can be load bearing, and stand up to fatigue and wearing in an industrial

setting. An approach to increasing the strength and toughness of virgin plastic is to add chopped fibers which act as a stronger second phase material.

A study conducted by Zhong et al. [23] evaluated the addition of chopped glass fibers to virgin ABS. The chopped glass fibers were added in 15, 20, 25, and 30 % by weight. The glass filled ABS was found to be brittle when extruded into the printing filament and therefore could not be wound onto a cylinder. The authors then studied the effects of the addition of LLDPE, PE, Hydrogenated Buna-N, and Ethylene-Ethyl-Acrylate (EEA) which is an elastomer. These substances were added to increase ductility and toughness of the printing material so it could be extruded into a filament that could be wound. It was found that addition of Buna-N and LLDPE to the glass filled ABS allowed for a filament that was ductile enough to be wound. Zhong et al. showed that this combination of materials allowed for the inclusion of chopped glass fibers which increase the strength of the printing material.

Another study conducted by Tekinalp et al. [19] looked at the addition of chopped carbon fibers to virgin ABS. The chopped carbon fibers with an average length of 3.2 *mm* were added to the ABS in 10, 20, 30, and 40 % by weight. The carbon fiber filled ABS was then printed into dog-bones for tensile testing with the deposition direction being parallel to the load direction. After tensile testing the dog-bone specimens to failure the fracture surface of the dog-bone specimens were imaged with an SEM to study the fiber orientation in the printed part. Three major effects were seen on the fracture surfaces. The first effect, triangular voids between beads, was a known occurrence in FDM printing. The authors do state that as the carbon fiber weight percentage increases the size of the triangular voids decrease. This is said to be a result of increasingly lower extrudate swell

values and higher thermal conductivity as carbon fiber content increases. The second effect seen is void formation inside of the polymer bead around the chopped fibers. This type of void or pore formation increases along with the fiber weight percentage. This is said to be a result of the fiber and polymer phases flowing partially independently during extrusion. The last effect seen is high fiber breakage and high fiber alignment in the bead. The authors conclude that the high fiber breakage is attributed to high shear forces in the extrusion process, which also causes the high rate of alignment of the fibers. The authors state that even with the void formations and porosity there is a large increase of strength with the addition of chopped carbon fibers which gives the material "great potential for use in manufacturing of load bearing composite parts." [19] The high alignment of fibers oriented in the direction of the flow is of specific interest to the materials studied in this thesis.

2.1.3 Fiber Orientation Calculation

The fiber orientation within a FDM printed part will define the structural and mechanical properties. The fiber orientation in the polymer bead that is exiting the FDM extrusion nozzle is therefore of interest for the design and creation of load bearing parts. A highly aligned fiber orientation like the one presented by Tekinalp et al. [19] allows for high strength in the direction of fiber alignment, but little to no increase in strength transverse to the fiber alignment. A good understanding of how the extrusion nozzle effects the fiber orientation is critical in the nozzle design and mechanical expectations of a printed part.

A study by Nixon et al. [15, 16] first considered the effect of nozzle exit shape on the fiber orientation in FDM polymer melt flow. Moldflow (Moldflow Corporation,

Framingham, Massachusetts), which employs the Folgar-Tucker isotropic rotary diffusion model [7] and the ORL fourth order orientation tensor closure [24], was used for this study. Three nozzle geometries (convergent, short straight, and divergent) were considered in addition to volumetric ejection rate and volumetric fill fraction. Volumetric flow rates used in this study are 1.207, 1.448, and 1.810 $\frac{\mathrm{cm}^3}{\mathrm{s}}$ and the volumetric fiber fill fractions are 0, 10, and 20%. The author runs 27 simulations to exhaust all given possibilities then reports findings for the 10% and 20 % volumetric fill fractions. The author finds that fiber orientation in the liquefier/plenum sees little change until it reaches the area immediately before the nozzle. In this region the authors state that higher velocity gradients cause the fibers to align with the flow and that both percent fiber fill fraction and ejection rate increase the fiber alignment pre-nozzle. Finally the author reports that the convergent nozzle sees high in nozzle fiber alignment while the divergent nozzle sees a large decrease in the fiber alignment due to expansion flow. The author did not comment on the fiber orientation after the nozzle exit. Due to the fluid being shot into a large open mold rather than a free jet into open air the results were deemed meaningless.

Nixon et al. presents a significant first step in modeling fiber orientation in FDM printing, but there are definitely improvements needed before a full understanding of the process is gained. For example, the free surface calculations to define the polymer extrudate geometry is a focus this thesis. In addition a more in-depth investigation related to the fluid flow and fiber orientation is considered in the current work.

2.2 Extrudate Swell

The extrudate swell phenomena seen at the exit of an extrusion nozzle when the polymer melt becomes a free-stream fluid jet has yet to be analyzed for FDM printing. The free surface boundary must be properly defined to accurately model the FDM nozzle fluid domain. The flow of a polymer melt within a die and the related extrudate swell has been studied for many years as related to manufacturing processes, and a good understanding of the proper definition of the free surface has been reached. Extrudate swell is defined as the partial elastic recovery or swelling effect of an elastic fluid back to its former shape and volume at the exit of an extrusion nozzle or die assembly. The polymer melts' elastic nature is inhibited by the compression undergone in an extrusion nozzle or die assembly; therefore, when the polymer melt exits the compressed cavity and becomes a fluid jet with free surfaces it swells to its former shape and volume. The extent of the swelling depends on the fluid properties for each fluid and external conditions that the fluid is exposed to after exiting the die. The amount of swelling that the fluid undergoes will also affect the final physical and mechanical properties of the extruded product. [25]

2.2.1 Calculation of Extrudate Swell

An interesting aspect of extrudate swell that was introduced by Tanner [26] is that there are two different portions of the extrudate swell. There is an initial large expansion close to the die or extrusion exit then farther from the exit there is a region of smaller swell. It is said that the secondary swell can be neglected in calculations due to the rate and value of the swell being small in comparison with the initial swell. When modeling the die swell there are several assumptions that Tanner states and that are used in this

thesis. The assumptions are (a) the flow is isothermal and incompressible, (b) the die is long with a length/diameter>>1, (c) inertial effects in the flow may be ignored, (d) gravity, other body forces, and surface tension forces are ignored, so that the final extruded rod is load free, (e) the small, slow recovery far from the die is ignored [26]. Using these assumptions Tanner [27] defines an equation for the die swell of a viscoelastic fluid which is given as

$$\frac{D}{d} = \left[1 + \frac{1}{2}\left(\frac{N_1}{2\tau_w}\right)\right]^{\frac{1}{6}} + 0.13 \tag{2.1}$$

where N_1 is the first normal stress difference at the wall of a long circular tube, d is the diameter of the extrusion tube, τ_w is the wall shear stress, D is the diameter of the extrudate emerging from the extrusion tube, and the factor 0.13 is an addition to account for the swelling observed in inelastic Newtonian fluid in creeping flow [27]. For a Newtonian fluid the first normal stress, N_1, difference is zero [28] which causes $\frac{D}{d}$ in equation (2.1) to become simply $\frac{D}{d} = 1.13$.

Creeping flow of a compressible fluid is defined by the continuity and momentum which are respectively given as

$$\nabla \cdot \rho\mathbf{v} = 0 \tag{2.2}$$

$$\rho\mathbf{v} \cdot \nabla\mathbf{v} - \nabla \cdot \boldsymbol{T} = 0 \tag{2.3}$$

where ρ is the fluid density, $\mathbf{v}$ is the velocity vector, and $\boldsymbol{T}$ is defined as

$$\boldsymbol{T} = -p(\rho)\boldsymbol{I} + \mu[(\nabla\mathbf{v}) + (\nabla\mathbf{v})^{\mathrm{T}}] - \frac{2}{3}\mu\boldsymbol{I}\nabla \cdot \mathbf{v} \tag{2.4}$$

In the case of incompressible flow ρ is constant and the $-\frac{2}{3}\mu\boldsymbol{I}\nabla \cdot \mathbf{v}$ term of equation (2.4) goes to zero. Also for the case of a Newtonian fluid, μ is constant. For the

work done in this thesis we are concerned with only the Newtonian term which shows a flow expansion of 0.13 or 13%. A Non-Newtonian fluid has a greater expansion value than the Newtonian fluid and will vary for different fluid properties due to shear rate dependence. This value has been found to be accurate by several different numerical simulations. The first study considered is the work done by Georgiou et al, which defines the stick-slip free surface problem that represents an axisymmetric fluid jet exiting a die or extrusion tube [29]. Georgiou defines the problem as is seen in Figure 2.1.

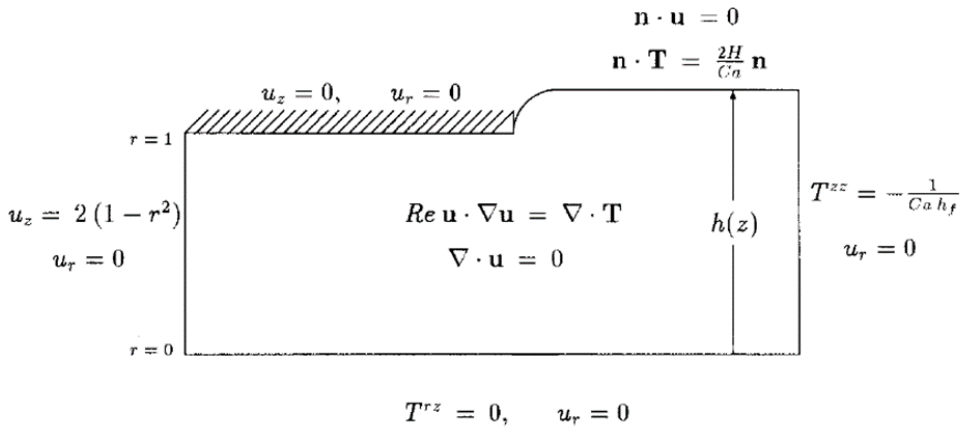

Figure 2.1. Axisymmetric Die Swell Flow Domain with Boundary Conditions from Georgiou [30]

The finite element method may be used to solve the fluid flow problem in Figure 2.1 in two dimensions, or the two-dimensional axisymmetric problem having the center of the flow channel as the axis of symmetry. In the latter case, the bottom boundary line Figure 2.1 is the line of axis symmetry. The wall with hashed lines is defined as a no slip boundary. The inlet fluid velocity is a parabolic flow representative of laminar flow with maximum velocity at the axis of symmetry and minimum velocity at the no slip upper boundary. The swell boundary is defined by $\mathbf{n} \cdot \mathbf{v} = 0$ which says that no fluid is passing

through the defined free boundary. The swell boundary is also defined by setting the stress vector along the boundary equal to zero which is defined as

$$\boldsymbol{T}:[\mathbf{n}\,\mathbf{n}] = 0 \tag{2.5}$$

where **n** is the normal vector along the boundary:

$$\mathbf{n} = \begin{bmatrix} n_r \\ n_\theta \\ n_z \end{bmatrix} \tag{2.6}$$

and $\boldsymbol{T}:[\mathbf{n}\,\mathbf{n}]$ is the double contraction of the stress tensor with the normal vector defined as the stress traction along the free surface. The outlet is defined as no fluid is flowing radially and the fluid is passing freely through the outlet boundary with zero stress in the z-direction. Solving the problem defined above for a round tubular channel with the finite element method, Georgiou [29] predicted a die swell of 13% for a Newtonian fluid. He also discovered that there is a particular rate of expansion, defined by the slope of the curve shown in Figure 2.2, and therefore a well-defined shape to the swell which is used as a benchmark later in the study.

Georgiou [29] also studied the effect of fluid compressibility on the final extrudate swell. He showed that compressibility can affect the overall swell value for a given fluid where die swell ranged from 11-13% depending on the amount of compressibility of the fluid. Georgiou [30] also presents the effectiveness of singular finite elements at the die exit, which will be discussed in the following section. Georgiou states that Salamon et al. experimentally determined a die swell value of 1.1291, which agrees well with Georgiou's calculated values for Ca = 1. Where Ca is the capillary number which is a dimensionless quantity that represents a relationship between the viscous and surface tension forces.

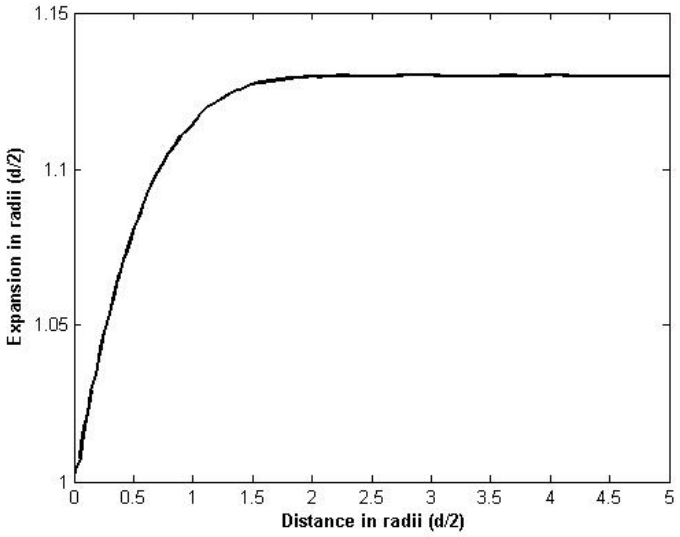

Figure 2.2. Magnitude and Shape of the Extrudate Swell from Georgiou [29]

Reddy and Tanner [31] found that minimizing the stress along the boundary using a finite element approach could be used to determine the extrudate swell of a free surface. A quadrilateral mesh is used with 20 degrees of freedom per element. Reddy and Tanner also consider the effects of increasing the Reynolds number on the extrudate swell. The authors show that at higher Reynolds numbers the effect of surface tension becomes negligible.

Elwood et al. [32] used three dimensional streamlined finite elements to predict a 14% swell for an incompressible Newtonian fluid from a round tubular channel. He also predicted that there is no swell at the corners of a square die but a contraction of the fluid at the die exit. Contrary to previous works Elwood et al. [32] considers the effects of a flat wall on the die swell versus an annular die shape. He also predicts that the flat wall will create 19% swell which is substantially greater than the 14% previously defined. Elwood [32] states that the solution to the extrudate swell can be calculated with three types of free surface boundary conditions (kinematic, normal stress, or shear stress). The

kinematic approach is used by Georgiou [29] where the surface stress state is neglected, Tanner [26] uses the shear stress approach to define the free surface, and Reddy and Tanner [31] use the normal stress approach. Elwood also states, body forces due to gravity cause a decrease in swell of the free surface when included in the model.

From the above papers it is found that the die swell is highly dependent on the flow conditions that the fluid undergoes. Several studies have looked at the effect of different flow parameters on the amount of swell seen by the fluid. Mitsoulis et al. [33] predicts that for creeping flow of a Newtonian fluid the die swell can vary from -90% to +56% by changing factors affecting the flow. These factors include Stokes Number (St), Reynolds number (Re), capillary number (Ca), compressibility (B), pressure-shift coefficient (B_p), and slip coefficient (B_{sl}). The extremes of -90% swell and +56% swell come from unlikely flow parameters for normal processing such as highly gravity or inertial driven flow and highly compressible fluids, but it does show the large effect that the parameters can have on the resultant die swell. These factors do not affect the problem evaluated in this thesis. The assumptions used in this thesis and by Tanner [27] eliminate the influence of B, B_p, B_{sl}, and St and sets Re and Ca in ranges that do not affect the extrudate swell.

2.2.2 Stick-Slip Singularity

Another factor that affects the calculation of die swell relates to singularities in the flow field. The occurrence of a singularity in the finite element problem for the velocity-pressure formulation of creeping flow has been well documented, as well as the approaches to dealing with the inherent singularity. Georgiou [12] determined that singular finite elements that map the shape of the singularity can be used to improve

convergence with fewer elements as compared to simply using standard finite elements. There are several types of singular finite element approaches presented in the paper which include embodied singularity elements, embedded singularity elements, and singular isoperimetric elements. Georgiou [13] employs embodied finite elements which embody specific shape functions to represent the singularity field. In his approach the singular finite elements are only used in the area immediately surrounding the stick slip singularity point. Using this method Georgiou claims a substantial decrease in the number of elements needed for similar or better convergence.

Another approach to properly assessing the singularity is discussed by Finlayson [14] who uses COMSOL Multiphysics (COMSOL, Stockholm, Sweden) to address the singularity issue. Finlayson claims by the use of Petrov-Galerkin stream wise up-winding and the Discrete Elastic-Viscous-Split-Stress (DEVSS) method a viscoelastic fluid can be modeled with the stick slip boundary conditions. The SUPG method smooths the velocity gradients at the singularity, by averaging upstream and downstream velocity gradient values. Using this method Finlayson sustains acceptable answers without requiring the specialty elements developed by Georgiou [12, 13].

The literature discussed above indicates that various methods have been developed to address the singularity that occurs at the stick-slip point. The singularity effects the evaluation of stress along the swell boundary and the ability eliminate the stress by adjusting the shape of the free surface. This effect will be seen later in the thesis.

2.3 Fiber Orientation

Fiber orientation models are used to compute the direction of fibers or groups of fibers suspended within a moving fluid. These models have seen extensive development and application in extrusion, and injection and compression molding over the past several decades. Fiber orientation models are widely used in commercial software packages such as Moldflow (Moldflow Corporation, Framingham, MA) and Moldex3D (Core Tech Systems Co., Ltd., Chupei City, Taiwan).

2.3.1 Fiber Orientation Models

The study of fiber orientation of a single inclusion suspended within a viscous fluid can trace its origins to work done by Einstein, [34] who modeled perfect spheres suspended in a viscous fluid. Jeffery [9] expanded Einstein's work on spheres to the periodic rotation of a single ellipsoidal fiber suspended in a viscous fluid. The first assumption made by Jeffery is that an ellipsoidal fiber rotates in a domain with no fiber boundary or fiber-fiber interaction. His derivation assumed that the ellipsoid is much smaller than the distance from the ellipsoid to the boundary or the distance to another ellipsoid. The suspended ellipsoid was also assumed to be under the influence of shear flow as well which causes the periodic tumbling motion of the fiber. From this paper we get the differential equation of motion for the direction of a fiber. Jeffery's differential equation can be written as [36]

$$\frac{D\mathbf{p}}{Dt} = \boldsymbol{\Omega} \cdot \mathbf{p} + \lambda(\boldsymbol{\Gamma} \cdot \mathbf{p} - \boldsymbol{\Gamma} : \mathbf{ppp}) \tag{2.7}$$

where $\mathbf{p}$ is the unit vector along the primary axis of the fiber with the components given as,

$$p_1 = \sin\theta\cos\varphi$$
$$p_2 = \sin\theta\sin\varphi \tag{2.8}$$
$$p_3 = \cos\theta$$

where θ and φ are angles defined in the coordinate system shown in Figure 2.3.

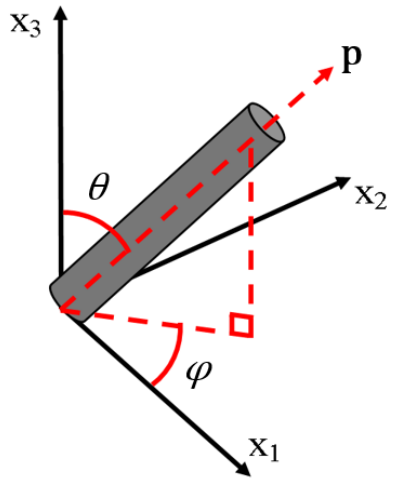

Figure 2.3. Coordinate System for a Single Fiber in Jeffery's Equation

In equation (2.7), λ is the coefficient related to fiber geometry,

$$\lambda = \frac{r_e^2 - 1}{r_e^2 + 1} \tag{2.9}$$

where r_e is the equivalent aspect ratio. In equation (2.7), $\boldsymbol{\Omega}$ is the vorticity tensor given as,

$$\boldsymbol{\Omega} = \frac{1}{2}[(\nabla\mathbf{v}) - (\nabla\mathbf{v})^{\mathrm{T}}] \tag{2.10}$$

and $\boldsymbol{\Gamma}$ is the rate of deformation tensor defined as

$$\boldsymbol{\Gamma} = \frac{1}{2}[(\nabla\mathbf{v}) + (\nabla\mathbf{v})^{\mathrm{T}}] \tag{2.11}$$

There are two main issues with Jeffery's approach to fiber orientation when applying it to discrete fiber polymer composites. The first is that for flows containing

more than one fiber Jeffery's equation would need to be calculated separately for each fiber which is inefficient. Folgar and Tucker [7] introduced the use of the probability distribution function, $\psi(\mathbf{p})$, which calculates the probability of a fiber being between θ_1 and $(\theta_1 + d\theta)$ and φ_1 and $(\varphi_1 + d\varphi)$. The second issue related to modeling discrete fiber composites relates the lack of a fiber-fiber interaction term. Fiber interaction for discrete fiber composites was first addressed by Folgar and Tucker [7] who introduced an Isotropic Rotary Diffusion function to account for fiber interaction. The rotary diffusivity term, D_r, was added to Jeffery's equation (Eq. (2.7)) to account for fiber-fiber interactions which limits the amount of fiber alignment. Folgar and Tucker recommended $D_r = C_I\dot{\gamma}$, where C_I is an empirically fit coefficient called the interaction coefficient and $\dot{\gamma}$ is the magnitude of the rate of deformation tensor given as

$$\dot{\gamma} = (\boldsymbol{\Gamma}:\boldsymbol{\Gamma})^{\frac{1}{2}} \tag{2.12}$$

where $\dot{\gamma} = (\boldsymbol{\Gamma}:\boldsymbol{\Gamma})^{\frac{1}{2}}$ is the double contraction of the rate of deformation with itself. The equation for a single fiber rotating in a concentrated suspension would then become [10]

$$\frac{D\mathbf{p}}{Dt} = \left(\boldsymbol{\Omega}\cdot\mathbf{p} + \boldsymbol{\lambda}(\boldsymbol{\Gamma}\cdot\mathbf{p} - \boldsymbol{\Gamma}:\mathbf{ppp})\right) - C_I\dot{\gamma}\frac{1}{\psi}\frac{d\psi}{d\mathbf{p}} \tag{2.13}$$

Computing the fiber orientation distribution function as a function of time can be computationally expensive. Therefore, it is common today to compute the moments of the distribution function which were first popularized for discrete fiber composites by Advani-Tucker [10]. Advani and Tucker [10] stated "orientation tensors are related to the coefficients of a Fourier series expansion of the probability distribution function." The differential equation for computing the time history of the second-order orientation tensor $\boldsymbol{A}$ is written as

$$\frac{D\boldsymbol{A}}{Dt} = -\frac{1}{2}(\boldsymbol{\Omega}\cdot\boldsymbol{A} - \boldsymbol{A}\cdot\boldsymbol{\Omega}) + \frac{1}{2}\lambda(\boldsymbol{\Gamma}\cdot\boldsymbol{A} + \boldsymbol{A}\cdot\boldsymbol{\Gamma} - 2\mathbb{A}\colon\boldsymbol{\Gamma}) + \boldsymbol{D_r} \tag{2.14}$$

where second and fourth order orientation tensors are defined respectively as

$$A_{ij} = \oint p_i p_j \psi(\boldsymbol{p})\, d\boldsymbol{p} \tag{2.15}$$

and

$$\mathbb{A}_{ijkl} = \oint p_i p_j p_k p_l \psi(\boldsymbol{p})\, d\boldsymbol{p} \tag{2.16}$$

The Advani-Tucker orientation tensor approach is an improvement on the calculation speed compared to that of the probability distribution function. Advani and Tucker [10] stated an increase of computation speed of two orders of magnitude, and it was shown later by Montgomery-Smith et al. [45] that an increase of up to four orders of magnitude was seen. When $\boldsymbol{D_r}$ is set equal to zero the above equation defines the Jeffery equation defined earlier. To account for fiber interaction, fiber orientation diffusion functions are employed. The Folgar-Tucker [7] Isotropic Rotary diffusion mentioned above was created to account for fiber interaction in concentrated fiber suspensions where there exists fiber-fiber interaction. The Folgar-Tucker diffusion function is given as

$$\boldsymbol{D_r^{IRD}} = 2C_I\dot{\gamma}(\boldsymbol{I} - 3\boldsymbol{A}) \tag{2.17}$$

The Folgar-Tucker Isotropic Rotary Diffusion (IRD) model has been widely used in industry, and is used by fiber orientation simulation programs such as Moldflow (Moldflow Corporation, Framingham, Massachusetts) and Moldex3D (Core Tech Systems Co., Ltd., Chupei City, Taiwan). The main problem with this orientation model is that there still exists an overestimate of the calculated fiber orientation rate of alignment in shear flow. To address this issue, various recent modifications have been

proposed that include the Reduced Strain Closure [8] (RSC) model, the Koch model [35], and the Anisotropic Rotary Diffusion (ARD) [36] model.

The reduced strain closure (RSC) method, introduced by Wang et al. [8] seeks to slow the orientation kinetics exhibited by short fiber polymer suspensions which tend to be over-predicted by the previously discussed models. The authors found that orientation of short fibers can range from two to ten times slower than is predicted by the Folgar-Tucker IRD model [8]. To slow the orientation kinetics but not affect the steady state solution the authors decrease the eigenvalue growth rate but do not disturb the rotation rate of the eigenvectors. The referenced eigenvectors and eigenvalues represent the symmetric second order orientation tensor as

$$\boldsymbol{A} = \sum_{i=1}^{3} \lambda_i \, \boldsymbol{e}_i \boldsymbol{e}_i \tag{2.18}$$

where $\boldsymbol{e}_i$ are the eigenvectors and λ_i are the eigenvalues. Given this representation of $\boldsymbol{A}$, it can be shown that Equation (2.14) becomes [8]

$$\begin{aligned} \frac{D\boldsymbol{A}}{Dt} = \; & (\boldsymbol{\Omega} \cdot \boldsymbol{A} - \boldsymbol{A} \cdot \boldsymbol{\Omega}) + \lambda\{\boldsymbol{\Gamma} \cdot \boldsymbol{A} + \boldsymbol{A} \cdot \boldsymbol{\Gamma} - 2[\mathbb{A} + (1-\kappa)(\mathbb{L} - \mathbb{M}\colon \mathbb{A})]\colon \boldsymbol{\Gamma}\} \\ & + 2\kappa C_I \dot{\gamma}(\boldsymbol{I} - 3\boldsymbol{A}) \end{aligned} \tag{2.19}$$

where $\mathbb{L}$ and $\mathbb{M}$ are analytical functions of the eigenvalues and eigenvectors of $\boldsymbol{A}$ which are defined respectively as

$$\mathbb{L} = \sum_{i=1}^{3} \lambda_i (\boldsymbol{e}_i \boldsymbol{e}_i \boldsymbol{e}_i \boldsymbol{e}_i) \tag{2.20}$$

and

$$\mathbb{M} = \sum_{i=1}^{3} \boldsymbol{e}_i \boldsymbol{e}_i \boldsymbol{e}_i \boldsymbol{e}_i \tag{2.21}$$

In the above, κ is a parameter that slows the orientation kinetics, chosen to fit experimental data. The authors state that the model reduces to the Folgar-Tucker IRD model when $\kappa \rightarrow 1^-$. These changes effectively reduce strain rate imposed on the orientation tensor; hence, the model is named the Reduced Strain Closure (RSC). This model has been an effective addition to the reduction of the rate of fiber orientation. The RSC method is also used in the Phelps-Tucker ARD-RSC model which is the most accurate model that currently exists for prediction of fiber orientation states.

The ARD and ARD-RSC models are presented by Phelps and Tucker. The ARD is defined as [36]

$$\boldsymbol{D}_r^{\boldsymbol{ARD}} = \dot{\gamma}[2\boldsymbol{C} - 2(\mathrm{tr}\,\boldsymbol{C})\boldsymbol{A} - 5(\boldsymbol{C}\cdot\boldsymbol{A} + \boldsymbol{A}\cdot\boldsymbol{C}) + 10\mathbb{A}\!:\!\boldsymbol{C}] \tag{2.22}$$

and the ARD-RSC is defined as [36]

$$\begin{aligned}\frac{D\boldsymbol{A}}{Dt}^{ARD-RSC} &= (\boldsymbol{\Omega}\cdot\boldsymbol{A} - \boldsymbol{A}\cdot\boldsymbol{\Omega}) \\ &+ \lambda\{\boldsymbol{\Gamma}\cdot\boldsymbol{A} + \boldsymbol{A}\cdot\boldsymbol{\Gamma} - 2[\mathbb{A} + (1-\kappa)(\mathbb{L} - \mathbb{M}\!:\!\mathbb{A})]\!:\!\boldsymbol{\Gamma}\} \\ &+ \dot{\gamma}\{2[\boldsymbol{C} - (1-\kappa)\mathbb{M}\!:\!\boldsymbol{C}] - 2\kappa(\mathrm{tr}\boldsymbol{C})\boldsymbol{A} - 5(\boldsymbol{C}\cdot\boldsymbol{A} + \boldsymbol{A}\cdot\boldsymbol{C}) \\ &+ 10[\mathbb{A} + (1-\kappa)(\mathbb{L} - \mathbb{M}\!:\!\mathbb{A})]\!:\!\boldsymbol{C}\}\end{aligned} \tag{2.23}$$

where **C** is a spatial tensor describing fiber-fiber interactions given by

$$\boldsymbol{C} = b_1\boldsymbol{I} + b_2\boldsymbol{A} + b_3\boldsymbol{A}^2 + \frac{b_4}{\dot{\gamma}}\boldsymbol{\Gamma} + \frac{b_5}{\dot{\gamma}}\boldsymbol{\Gamma}^2 \tag{2.24}$$

The Koch model [35] builds on the Folgar-Tucker Isotropic Rotary Diffusion model and adds the effect of long-range hydrodynamic fiber-fiber interactions. It is also an anisotropic model and depends on the fiber orientation state to calculate orientation diffusivity. This model was designed for semi-dilute fiber suspensions such that $nL^2d > 3$,

where n is the number of fibers per unit volume, L is the average fiber length, and d is the fiber diameter. The Koch anisotropic rotary diffusion model is defined as [35]

$$\boldsymbol{D}_{\boldsymbol{r}}^{\boldsymbol{Koch}} = \frac{nL^3}{\dot{\gamma}^2 \ln^2 \alpha}[\lambda_1(\boldsymbol{\Gamma}:\mathbb{A}:\boldsymbol{\Gamma})\boldsymbol{I} + \lambda_2(\boldsymbol{\Gamma}:\boldsymbol{\mathcal{A}}:\boldsymbol{\Gamma})] \tag{2.25}$$

where, $\alpha = L/d$ is the fiber aspect ratio, λ_1 and λ_2 are coefficients that are obtained by fitting the model to theoretical orientation distributions in extensional flows, and $\boldsymbol{\mathcal{A}}$ is the sixth order orientation tensor given as

$$\boldsymbol{\mathcal{A}}_{ijklmn} = \oint p_i p_j p_k p_l p_m p_n \psi(\boldsymbol{p})\, d\boldsymbol{p} \tag{2.26}$$

Phelps and Tucker [36] noted that for values of nL^2d sufficiently less than 3 A_{11} will rise above unity which is non-physical, and in the steady-state condition λ_1 which is the isotropic diffusion term dominates the anisotropic diffusion term λ_2 so that there is little difference between the Koch model and the Folgar-Tucker diffusion function which is more computationally efficient.

2.3.2 Closure Methods

A major issue in the use of the Advani-Tucker [10] orientation tensor approach is the need for a series truncation. The fiber orientation tensor approach is a Fourier series expansion of increasing even order orientation tensors (A_{ij}, $\mathbb{A}_{ijkl}$, $\boldsymbol{\mathcal{A}}_{ijklmn}$, ….) used to represent the fiber orientation distribution function. This series must be truncated at a certain point and a closure method must be used to calculate the highest order tensor using the lower order tensors. There are many different closure methods that have been proposed. The Hybrid Closure presented by Advani and Tucker [10] simply combines the linear [37] and quadratic [38] closure approximations. The linear closure approximation is simply a summation of all the products of $\boldsymbol{A}$ and δ.

$$\widehat{\mathbb{A}}_{ijkl} = -C_1\left(\delta_{ij}\delta_{kl} + \delta_{ik}\delta_{jl} + \delta_{il}\delta_{jk}\right) + C_2(A_{ij}\delta_{kl} + A_{ik}\delta_{jl} + A_{il}\delta_{jk} + A_{kl}\delta_{ij} + A_{jl}\delta_{ik} + A_{jk}\delta_{il}) \tag{2.27}$$

where C_1 and C_2 are constants defined respectively as $\frac{1}{35}$ and $\frac{1}{7}$ for three-dimensional orientation and respectively as $\frac{1}{24}$and $\frac{1}{6}$ for planar constrained orientation. The quadratic closure is defined as the product of the second-order orientation tensor defined as

$$\widetilde{\mathbb{A}}_{ijkl} = A_{ij}A_{kl} \tag{2.28}$$

The linear closure is exact for completely random fiber distributions while the quadratic closure is exact for fully aligned fibers. The hybrid closure combines the strengths of each method to compute the fourth-order orientation tensor as

$$\overline{\mathbb{A}} = (1-f)\widehat{\mathbb{A}} + f\widetilde{\mathbb{A}} \tag{2.29}$$

where *f* is an alignment parameter defined as

$$f = aA_{ij}A_{ji} - b \tag{2.30}$$

In this calculation, *a* and *b* are, respectively, $\frac{3}{2}$ and $\frac{1}{2}$for three-dimensional orientation and 2 and 1 for planar orientation. The hybrid closure is shown to provide a better model across the orientation spectrum than the two previous models.

The Orthotropic fitted closure presented by Cintra-Tucker [24] is based on the realization that all fourth order tensor approximations must be orthotropic which is obtained when its principal axes match those of the second order tensor from which the fourth order tensor approximation is computed. The Orthotropic Fitted Closure is computed as

$$\overline{\boldsymbol{A}}_{mm}^{ORF} = C_m^1 + C_m^2 a_1 + C_m^3 [a_1]^2 + C_m^4 a_2 + C_m^5 [a_2]^2 + C_m^6 a_1 a_2 \tag{2.31}$$

where m = 1,6. In equation (2.31) $a_1$and a_2 are the eigenvalues of the second order orientation tensor. There are 18 independent coefficients that are computed using a minimization process that fits computed values of $\boldsymbol{A}$ for various homogenous flow fields. The authors state that the orthotropic fitted closure (ORF) uses a similar approach as the Natural Closure presented by Verleye and Dupret [39]. It is stated that "the invariants and the principal values contain the same information and, if completely general functions were used, they would give identical closure results. The Natural Closure is defined as

$$\begin{aligned}\overline{\mathbb{A}}_{ijkl}^{Natural} = \ & \beta_1 S(\delta_{ij}\delta_{kl}) + \beta_2 S(\delta_{ij}A_{kl}) + \beta_3 S(A_{ij}A_{kl}) + \beta_4 S(\delta_{ij}A_{km}A_{ml}) \\ & + \beta_5 S(A_{ij}A_{km}A_{ml}) \ + \beta_6 S(A_{im}A_{mj}A_{kn}A_{nl})\end{aligned} \tag{2.32}$$

where S is the symmetric part of its argument, i.e.,

$$S = \frac{1}{24}(T_{ijkl} + T_{jikl} + T_{jkil} + \cdots) \tag{2.33}$$

The Invariant Based Optimal Fitting (IBOF) closure is a hybrid of the Natural and Orthotropic Fitted Closures that is presented by Chung and Kwon [40]. The natural and orthotropic closures are eigenvalue-based optimal fitting (EBOF) closure approximations. The IBOF closure is defined in the exact same way as the natural closure ($\overline{\mathbb{A}}^{Natural}$), except that the β_i values are calculated with a different procedure. For the IBOF it is considered that the β_i values are functions of the second and third invariants (II, III) of A_{ij}.

The Fast Exact Closure (FEC) by Montgomery-Smith et al. [17] is a computationally efficient version of the Exact Closure by Montgomery-Smith et al. [41]. The FEC is considered exact since it does not require a fiber interaction term ($\boldsymbol{D_r}$ = 0), resulting in the Jeffery equation being solved exactly. The FEC solves the following set of coupled ODEs simultaneously to find the fiber orientation state:

$$\frac{D\boldsymbol{A}}{Dt} = -\mathbb{C}\colon \boldsymbol{F}(\boldsymbol{B}) + \boldsymbol{G}(\boldsymbol{A}) \qquad \frac{D\boldsymbol{B}}{Dt} = \boldsymbol{F}(\boldsymbol{B}) - \mathbb{D}\colon \boldsymbol{G}(\boldsymbol{A}) \tag{2.34}$$

where $\mathbb{C}$ and $\mathbb{D}$ are rank four conversion tensors, and $\boldsymbol{F}(\boldsymbol{B})$ and $\boldsymbol{G}(\boldsymbol{A})$ are defined by the fiber orientation model that is being solved. The implementation of the fast exact closure for the Folgar-Tucker IRD model,

$$\frac{D\boldsymbol{A}}{Dt} = -\frac{1}{2}\mathbb{C}\colon [\boldsymbol{B}\cdot(\boldsymbol{\Omega} + \lambda\boldsymbol{\Gamma}) + (-\boldsymbol{\Omega} + \lambda\boldsymbol{\Gamma})\cdot\boldsymbol{B}] + D_r(2\boldsymbol{I} - 6\boldsymbol{A}) \tag{2.35}$$

$$\frac{D\boldsymbol{B}}{Dt} = -\frac{1}{2}(\boldsymbol{B}\cdot(\boldsymbol{\Omega} + \lambda\boldsymbol{\Gamma}) + (-\boldsymbol{\Omega} + \lambda\boldsymbol{\Gamma})\cdot\boldsymbol{B}) + D_r\mathbb{D}\colon(2\boldsymbol{I} - 6\boldsymbol{A}) \tag{2.36}$$

where the tensor $\boldsymbol{B}$ is a parameter of orientation defined similar to that of the orientation tensor $\boldsymbol{A}$, and $\mathbb{C}$ and $\mathbb{D}$ are fourth-order conversion tensors. The conversion tensors are calculated in the orthonormal basis of $\boldsymbol{B}$; therefore, b_1, b_2, and b_3 are the eigenvalues of $\boldsymbol{B}$ and a_1, a_2, and a_3 are the eigenvalues $\boldsymbol{A}$. $\mathbb{C}$ is a symmetric tensor defined as

$$\mathbb{C} = \begin{bmatrix} \mathbb{C}_{1111} & \mathbb{C}_{1122} & \mathbb{C}_{1133} & 2\mathbb{C}_{1112} & 2\mathbb{C}_{1113} & 2\mathbb{C}_{1111} \\ \mathbb{C}_{2211} & \mathbb{C}_{2222} & \mathbb{C}_{2233} & 2\mathbb{C}_{2212} & 2\mathbb{C}_{2213} & 2\mathbb{C}_{2223} \\ \mathbb{C}_{3311} & \mathbb{C}_{3322} & \mathbb{C}_{3333} & 2\mathbb{C}_{3312} & 2\mathbb{C}_{3313} & 2\mathbb{C}_{3323} \\ 2\mathbb{C}_{1211} & 2\mathbb{C}_{1222} & 2\mathbb{C}_{1233} & 4\mathbb{C}_{1212} & 4\mathbb{C}_{1213} & 4\mathbb{C}_{1223} \\ 2\mathbb{C}_{1311} & 2\mathbb{C}_{1322} & 2\mathbb{C}_{1333} & 4\mathbb{C}_{1312} & 4\mathbb{C}_{1313} & 4\mathbb{C}_{1323} \\ 2\mathbb{C}_{2311} & 2\mathbb{C}_{2322} & 2\mathbb{C}_{2333} & 4\mathbb{C}_{2312} & 4\mathbb{C}_{2313} & 4\mathbb{C}_{2323} \end{bmatrix} \tag{2.37}$$

where the components of $\mathbb{C}$ are calculated as

$$\begin{aligned} \bar{\mathbb{C}}_{1122} &= \frac{a_1 - a_2}{2(b_2 - b_1)} & \bar{\mathbb{C}}_{1111} &= \frac{1}{2}b_1^{-1} - \mathbb{C}_{1122} - \mathbb{C}_{1133} \\ \bar{\mathbb{C}}_{1133} &= \frac{a_1 - a_3}{2(b_3 - b_1)} & \bar{\mathbb{C}}_{2222} &= \frac{1}{2}b_2^{-1} - \mathbb{C}_{1122} - \mathbb{C}_{2233} \\ \bar{\mathbb{C}}_{2233} &= \frac{a_2 - a_3}{2(b_3 - b_2)} & \bar{\mathbb{C}}_{3333} &= \frac{1}{2}b_3^{-1} - \mathbb{C}_{1133} - \mathbb{C}_{2233} \\ \bar{\mathbb{C}}_{ijkk} &= 0 \; if \; i \neq j \neq k \end{aligned} \tag{2.38}$$

and $\mathbb{D}$ is defined as

$$\mathbb{D} = \mathbb{C}^{-1} = \begin{bmatrix} \mathbb{D}_{1111} & \mathbb{D}_{1122} & \mathbb{D}_{1133} & 2\mathbb{D}_{1112} & 2\mathbb{D}_{1113} & 2\mathbb{D}_{1111} \\ \mathbb{D}_{2211} & \mathbb{D}_{2222} & \mathbb{D}_{2233} & 2\mathbb{D}_{2212} & 2\mathbb{D}_{2213} & 2\mathbb{D}_{2223} \\ \mathbb{D}_{3311} & \mathbb{D}_{3322} & \mathbb{D}_{3333} & 2\mathbb{D}_{3312} & 2\mathbb{D}_{3313} & 2\mathbb{D}_{3323} \\ 2\mathbb{D}_{1211} & 2\mathbb{D}_{1222} & 2\mathbb{D}_{1233} & 4\mathbb{D}_{1212} & 4\mathbb{D}_{1213} & 4\mathbb{D}_{1223} \\ 2\mathbb{D}_{1311} & 2\mathbb{D}_{1322} & 2\mathbb{D}_{1333} & 4\mathbb{D}_{1312} & 4\mathbb{D}_{1313} & 4\mathbb{D}_{1323} \\ 2\mathbb{D}_{2311} & 2\mathbb{D}_{2322} & 2\mathbb{D}_{2333} & 4\mathbb{D}_{2312} & 4\mathbb{D}_{2313} & 4\mathbb{D}_{2323} \end{bmatrix} \tag{2.39}$$

The Phelps-Tucker ARD model is recast as

$$\frac{D\boldsymbol{A}}{Dt} = \frac{1}{2}\mathbb{C}\colon[\boldsymbol{B}\cdot(\boldsymbol{\Omega}+\lambda\boldsymbol{\Gamma})+(-\boldsymbol{\Omega}+\lambda\boldsymbol{\Gamma})\cdot\boldsymbol{B}]+2D_r+3(tr\boldsymbol{D_r})\boldsymbol{A}-5\mathbb{C}\colon(\boldsymbol{B}\cdot D_r+D_r\cdot\boldsymbol{B}) \tag{2.40}$$

$$\frac{D\boldsymbol{B}}{Dt} = -\frac{1}{2}(\boldsymbol{B}\cdot(\boldsymbol{\Omega}+\lambda\boldsymbol{\Gamma})+(-\boldsymbol{\Omega}+\lambda\boldsymbol{\Gamma})\cdot\boldsymbol{B})-\mathbb{D}\colon(2D_r+3(tr\boldsymbol{D_r})\boldsymbol{A})+5(\boldsymbol{B}\cdot D_r+D_r\cdot\boldsymbol{B}) \tag{2.41}$$

It is shown by the authors that the FEC is exactly accurate for $D_r = 0$, and otherwise is as accurate as the orthotropic fitting closures, and is much faster than most of the other current closure approximations. The major benefit of this closure is that it does not need to calculate or approximate the fourth order moment tensor $\mathbb{A}$.

2.3.3 Fiber Orientation in Expansion and Contraction Geometries

Fiber orientation in extrusion processes and in complex geometries has been studied for decades and is well understood for the common injection molding and extrusion processes. Studies have also been run that take into consideration abrupt changes in geometry and complex geometric shapes. These areas of research are of interest to the current study which aims to study fiber orientation through a nozzle with complex geometry and in an extruded polymer region.

VerWeyst and Tucker [42] study several common complex flow domains such as rapid expansion, a center gated disk, and a rapid contraction using the finite element method to model the respective flow domains. The model used in this study includes the use of a coupled fiber orientation-viscosity model which is of interest for future studies in the subject area of this thesis. The authors show that expansion and contraction flows

cause fibers to orient transverse to the original flow direction. Vortices in the corners of the expansion and contractions are also observed and are shown to increase in size and strength by the addition of chopped fibers. The effects of the vortices in the contraction and expansion flows have also been discussed by Lipscomb et al. [38] and Baloch and Webster [43] who solved the problem within an axisymmetric fluid domain. The decrease in fiber alignment is seen for all three flow types (rapid expansion, center gated disk, and rapid contraction) presented which would indicate we should see a loss of fiber alignment in the extrudate swell.

Yasuda et al. [44] evaluated the effect of abrupt expansion geometries on fiber orientation. The authors use an experimental approach to the fiber orientation study rather than the finite element modeling by VerWeyst and Tucker [42]. A flow channel was created with a 1:16 expansion and a 1:4 expansion. The flow channel was filled with a Newtonian fluid and cellulose acetate propionate (CAP) fibers. The fiber filled suspending fluid was then passed through the expansion domain for both the 1:16 and 1:4 expansions. The authors report that at the expansion the fibers quickly orient perpendicular to the radial flow and due to the quick orientation, effect the amount of fiber interaction for a semi-dilute fiber suspension.

The understanding of fiber orientation in expansions and contractions will be helpful in the definition of fiber orientation in the extrudate swell. Fiber orientation in an extrudate swell expansion flow and an FDM nozzle has yet to be studied. This thesis presents a calculation of the fiber orientation for the FDM nozzle geometry and extrudate swell domain extending from the FDM nozzle exit. From the research presented we

should expect an increase in orientation in the flow direction at contraction areas and a decrease in expansion areas.

CHAPTER THREE

Extrudate Swell

A method for calculating the extrudate swell free surface shape is developed in this chapter to define the entire fluid domain through which the fiber filled polymer melt will travel during the FDM deposition process. The free surface of the polymer melt outside of the nozzle exit is calculated using a minimization approach similar to the one used by Reddy and Tanner[14] which computed the shape of the free surface that minimized the normal and tangential stresses along the free surface. The stress calculation and minimization process is achieved using COMSOL Multiphysics (COMSOL, Stockholm, Sweden) and a custom code created in MATLAB (MathWorks, Inc., Natick, Massachusetts) through COMSOL LiveLink. The results of the stress minimizations are then discussed and compared to values in the literature for validation of the minimization technique. The following sections will present a deeper look at the extrudate swell calculation method used to define the extrudate swell free surface.

3.1 Extrudate Swell Theory

The finite element model used in the minimization function is defined as having the same geometry, similar boundary conditions, and the same two-dimensional axisymmetric problem presented by Tanner [11], Georgiou [13], and Reddy [15]. The use of a similar problem structure allows the results to be compared to a benchmark shape and value of the extrudate swell for validation of the method used in this study.

The flow of polymer melt through a nozzle and into free space is defined as creeping flow (i.e. a flow having a Reynolds number that is small compared to unity) of an incompressible Newtonian fluid. The continuity and momentum equations defining this flow are given respectively as

$$\nabla \cdot \mathbf{v} = 0 \tag{3.1}$$

and

$$\mathbf{v} \cdot \nabla \mathbf{v} - \nabla \cdot \boldsymbol{T} = 0 \tag{3.2}$$

where **v** is the velocity vector and $\boldsymbol{T}$ is the total stress tensor given as

$$\boldsymbol{T} = -p\boldsymbol{I} + \mu[(\nabla \mathbf{v}) + (\nabla \mathbf{v})^{\mathrm{T}}] \tag{3.3}$$

In Equation (3.3) p is the pressure, $\boldsymbol{I}$ is the identity matrix, μ is the viscosity, and superscript T is the transpose operator. The extrudate swell problem is defined using the geometry and boundary conditions appearing in Figure 3.1.

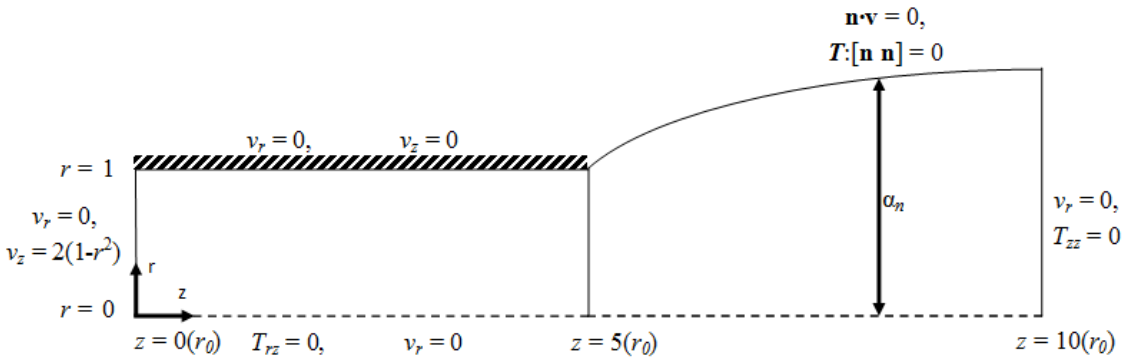

Figure 3.1. Extrudate Swell Model Geometry and Boundary Conditions

Georgiou concluded that a distance of 5 radii upstream and downstream from the extrusion exit is a sufficient length to ensure steady results. In this thesis, the diameter of a common desktop FDM printing extrusion nozzle being modeled is 0.35 *mm*; therefore, the radius is 0.175 *mm* for the given two-dimensional axisymmetric problems considered here. The swell boundary is defined with function r(z) which represents the free surface.

The boundary conditions appearing in Figure 3.1 define the fluid flow domain and boundary conditions required to solve the die swell problem. The bottom dashed boundary line in the figure is the line of axis symmetry. The axisymmetric model can be swept around this axis to represent the three-dimensional flow domain used in this study. The wall with hashed lines is the inner wall of the flow nozzle and is defined to have a no slip boundary condition ($v_z = 0$ and $v_r = 0$). The inlet fluid velocity is assumed to have a parabolic profile typical of a laminar tube flow of a Newtonian fluid with a maximum velocity at the axis of symmetry, and zero velocity at the no slip upper boundary. The inlet velocity equation may be written as

$$v_z^{inlet} = -v_{max}\left[1 - \left(\frac{r_{inlet}}{r_{max}}\right)^2\right] \tag{3.4}$$

where v_{max} is the maximum velocity at the inlet of the fluid domain, r_{inlet} is the radial location, and r_{max} is the maximum radius of the fluid domain at the inlet. The die swell boundary is defined as a slip wall where fluid adjacent to the wall is allowed to slip ($\underline{\mathbf{t}}\cdot\underline{\mathbf{v}} \neq 0$) where $\underline{\mathbf{t}}$ is the tangential velocity vector, and does not pass through the wall ($\mathbf{n}\cdot\mathbf{v} = 0$). The extrudate swell free surface boundary is also defined by $\boldsymbol{T}:[\mathbf{n}\ \mathbf{n}] = 0$, which provides that no fluid passes through or away from the boundary. The outlet is defined by a zero pressure which provides for a zero fluid stress along this surface.

3.2 Free Surface Defined

The approach to defining the shape of the free surface used in this work is similar to that used by Reddy and Tanner [14] and has proven to be a successful method. In previous work by Georgiou [13] and Mistoulis [16], an iterative process was used to zero the normal velocity along the free surface by moving points along the surface in the

radial direction. The approach described below, defines the free surface using various functions of radius along the length of the flow and computes parameters that define each function to minimize the stresses along the free surface. The minimized surface is then compared to solutions found in the literature that has been studied.

The free surface shape is defined using a radius function r, in terms of the independent spatial coordinate z. Values of $r_i(z_i)\ i = 1, \dots, n$, are specified along the length of the flow which are used to define an interpolating polynomial r(z) for the free surface. In the studies to follow, the radius r of the free surface of the axisymmetric extrudate swell is defined as the m^{th} order polynomial of the z coordinate as.

$$r(z) = a_0 + a_1 z + a_2 z^2 + a_3 z^3 + \cdots + a_n z^m \tag{3.5}$$

where the coefficients $a_0, \dots, a_n$ are derived for the following conditions:

- Expansion occurs over a length of z from 1 to 5 radii to match the model presented by Georgiou [29]
- The slope at the point of expansion end is zero, $\frac{dr}{dz} = 0$
- At $m - 1$ equally* spaced points along the curve a surface swell value is defined as αr_0
- For expansion lengths less than 5 radii a line with zero slope continues past the defined function.
- Other derivations are considered that do not have equally spaced points. In these cases, points are concentrated upstream toward the nozzle exit where the rate of expansion is greatest.

The highest order polynomial used in this study is a fifth order polynomial. Polynomials with order higher than 5 were considered, but were not used due to instabilities in the resulting fitted equation that occurred between defined points.

An exponential function was also considered in an effort to provide the best representation of the free surface shape. The exponential form used here is given as

$$r(z) = r_0 + \frac{1}{2}(\alpha - 1)\left[1 - e^{-\beta z\left(\frac{\ln(1-\alpha r_0)}{r_0}\right)}\right] \tag{3.6}$$

where α is the max expansion of the free surface, β is the coefficient that determines the rate of expansion, and r_0 is the initial radius of the fluid flow in the nozzle. The smooth growth of an exponential function appeared to be a good fit for possibly defining the extrudate swell shape. The exponential function as it is defined here could not reach the minimum stress state in the optimization process and therefore was not used in any of the results to follow. Because a sufficient answer could not be found with the exponential defined above and the ability to define the free surface repeatedly with a polynomial, only the polynomial function in equation (3.5) was used in this study. Five plots of the die swell expansion with typical die swell radius values appear in Figure 3.2 for the quadratic function in equation (3.6)

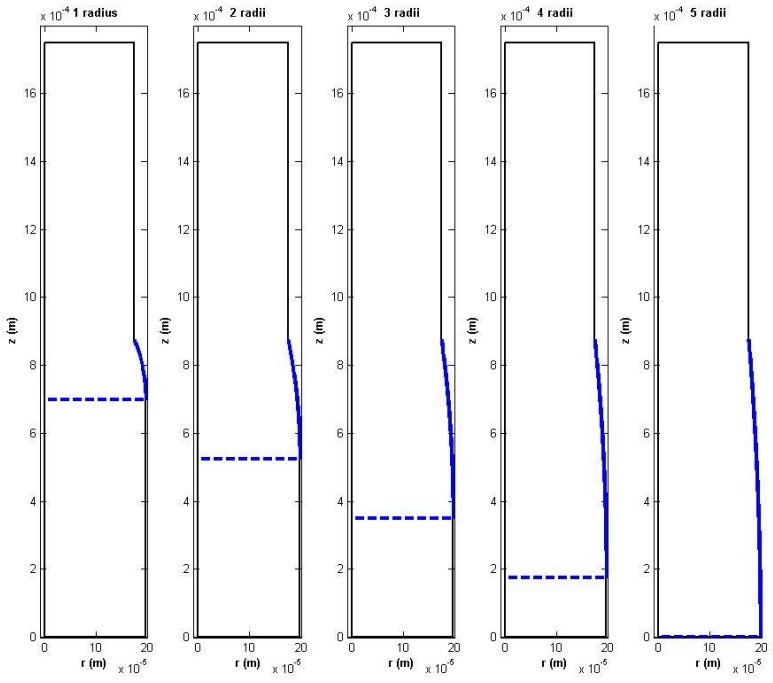

Figure 3.2. Five Expansion Lengths Plotted for the Quadratic Free Surface Representation

3.3 Minimization Process

The goal of the optimization is to minimize the stress along the free surface boundary. The minimization problem is stated as

$$\min_{\underline{\alpha}} f(\underline{\alpha}) = \int_S T_n\big(S(\underline{\alpha})\big) + T_t\big(S(\underline{\alpha})\big)dz = 0 \tag{3.7}$$

$$\text{subject to} \quad 1.2 \geq \alpha_1 \geq \alpha_2 \geq \alpha_3 \geq \ldots \geq \alpha_n \geq 1$$

T_n and T_t are derived from the stress boundary condition $\boldsymbol{T}\colon[\mathbf{n}\ \mathbf{n}] = 0$ where $\boldsymbol{T}$ is presented in equation (3.3) and $\mathbf{n}$ is given as

$$\mathbf{n} = \begin{bmatrix} n_r \\ n_\theta \\ n_z \end{bmatrix} \tag{3.8}$$

with the understanding that all θ components are equal to zero for the axisymmetric representation. The stress boundary condition $\boldsymbol{T}\colon[\mathbf{n}\ \mathbf{n}] = 0$ can be written as

$$\boldsymbol{T}\colon[\mathbf{n}\ \mathbf{n}] = \left(-p\begin{bmatrix} 1 & 0 & 0 \\ 0 & 1 & 0 \\ 0 & 0 & 1 \end{bmatrix} + \mu\begin{bmatrix} 2\dfrac{\partial v_r}{\partial r} & 0 & \dfrac{\partial v_r}{\partial z} + \dfrac{\partial v_z}{\partial r} \\ 0 & 2\dfrac{v_r}{r} & 0 \\ \dfrac{\partial v_z}{\partial r} + \dfrac{\partial v_r}{\partial z} & 0 & 2\dfrac{\partial v_z}{\partial z} \end{bmatrix} \right) \begin{bmatrix} n_r \\ 0 \\ n_z \end{bmatrix} \begin{bmatrix} n_r \\ 0 \\ n_z \end{bmatrix} = 0 \tag{3.9}$$

After expansion the stress boundary condition can be written as

$$\begin{aligned} \boldsymbol{T}\colon[\mathbf{n}\ \mathbf{n}] = {} & -pn_rn_r - pn_zn_z + 2\mu\frac{\partial v_r}{\partial r}n_rn_r + \mu\left(\frac{\partial v_r}{\partial z} + \frac{\partial v_z}{\partial r}\right)n_zn_r \\ & + 2\mu\frac{\partial v_z}{\partial z}n_zn_z + \mu\left(\frac{\partial v_z}{\partial r} + \frac{\partial v_r}{\partial z}\right)n_rn_z = 0 \end{aligned} \tag{3.10}$$

The stress boundary condition can be separated into two stress components T_n and T_t. where T_n is the normal stress on the free surface

$$T_n = -pn_r^2 + 2\mu\left(\frac{\partial v_r}{\partial r}\right)n_r^2 + \mu\left(\frac{\partial v_r}{\partial z} + \frac{\partial v_z}{\partial r}\right)n_zn_r \tag{3.11}$$

and T_t is the tangential stress on the free surface

$$T_t = -pn_z^2 + 2\mu\left(\frac{\partial v_z}{\partial z}\right)n_z^2 + \mu\left(\frac{\partial v_z}{\partial r} + \frac{\partial v_r}{\partial z}\right)n_r n_z \tag{3.12}$$

When the minimum value of both T_n and T_t is calculated the correct extrudate swell shape has been reached.

The minimization problem is solved for each of the five expansion length options for each of the different functions that have been defined. MATLAB's fmincon function is used for the minimization process. fmincon is defined by MATLAB as

$$[x, fval, \sim, output] = fmincon(fun, x_0, \sim, \sim, \sim, \sim, lb, ub, nonlcon, options) \tag{3.13}$$

where x is the vector of optimum values, $fval$ is the value of the objective function at the optimum point, and $output$ is a function that contains minimization variables for each iteration of the minimization. In equation (3.13), fun is the objective function being minimized, x_0 is the initial vector of expansion values, ~ represents an unused parameter in this minimization, lb is the lower bound for the x vector, ub is the upper bound of the x vector, $nonlcon$ contains the constraints for the minimization function, and $options$ is a function that contains variables which change the minimization calculation.

The objective function for this study is calculated for each iteration by inserting the curve defined by the x vector, which contains the α_n expansion values for the free surface into the geometry in COMSOL. The initial x vector, x_0, the lower boundary, lb, and the upper boundary, ub, for this study are defined as

$$x_0 = \begin{bmatrix} 1.05 + (0.2 * (n-1)) \\ \dots \\ 1.09 \\ 1.07 \\ 1.05 \end{bmatrix}, lb = \begin{bmatrix} 1 \\ 1 \\ 1 \\ \dots \\ 1 \end{bmatrix}, ub = \begin{bmatrix} 1.2 \\ 1.2 \\ 1.2 \\ \dots \\ 1.2 \end{bmatrix} \tag{3.14}$$

The boundary conditions and mesh are then added to the defined geometry. The FEM problem is then run in COMSOL. Once the FEM solution is obtained the normal

and tangential stress are calculated in post processing using a "Line Integration" which is built in to COMSOL. This process is done for each iteration of the minimization. The options used for the minimization in this study designate the objective function tolerance, TolFun, which is set to 10^{-5}, the x vector tolerance, TolX, which is set to 10^{-5}, and the Algorithm used, Algorithm, is set to SQP (Sequential Quadratic Programming). When the optimum has been found for the current function or expansion value, the next function or expansion calculation is begun. The minimization with the lowest objective function value is then designated as the optimum free surface and the true shape of the extrudate swell for the given function and expansion length.

3.4 Calculation of Extrudate Swell

The steps taken to calculate the extrudate swell free surface are described in this section. The extrudate swell free surface is computed for 1) a straight tube and 2) a FDM nozzle. The models used to compute extrudate swell for both of these geometries are described below, where boundary conditions, fluid properties, and mesh properties that define the problem are provided for both of the models.

3.4.1 Extrudate Swell Calculation: Straight Tube Model

The first problem considered in this research is the flow of an isothermal Newtonian fluid through a straight tube, where the fluid domain is defined as that within the tube itself and also immediately adjacent to the tube beyond its exit where extrudate swell occurs. The properties used in this simulation are fluid density $\rho = 1040$ kg/cm^3 and dynamic viscosity of $\mu = 350$ Pa·s. These values are chosen since they present reasonable average properties for an ABS plastic, which is a common FDM printing material used in industry, at 230^{o}C and under

a shear rate of 575 s^{-1}. It is understood that since ABS is a polymer it is Non-Newtonian with a viscosity that varies with strain rate. Assuming an isothermal Newtonian fluid simplifies the simulation process and is expected to be a good first step into the study of fiber orientation in deposition processes. Additional insight into these processes could be gained in the future by including non-isothermal, non-Newtonian models which more accurately represent polymer melt flow. Here we consider a Newtonian fluid only, so a single value of viscosity is chosen for ABS at a nominal shear rate for the processing of ABS in a typical FDM process. Use of a Newtonian fluid also makes it possible to compare results in this thesis to known data from Georgiou [13] and Ellwood [15].

For this study we use $v_{max} = 108.6 \frac{mm}{s}$ and $r_{max} = 0.175\ mm$. This inlet velocity allows for an average extrusion tube exit velocity of 66.5 $\frac{mm}{s}$,which is in the range of extrusion speeds for most desktop FDM printers. The mesh for the finite element model is created based on the geometry and boundary conditions of the problem. The mesh used for this problem is a mapped quad mesh which is well suited for fluid flow problems since the likelihood of numerical instabilities is reduced. The mapped quads also allow for elements of nearly equal size along the extrudate swell boundary, which results in more accurate stress calculation during the extrudate swell optimization solution process. The geometry and mesh defined can be seen in Figure 3.3.

Once the fluid domain has been defined and meshed, the finite element solution can be calculated. The mesh for the straight tube extrudate swell model has 199200 domain elements, 3256 boundary elements, 602037 degrees of freedom, and takes 41 seconds to compute the velocity and pressure solution. The objective function in equation (3.7) is evaluated by computing the normal and tangential stresses in equations (3.8) and

(3.9), respectively, from z = 0.875 *mm* to z = 0 *mm*. The velocity normal to the surface is also integrated along the free surface. The FEM solution is calculated for each optimization iteration during the minimization procedure. After the stress calculation, all the necessary data is stored for the given iteration, then the swell boundary geometry is removed from the finite element model so that the new geometry with the new swell values can be created. This is repeated until the optimization process reaches the minimum stress state along the free surface.

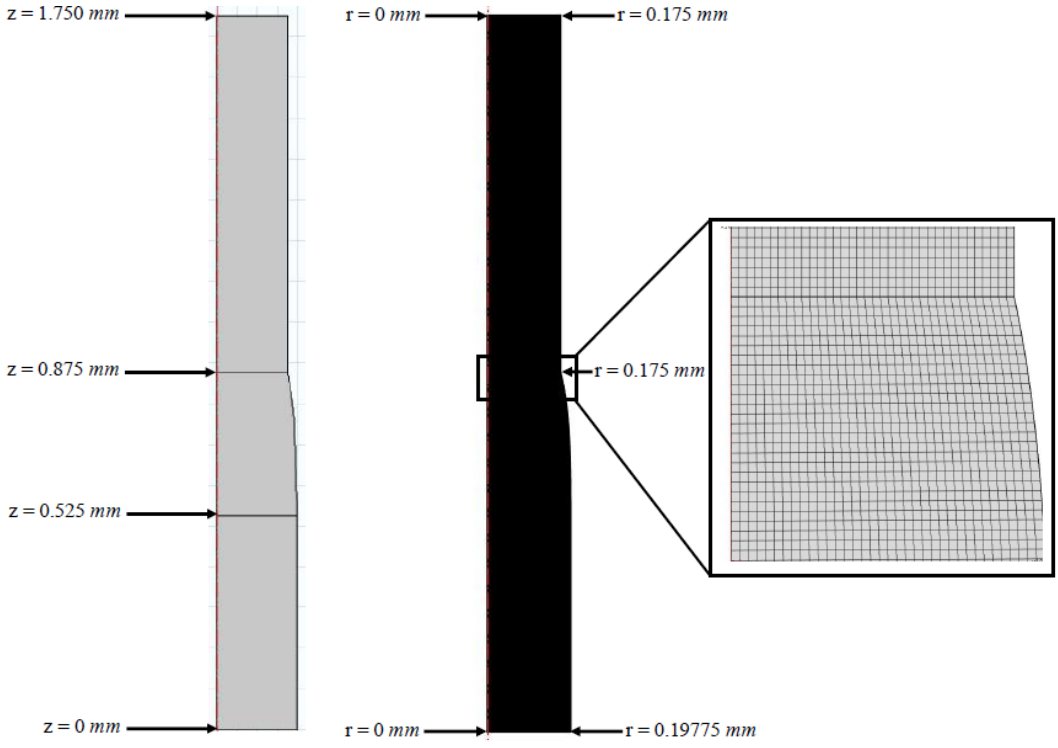

Figure 3.3. Geometry and Mapped Mesh for the Straight Tube Extrudate Swell Problem

3.4.2 Extrudate Swell Calculation: FDM Nozzle

The straight tube extrusion model above provides a means to validate the proposed modeling approach. However, understanding the effect of a typical FDM nozzle on extrudate swell and fiber orientation requires that the analysis above be extended to

include the appropriate geometry. The geometry, boundary conditions, and meshing for a typical FDM nozzle will be defined in the following section. The boundary conditions used in the full nozzle are similar to the straight tube problem. The FDM nozzle model simply adds a larger inlet and a convergence zone upstream from the nozzle exit.

The cross section showing the geometrical aspects of a common FDM extrusion nozzle are shown in Figure 3.4.

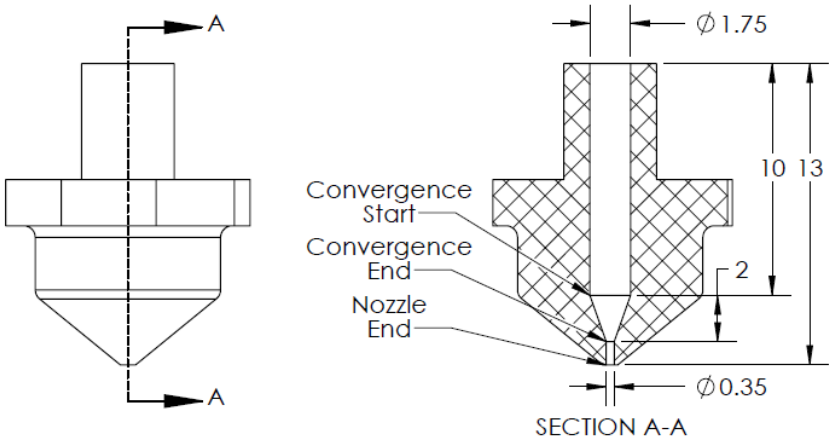

Figure 3.4. Common FDM Nozzle Geometry, Dimensions are Shown in Millimeters (mm)

A typical FDM nozzle geometry is modeled with a two-dimensional axisymmetric finite element model to represent the actual three-dimensional nozzle. The axisymmetric cross section of the fluid domain for the FDM nozzle considered in this study appears in Figure 3.4. A section extending from the nozzle exit with a length of 5 radii is included for the analysis of the extrudate swell free surface. The fluid domain can be seen in Figure 3.5 with dimensions and boundary conditions.

The inlet at z = 5.625 *mm* is defined as a parabolic profile for laminar flow within a tube as defined by equation (3.4). For this study we use $v_{max} = 4\frac{mm}{s}$ and $r_{max} =$

0.875 *mm*. This inlet velocity allows for an average nozzle exit velocity of 66.5 $\frac{mm}{s}$ which is typical for desktop FDM printers. The properties used in this simulation are fluid density ρ = 1040 kg/cm^3 and dynamic viscosity of μ = 350 Pa·s. The outlet at z = 0 *mm* is defined as pressure P = 0 Pa. The free surface is defined as a slip wall from z = 0 *mm* to 0.875 *mm*. The remaining outer portion of the wall is defined as a no slip wall, and the wall at r = 0 *mm* is defined as an axisymmetric wall.

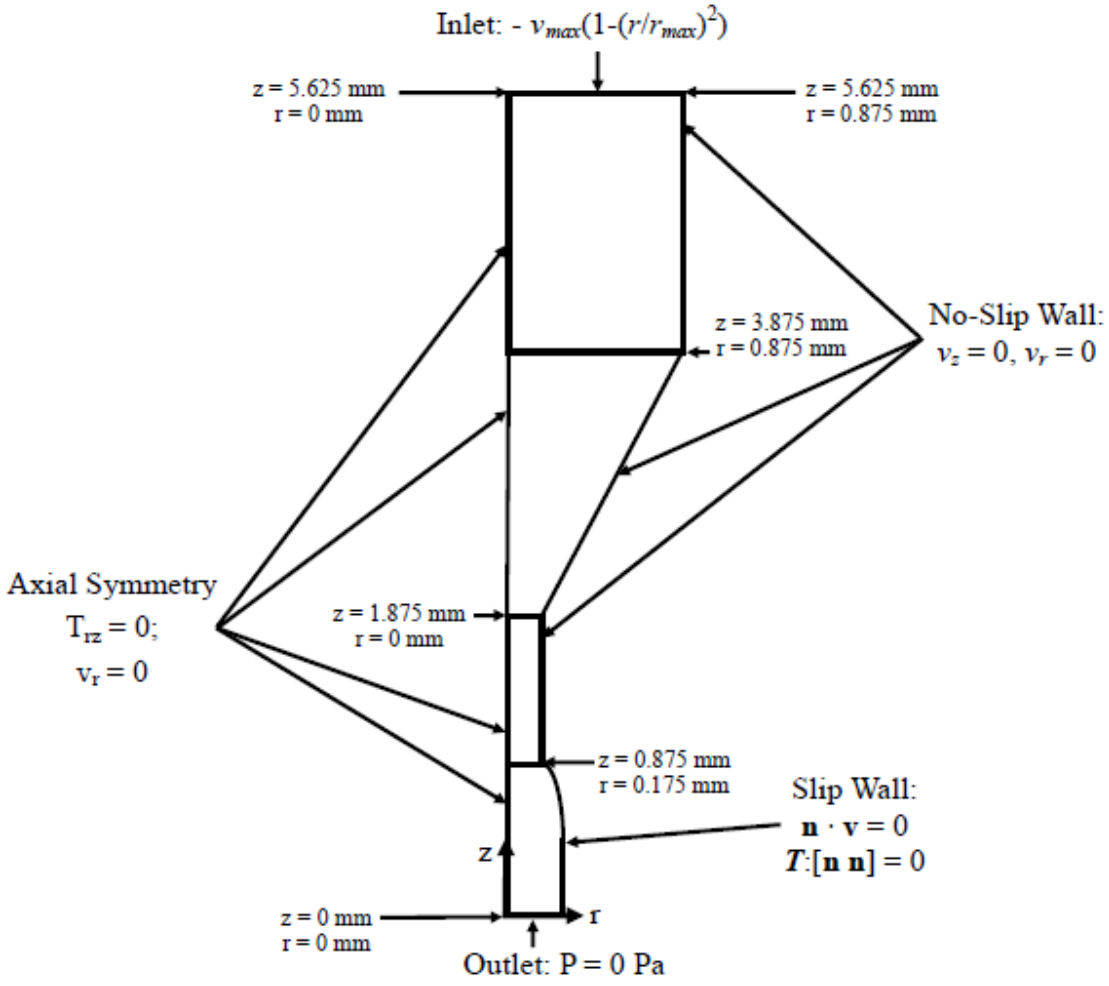

Figure 3.5. Boundary Conditions and Dimensions for the Full Nozzle Extrudate Swell Calculation

The mesh for this geometry was changed slightly from the Georgiou model. In order to decrease computational time, the domain defined by the inlet zone and convergence zone is modeled with triangular elements, and the straight portion of the nozzle and the extrudate swell portion of the fluid domain is modeled with quad elements, as before. The finite element mesh for a typical FDM nozzle model used in this study appears in Figure 3.6 below.

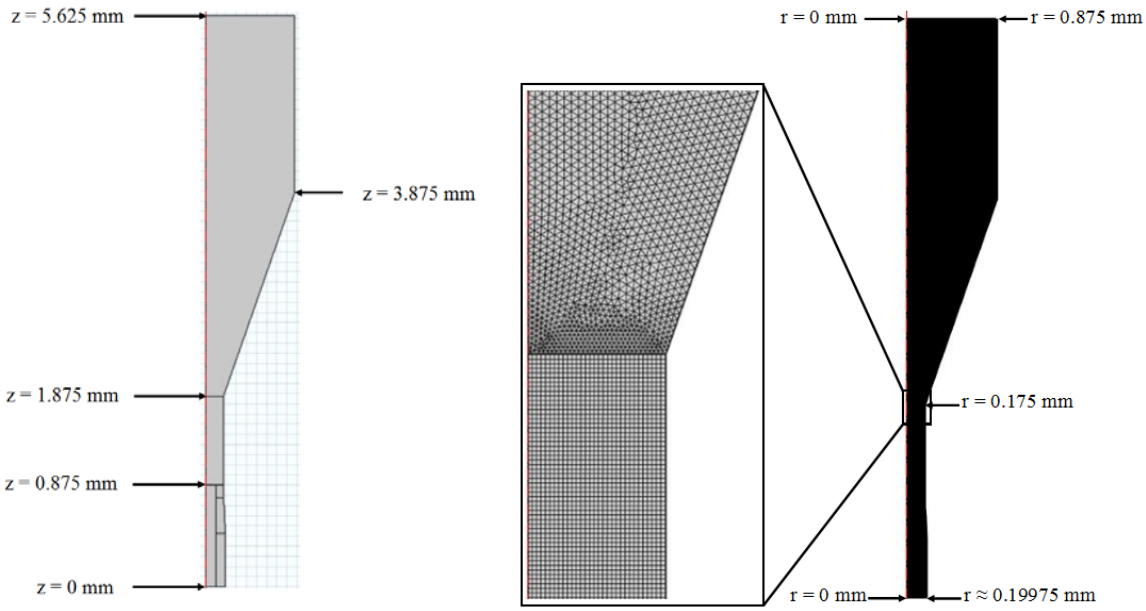

Figure 3.6. Geometry and Mesh for the Full Nozzle Extrudate Swell Calculation

It was found that for the full nozzle problem, a mapped quad mesh became inefficient with respect to calculation time and changes in mesh size between the inlet and outlet were difficult to accommodate. A COMSOL free quadrilateral mesh was considered, but the need for a very fine mesh size resulted in a finite element meshing issue which would affect the overall minimization method. The use of triangular elements in this model allow for a much faster solution time and the ability to mesh any domain. In

order to be confident in the use of triangular elements a study was performed in which it was found that a very fine triangular mesh would allow for the proper die swell calculation and also served to decrease the stress state along the free surface. The results of the mesh study are shown in Table 3.1. COMSOL uses a number system for mesh size which is used in the Table 3.1. Mesh sizes are defined as 1 – Extremely Fine, 2 – Extra Fine, 3 – Very Fine, and 4 – Fine.

Table 3.1. Mesh Study for FDM Nozzle Minimization Problem

Mesh	Number of Domain Elements	Number of Boundary Elements	Number of Degrees of Freedom	Optimum Free Surface Stress (N/m^2)	Calculation Time (s)	Mesh Time (s)	Calculation Time with 180 function calls (s)
Mapped Mesh 4	5568	559	51220	10.3	5	0.17	930
Mapped Mesh 3	8568	693	78485	9.52	7	0.2	1300
Mapped Mesh 2	38962	1475	353576	7.37	29	0.4	5300
Mapped Mesh 1	147450	2866	1332718	5.63	111	0.83	20200
Mapped 1 and Triangular 1	223425	2387	1055652	4.73	76	20.9	17500
Mapped 1 and Triangular 2	63746	1692	335359	4.73	24	3	4900
Mapped 1 and Triangular 3	21506	1298	144294	4.73	13	0.63	2450
Mapped 1 and Triangular 4	17542	1228	126281	4.73	11	0.53	2100

The normal and tangential stress as well as the normal velocity are integrated along the free surface from z = 0.875 *mm* to z = 0 *mm*. The FEM solution is calculated in COMSOL for each iteration of the minimization performed in MATLAB. After the stress

calculation all the necessary data is stored for the given iteration, then the swell boundary geometry is removed from the finite element model so that the new geometry with the new swell values can be built. This is repeated until the optimization process reaches the minimum stress state along the free surface.

3.5 Extrudate Swell Results

The results for the extrudate swell free surface minimization for both the straight tube model and the FDM nozzle is discussed in this section. Calculation of the extrudate swell was found to be sensitive to the meshing and boundary conditions. It was also found that the results were repeatable and had very little variation, which is a necessary property for a minimization to run effectively.

3.5.1 Straight Tube Model Results

The optimum free surface shape that defines the extrudate swell geometry is calculated using the minimization approach presented above. Figure 3.7 shows the optimization history and extrudate free surface shape for two surfaces that define the die swell shape. As has been stated previously, we use the function shape and magnitude that is presented in literature [29, 30, 32] as a benchmark.

Figure 3.7 (a) and (b) show that there is good agreement between the optimal fourth-order representation of the free surface and the Georgiou [29] curve defining extrudate swell. The fourth order polynomial contains four evenly spaced points, and at each point an expansion value $\alpha_i$is defined. The fourth order polynomial defined over two radii of expansion length with α_i defined at z = 0.525 *mm,* 0.642 *mm,* 0.758 *mm*, and 0.875 *mm* has expansion values

$$\alpha_1 = 1.1274;\ \alpha_2 = 1.1229;\ \alpha_3 = 1.10945;\ \alpha_4 = 1$$

and a final polymer bead radius of 0.1973 *mm,* and final stress state T_{tot} = 2.92$\frac{N}{m^2}$. In a different optimization, the fourth order polynomial defined over three radii of expansion length with α_i defined at z = 0.350 *mm,* 0.525 *mm,* 0.700 *mm*, and 0.875 *mm* has expansion values

$$\alpha_1 = 1.1289;\ \alpha_2 = 1.1275;\ \alpha_3 = 1.1139;\ \alpha_4 = 1$$

and a final polymer bead radius of 0.1976 *mm,* and final stress state T_{tot} = 3.082$\frac{N}{m^2}$. Both of the given equations have a lower final stress state than the curve given in the die swell literature which returns T_{tot} = 3.935$\frac{N}{m^2}$.

Figure 3.8 (a) and (b) shows similar values are obtained for a fifth order polynomial representation of the extrudate swell free surface. The fifth order polynomial contains five evenly spaced points, and at each point an expansion value is defined. The fifth order polynomial defined over two radii of expansion length with α_i defined at z = 0.525 *mm,* 0.613 *mm,* 0.700 *mm,* 0.788 *mm*, and 0.875 *mm* has expansion values

$$\alpha_1 = 1.1275;\ \alpha_2 = 1.1250;\ \alpha_3 = 1.1137;\ \alpha_4 = 1.0791;\ \alpha_5 = 1$$

and a final polymer bead radius of 0.1973 *mm,* and final stress state T_{tot} = 2.8$\frac{N}{m^2}$.

The fifth order polynomial defined over five radii of expansion length with α_i defined at z = 0 *mm,* 0.219 *mm,* 0.438 *mm,* 0.656 *mm*, and 0.875 *mm* has expansion values

$$\alpha_1 = 1.1294;\ \alpha_2 = 1.1294;\ \alpha_3 = 1.1279;\ \alpha_4 = 1.1222;\ \alpha_5 = 1$$

and a final polymer bead radius of 0.1976 *mm,* and final stress state T_{tot} = 3.38$\frac{N}{m^2}$. Both of the given equations have a lower final stress state than the curve given in the literature which returns T_{tot} = 3.935$\frac{N}{m^2}$.

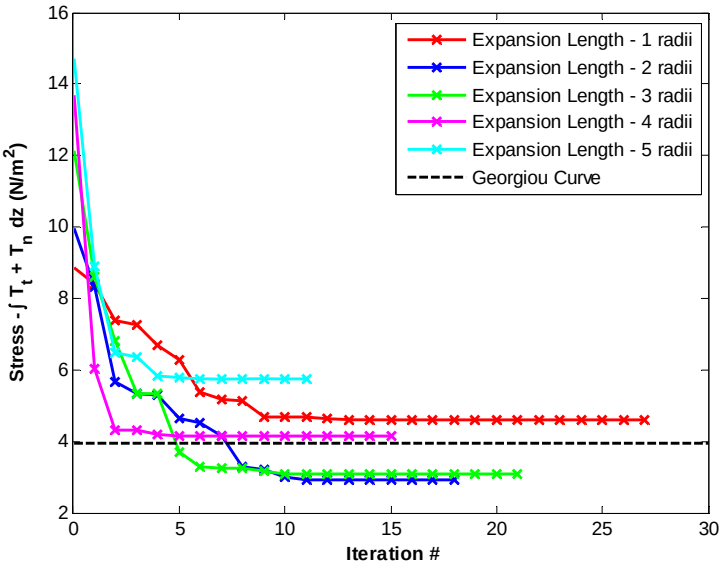

(a)

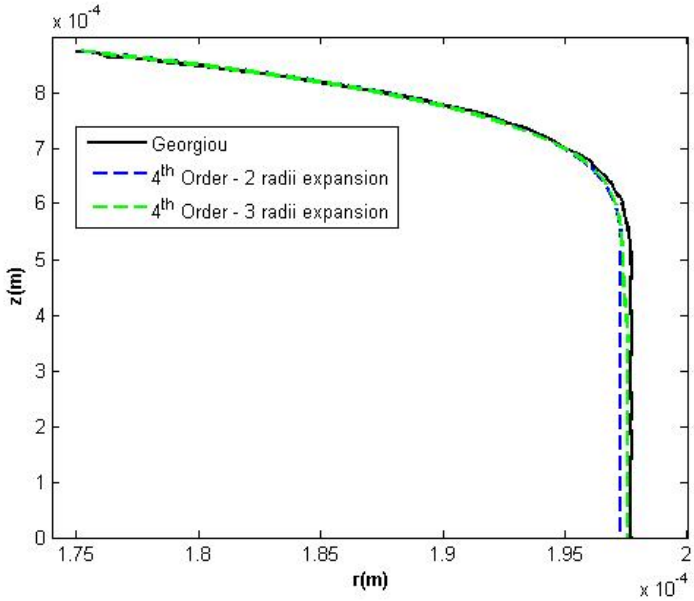

(b)

Figure 3.7. Optimum Curve Using a 4th Order Function (a) & (b).

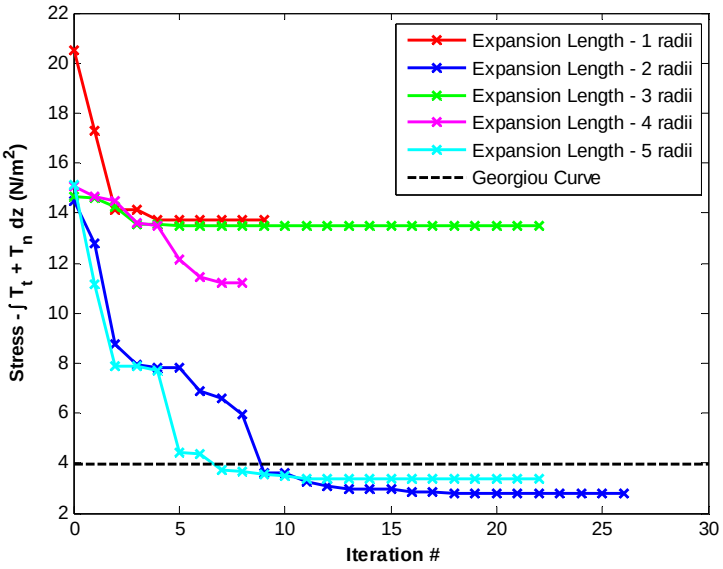

(a)

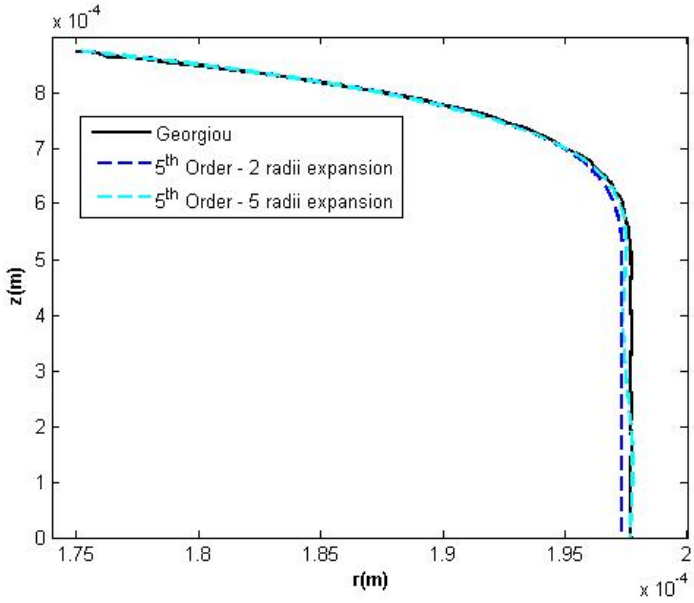

(b)

Figure 3.8. Optimum Curve using a 5th Order Function (a) & (b). in the Optimization Process

Depending on the method of calculation and tolerance placed on the minimization there can be slight differences in the final percentage of extrudate swell. The four curves shown above for the optimization process deviate only 0.26% from the optimum swell value of 13%, and it is common in literature to see values that vary for the extrudate

swell. From the study above, it is proved that the die swell shape can be accurately defined by using a minimization of the free surface stress. For the rest of the calculations a fourth order function defined over 2 radii of expansion will be used. It was seen that this function could repeatedly find the 13% swell value.

3.5.2 Full Nozzle Results

The full nozzle was treated in the same way the straight tube extrusion problem was treated. The minimization was again able to find approximately the 13% swell for the fourth order representation with 2 radii of defined expansion. The minimization results and shape of the extrudate swell function is shown below for the full nozzle problem. Figure 3.9 (a) shows that a minimum is found lower than that of the benchmark extrudate swell shape. The fourth order polynomial defined over two radii of expansion length with α_i defined at z = 0.525 *mm,* 0.642 *mm,* 0.758 *mm*, and 0.875 *mm* has expansion values

$$\alpha_1 = 1.1329;\ \alpha_2 = 1.1280;\ \alpha_3 = 1.10987;\ \alpha_4 = 1$$

and a final polymer bead radius of 0.1983 *mm* which is shown in Figure 3.9 (b), and final stress state $T_{tot} = 4.74\frac{N}{m^2}$. The final stress state for the curve given in the literature returns $T_{tot} = 5.46\frac{N}{m^2}$. The reason for the higher stress state for the full nozzle has to do with the mesh size available for the larger geometry. The effect of mesh size will be discussed in the following section.

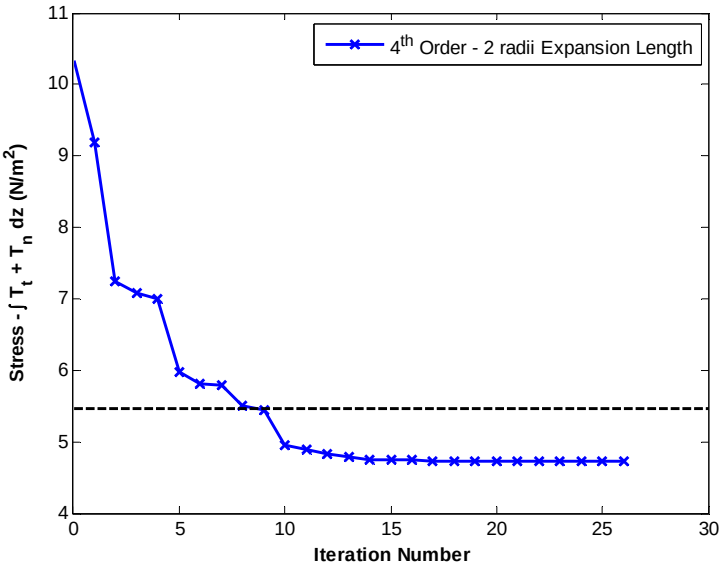

(a)

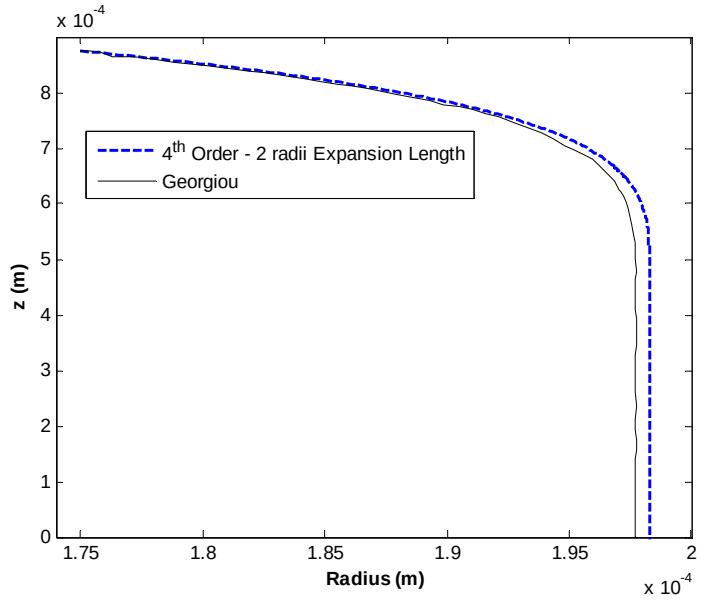

(b)

Figure 3.9. Minimization Path (a) and Shape of Minimum Extrudate Swell Curve (b)

3.5.3 Effect of The Stick-Slip Singularity

A very important effect that is noticed in Figure 3.7-9, is that the minimum value that defines the optimum free surface shape is not equal to zero. The reason for this non-

zero minimum, is a singularity that is inherent to the extrudate swell problem. The stick-slip singularity occurs at the point where the boundary condition transitions from a no slip boundary ($v_r = 0$ and $v_z = 0$) to a slip boundary condition ($\mathbf{n}\cdot\mathbf{v} = 0$), and is responsible for the non-zero minimum stress value observed in Figure 3.7-9. To show the shape and intensity of the singularity the normal, tangential, and combined stresses are plotted in Figure 3.10.

In Figure 3.10, we can see a steep spike in the two stress components from the singularity. This spike, while occuring over a very small distance, is large enough to add a substantial amount of stress to the integration over the free surface. The effect of the singularity is essentially gone after just 0.02 *mm* in the current model, which is only 2.3% of the entire free surface. In order to show the effect of the singularity and how it effects the integration, several integrals were taken at 0.01 *mm* intervals from 0.875 *mm* to 0.775 *mm*. It can be seen in Figure 3.11 how quickly the stress summation decreases outside of the singularity. The effect of the singularity can be reduced but not completely mitigated by increasing the number of elements and reducing the size of the elements around the stick-slip point. The effect of the singularity can be reduced further by the use of singular finite elements or upwinding techniques discussed by Georgiou [18] and Finlayson [19]. These methods allow for better convergence with fewer elements, but are difficult to apply when using a stand alone finite element software such as COMSOL Multiphysics. Even with the effect of the singularity, we are still able to minimize to the correct free surface shape. The only major concern is that the minimization is not able to drive the stress on the free surface to zero, but with the understanding that this is due to an inherent singularity in the finite element problem, this small amount of error is acceptable.

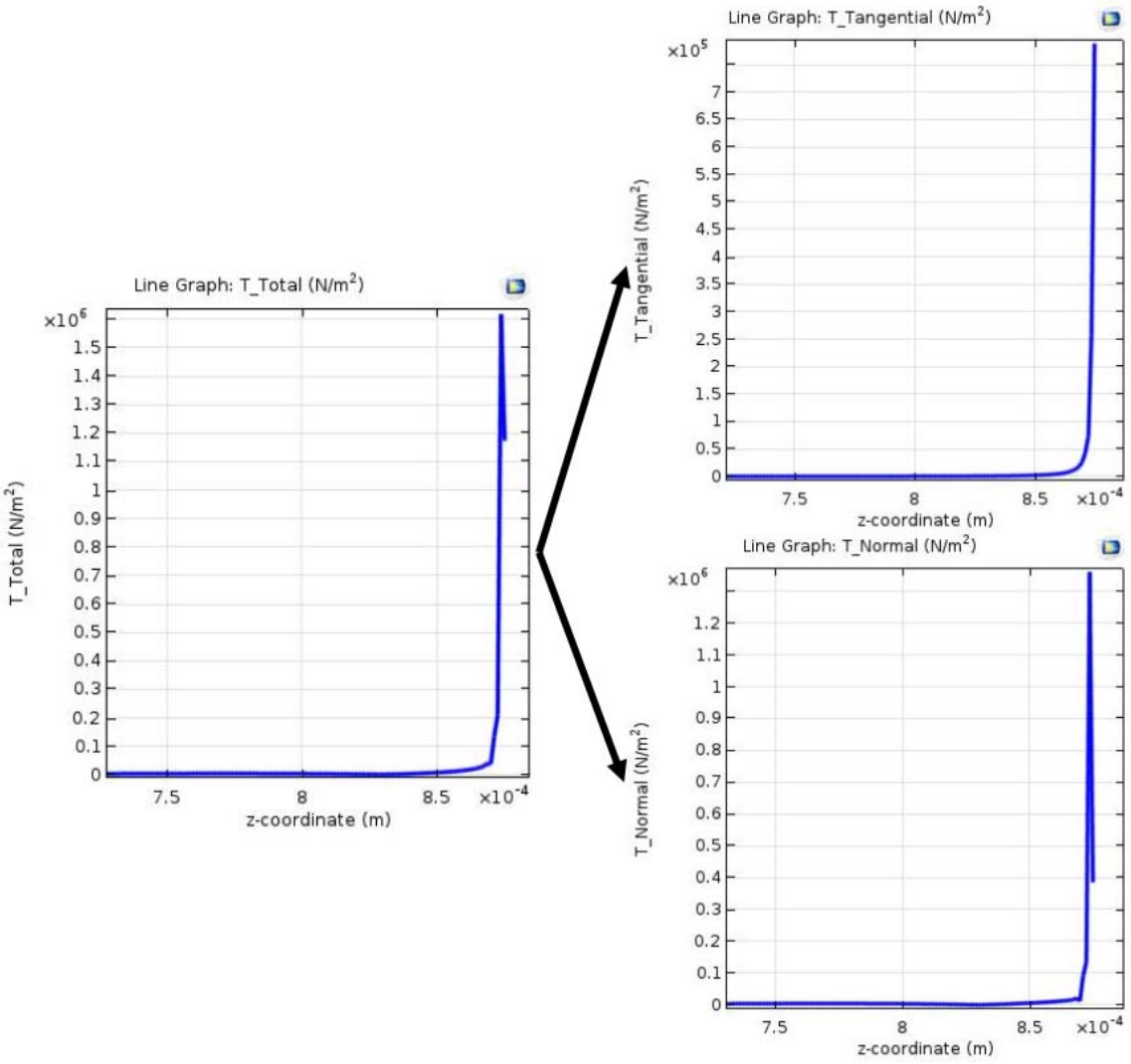

Figure 3.10. Plots of Stick-Slip Singularity Effects on the Tangential and Normal Stresses.

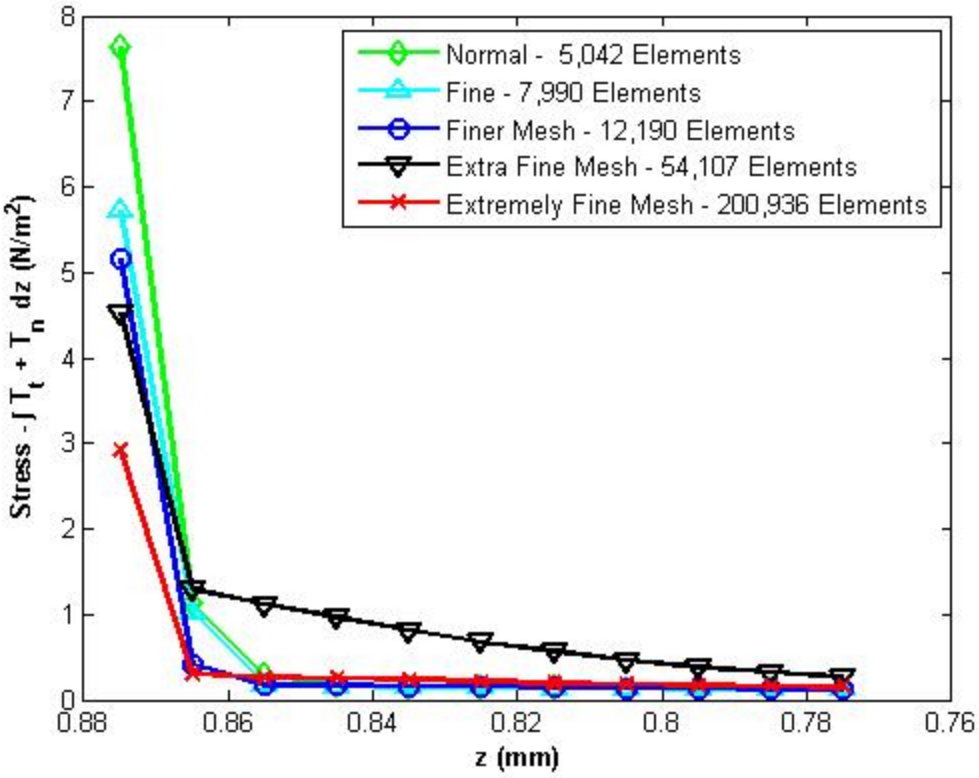

Figure 3.11. Integration Values along Free Surface for Different Mesh Sizes

CHAPTER FOUR

Fiber Orientation in FDM Nozzle Flow

The nozzle geometry and the extrudate swell free surface calculation was presented in the previous chapter to define the fluid domain representing the FDM nozzle flow. The fiber orientation throughout the entire fluid domain can be calculated from the velocity gradients in the flow field, which is important for determining the orientation state of the discrete fibers suspended in the polymer melt. The orientation state of the fibers after the nozzle exit is of interest in the current study. The fiber orientation state beyond the nozzle exit will determine the fiber orientation in the extruded bead and therefore in the final printed part. The fiber orientation state in the final printed part will define the strength, toughness, and other mechanical properties of that part. In this chapter the method for calculating the fiber orientation is presented, as well as the fiber orientation results seen for the straight tube extrudate swell and FDM nozzle problems.

4.1 Calculation of the Fiber Orientation

The fiber orientation calculation method used in this thesis employs the Advani-Tucker [10] orientation tensor approach with the Folgar-Tucker [7] isotropic rotary diffusion model for fiber-fiber interactions. The fiber orientation equation assuming isotropic rotary diffusion is given as

$$\frac{D\boldsymbol{A}}{Dt} = -\frac{1}{2}(\boldsymbol{\Omega}\cdot\boldsymbol{A} - \boldsymbol{A}\cdot\boldsymbol{\Omega}) + \frac{1}{2}\lambda(\boldsymbol{\Gamma}\cdot\boldsymbol{A} + \boldsymbol{A}\cdot\boldsymbol{\Gamma} - 2\mathbb{A}\colon\boldsymbol{\Gamma}) + 2C_I G(\boldsymbol{I} - 3\boldsymbol{A}) \qquad (4.1)$$

where the second and fourth order orientation tensors are defined respectively as

$$A_{ij} = \oint p_i p_j \psi(\boldsymbol{p})\, d\boldsymbol{p} \tag{4.2}$$

and

$$\mathrm{A}_{ijkl} = \oint p_i p_j p_k p_l \psi(\boldsymbol{p})\, d\boldsymbol{p} \tag{4.3}$$

In equation (4.1), C_I is the empirically obtained interaction coefficient defined by Folgar and Tucker [7], $\boldsymbol{I}$ is the identity tensor, $\boldsymbol{\Omega}$ is the vorticity tensor which is defined as,

$$\boldsymbol{\Omega} = [(\nabla \mathbf{v}) - (\nabla \mathbf{v})^{\mathrm{T}}] \tag{4.4}$$

$\boldsymbol{\Gamma}$ is the rate of deformation tensor given as,

$$\boldsymbol{\Gamma} = [(\nabla \mathbf{v}) + (\nabla \mathbf{v})^{\mathrm{T}}] \tag{4.5}$$

G is the magnitude of the strain rate tensor defined as,

$$G = (\boldsymbol{\Gamma} : \boldsymbol{\Gamma})^{\frac{1}{2}} \tag{4.6}$$

λ is the coeffiecient related to fiber geometry,

$$\lambda = \frac{r_e^2 - 1}{r_e^2 + 1} \tag{4.7}$$

where r_e is the equivalent fiber aspect ratio. In cylindrical coordinates, the velocity gradient $\nabla \mathbf{v}$ is defined as

$$\nabla \mathbf{v} = \begin{bmatrix} \frac{\partial v_r}{\partial r} & \frac{1}{r}\frac{\partial v_r}{\partial \theta} - \frac{v_\theta}{r} & \frac{\partial v_r}{\partial z} \\ \frac{\partial v_\theta}{\partial r} & \frac{1}{r}\frac{\partial v_\theta}{\partial \theta} + \frac{v_r}{r} & \frac{\partial v_\theta}{\partial z} \\ \frac{\partial v_z}{\partial r} & \frac{1}{r}\frac{\partial v_z}{\partial \theta} & \frac{\partial v_z}{\partial z} \end{bmatrix} \tag{4.8}$$

For axisymmetric problems having the z-axis as the axis of symmetry, v_θ and all derivatives with respect to Θ vanish yielding the following simplified two-dimensional axisymmetric velocity gradient

$$\nabla \mathbf{v} = \begin{bmatrix} \frac{\partial v_r}{\partial r} & 0 & \frac{\partial v_r}{\partial z} \\ 0 & \frac{v_r}{r} & 0 \\ \frac{\partial v_z}{\partial r} & 0 & \frac{\partial v_z}{\partial z} \end{bmatrix} \tag{4.9}$$

Note that the calculation of $\boldsymbol{A}$ in Equation (4.1) requires that the fourth order orientation tensor A_{ijkl} be known. Unfortunately, this requires the solution of an additional ordinary differential equation in time which includes the sixth order orientation tensor. To avoid this additional calculation, it is common to solve equation (4.1) using an approximation to, or closure of, A_{ijkl} calculated from A_{ij}. The closure method chosen in this study is the Fast Exact Closure from Montgomery-Smith, et al. [17]. The major benefit of this closure is that it does not need to calculate or approximate the fourth order moment tensor $\mathbb{A}$. The implementation of the fast exact closure causes the fiber orientation equation defined in equation (4.1) to be recast as [17]

$$\frac{D\boldsymbol{A}}{Dt} = -\frac{\mathbf{1}}{\mathbf{2}}\mathbb{C}\colon [\boldsymbol{B}\cdot(\boldsymbol{\Omega}+\lambda\boldsymbol{\Gamma}) + (-\boldsymbol{\Omega}+\lambda\boldsymbol{\Gamma})\cdot\boldsymbol{B}] + D_r(2\boldsymbol{I}-6\boldsymbol{A}) \tag{4.10}$$

$$\frac{D\boldsymbol{B}}{Dt} = -\frac{1}{2}(\boldsymbol{B}\cdot(\boldsymbol{\Omega}+\lambda\boldsymbol{\Gamma}) + (-\boldsymbol{\Omega}+\lambda\boldsymbol{\Gamma})\cdot\boldsymbol{B}) + D_r\mathbb{D}\colon(2\boldsymbol{I}-6\boldsymbol{A}) \tag{4.11}$$

where the tensor $\boldsymbol{B}$ is a parameter of orientation defined similar to that of the orientation tensor $\boldsymbol{A}$, and $\mathbb{C}$ and $\mathbb{D}$ are fourth-order conversion tensors. $\mathbb{C}$ is a symmetric tensor defined as

$$\mathbb{C} = \begin{bmatrix} \mathbb{C}_{1111} & \mathbb{C}_{1122} & \mathbb{C}_{1133} & 2\mathbb{C}_{1112} & 2\mathbb{C}_{1113} & 2\mathbb{C}_{1111} \\ \mathbb{C}_{2211} & \mathbb{C}_{2222} & \mathbb{C}_{2233} & 2\mathbb{C}_{2212} & 2\mathbb{C}_{2213} & 2\mathbb{C}_{2223} \\ \mathbb{C}_{3311} & \mathbb{C}_{3322} & \mathbb{C}_{3333} & 2\mathbb{C}_{3312} & 2\mathbb{C}_{3313} & 2\mathbb{C}_{3323} \\ 2\mathbb{C}_{1211} & 2\mathbb{C}_{1222} & 2\mathbb{C}_{1233} & 4\mathbb{C}_{1212} & 4\mathbb{C}_{1213} & 4\mathbb{C}_{1223} \\ 2\mathbb{C}_{1311} & 2\mathbb{C}_{1322} & 2\mathbb{C}_{1333} & 4\mathbb{C}_{1312} & 4\mathbb{C}_{1313} & 4\mathbb{C}_{1323} \\ 2\mathbb{C}_{2311} & 2\mathbb{C}_{2322} & 2\mathbb{C}_{2333} & 4\mathbb{C}_{2312} & 4\mathbb{C}_{2313} & 4\mathbb{C}_{2323} \end{bmatrix} \tag{4.12}$$

where the components of $\mathbb{C}$ are calculated in the principal frame of $\boldsymbol{A}$ and $\boldsymbol{B}$ as

$$\bar{\mathbb{C}}_{1122} = \frac{a_1 - a_2}{2(b_2 - b_1)} \qquad \bar{\mathbb{C}}_{1111} = \frac{1}{2} b_1^{-1} - \bar{\mathbb{C}}_{1122} - \bar{\mathbb{C}}_{1133}$$

$$\bar{\mathbb{C}}_{1133} = \frac{a_1 - a_3}{2(b_3 - b_1)} \qquad \bar{\mathbb{C}}_{2222} = \frac{1}{2} b_2^{-1} - \bar{\mathbb{C}}_{1122} - \bar{\mathbb{C}}_{2233} \tag{4.13}$$

$$\bar{\mathbb{C}}_{2233} = \frac{a_2 - a_3}{2(b_3 - b_2)} \qquad \bar{\mathbb{C}}_{3333} = \frac{1}{2} b_3^{-1} - \bar{\mathbb{C}}_{1133} - \bar{\mathbb{C}}_{2233}$$

$$\bar{\mathbb{C}}_{ijkk} = 0 \; if \; i \neq j \neq k$$

The conversion tensors are calculated in the orthonormal basis of $\boldsymbol{B}$; therefore, b_1, b_2, and b_3 are the values of the diagonal matrix $\boldsymbol{B}$ and a_1, a_2, and a_3 are the values of the diagonal matrix $\boldsymbol{A}$.

The conversion tensor $\mathbb{D}$ is defined as

$$\mathbb{D} = \mathbb{C}^{-1} = \begin{bmatrix} \mathbb{D}_{1111} & \mathbb{D}_{1122} & \mathbb{D}_{1133} & 2\mathbb{D}_{1112} & 2\mathbb{D}_{1113} & 2\mathbb{D}_{1111} \\ \mathbb{D}_{2211} & \mathbb{D}_{2222} & \mathbb{D}_{2233} & 2\mathbb{D}_{2212} & 2\mathbb{D}_{2213} & 2\mathbb{D}_{2223} \\ \mathbb{D}_{3311} & \mathbb{D}_{3322} & \mathbb{D}_{3333} & 2\mathbb{D}_{3312} & 2\mathbb{D}_{3313} & 2\mathbb{D}_{3323} \\ 2\mathbb{D}_{1211} & 2\mathbb{D}_{1222} & 2\mathbb{D}_{1233} & 4\mathbb{D}_{1212} & 4\mathbb{D}_{1213} & 4\mathbb{D}_{1223} \\ 2\mathbb{D}_{1311} & 2\mathbb{D}_{1322} & 2\mathbb{D}_{1333} & 4\mathbb{D}_{1312} & 4\mathbb{D}_{1313} & 4\mathbb{D}_{1323} \\ 2\mathbb{D}_{2311} & 2\mathbb{D}_{2322} & 2\mathbb{D}_{2333} & 4\mathbb{D}_{2312} & 4\mathbb{D}_{2313} & 4\mathbb{D}_{2323} \end{bmatrix} \tag{4.14}$$

There are two instances that can cause issues in equation (4.13) which are discussed in depth by Montgomery-Smith et al. [17]. If two or all three of the eigenvalues b_1, b_2, and b_3 are the same, equation (4.13) can become $\frac{0}{0}$. These problems are avoided by alternate calculations of the $\bar{\mathbb{C}}$ terms listed above.

Using the structure given here the change in fiber orientation throughout any given fluid domain can be calculated. In the next section the specific method used to implement the fiber orientation calculation will be discussed in depth.

4.2 Implementation of the Fiber Orientation Calculation

The fiber orientation calculation relies on the velocity gradients in the fluid domain. To calculate the velocity gradients for the fluid domain the points from the stress

minimization described in Chapter Three are used to calculate the optimum extrudate swell curve. The optimum extrudate swell curve then defines the fluid flow boundary in the finite element model using the LiveLink program. The geometry is then meshed and the finite element problem is calculated. Streamlines within the fluid domain are computed with COMSOL (COMSOL, Stockholm, Sweden) from the velocities and velocity gradients. Ten evenly spaced streamlines are placed along the outlet boundary. For clarity the streamlines do not remain evenly spaced throughout the domain which can be seen in Figure 4.8. Streamlines are calculated in COMSOL using a second order Runge-Kutta integration method along the direction of the vector. Along the ten defined streamlines the velocities and velocity gradients $\left(u, w, \frac{du}{dr}, \frac{du}{dz}, \frac{u}{r}, \frac{dw}{dr}, \frac{dw}{dz}\right)$ are calculated throughout the fluid domain. Here we define u as the velocity in the r direction, w as the velocity in the z direction, $\frac{du}{dr}$ as the change of the velocity in the r direction with respect to the r direction, $\frac{du}{dz}$ as the change of the velocity in the r direction with respect to the z direction, $\frac{u}{r}$ as the circumferential expansion of the fluid flow, $\frac{dw}{dr}$ as the change of the velocity in the z direction with respect to the r direction, and $\frac{dw}{dz}$ as the change of the velocity in the z direction with respect to the z direction. As an example the velocities and velocity gradients from streamline 1 in the straight tube extrudate swell problem are shown in Figure 4.1.

In Figure 4.1 the velocities and velocity gradients are shown with respect to time, but when the values calculated in the FEM problem are exported from COMSOL they are defined spatially. The spatial change from point to point needs to be converted to a time

step between the two points to solve the fiber orientation equation defined by equation (4.1) the spatial values must be converted to temporal values.

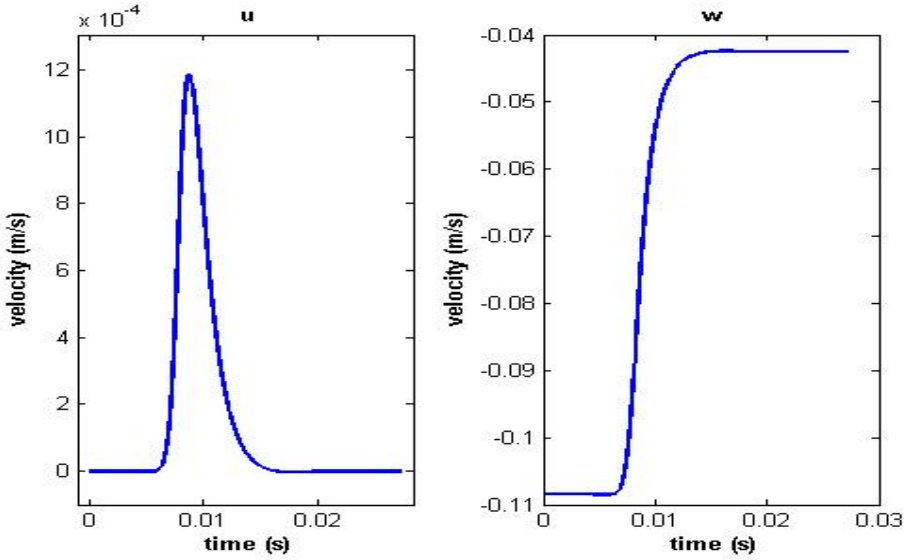

(a)

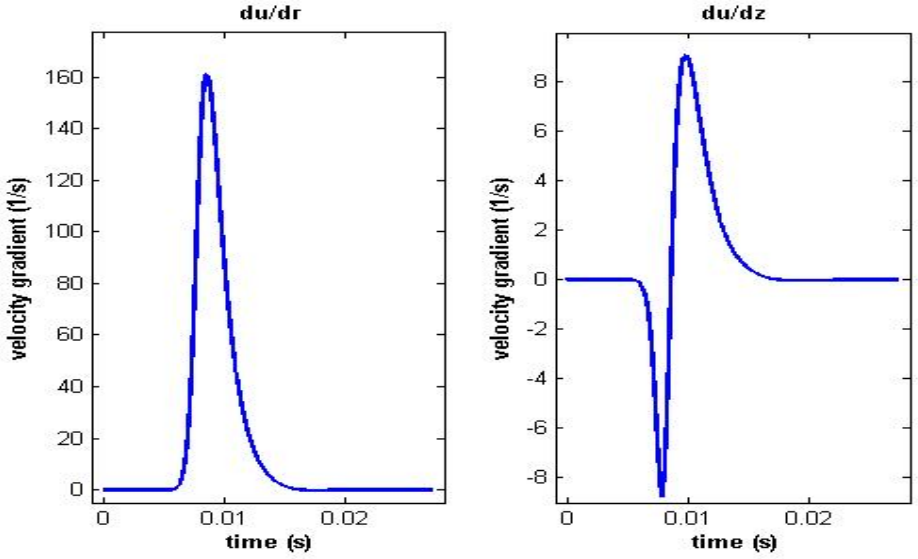

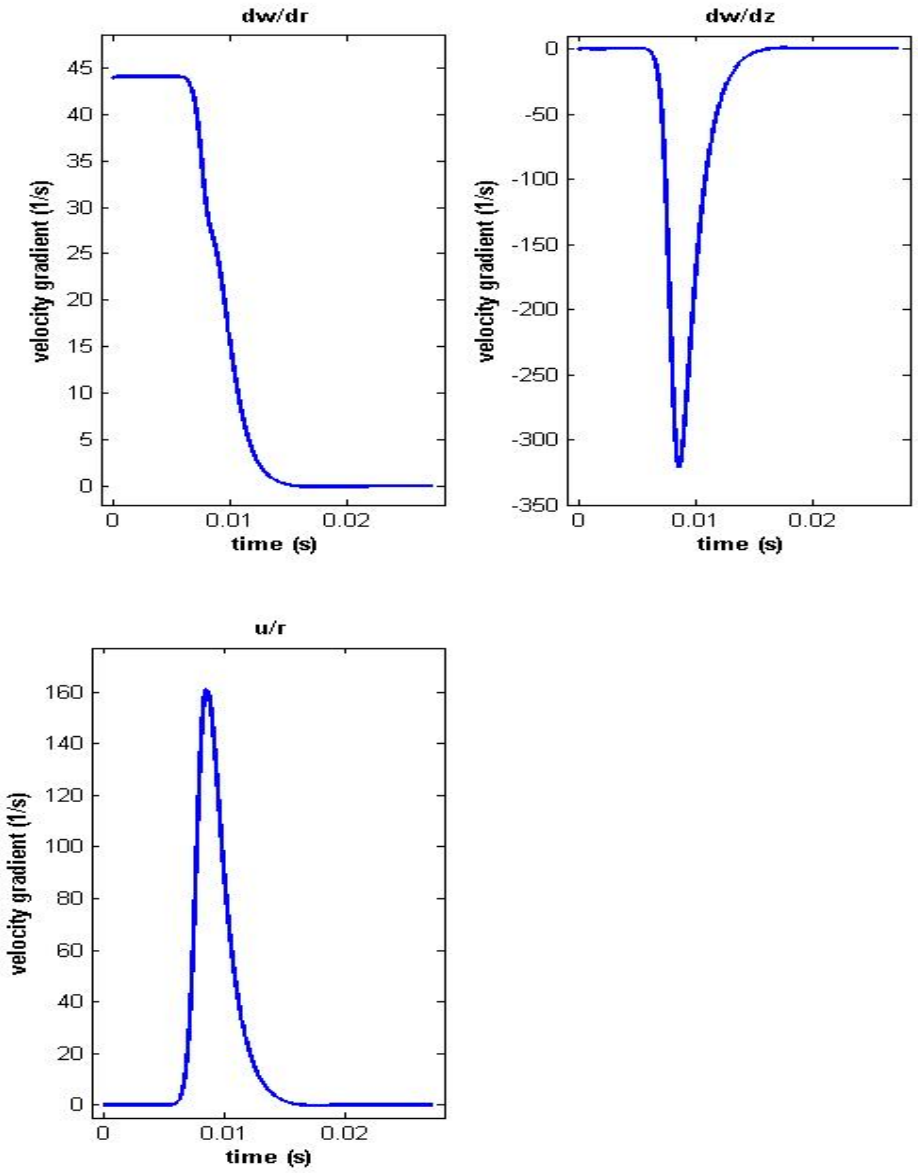

(b)

Figure 4.1. Velocities (a) and Velocity Gradients (b) Along Streamline 1 for the Straight Tube Extrudate Swell Problem

The evaluation of the time at the i+1 iteration is written as

$$t_{i+1} = \frac{d_i}{\|v\|_{\text{avg}}} + t_i \tag{4.15}$$

where d_i is the distance between two adjacent points in the streamline computed as

$$d_i = \sqrt{(r_{i+1} - r_i)^2 + (z_{i+1} - z_i)^2} \tag{4.16}$$

and $\|v\|_{avg}$ is the average of the magnitude of the velocity between the same two points given as

$$\|v\|_{avg} = \frac{\|v_{i+1}\| + \|v_i\|}{2} \tag{4.17}$$

This calculation gives the time it takes to get from the current point t_i to the next point t_{i+1} in seconds along the streamline. The velocities and velocity gradients can now be defined at specific time steps through the fluid domain.

In the fiber orientation equation there are two constants that must be defined. C_I is a constant that is defined empirically by Folgar-Tucker [7] and represents the amount fiber interaction. In equation (4.1) λ is a coefficient that is defined by the fiber geometry. To begin the fiber orientation calculation an initial $\boldsymbol{A}$ and $\boldsymbol{B}$ tensor must be selected which defines the initial orientation of the fibers entering the fluid domain of interest. The change in fiber orientation state can then be calculated throughout the given fluid domain.

To calculate the change in fiber orientation with respect to time using the initial conditions and constants a Runge-Kutta method is employed for the solution of the ordinary differential equation. The Runge-Kutta method used in this study is an adaptive step Runge-Kutta which uses a combination of the fourth and fifth order Runge-Kutta methods which can be written as

$$\boldsymbol{A}_{n+1}^{4RK} = \boldsymbol{A}_n^{4RK} + h\left(\frac{37}{378}k_1 + \frac{250}{621}k_3 + \frac{125}{594}k_4 + \frac{512}{1771}k_6\right) \tag{4.18}$$

$$\boldsymbol{A}_{n+1}^{5RK} = \boldsymbol{A}_n^{5RK} + h\left(\frac{2825}{27648}k_1 + \frac{18575}{48384}k_3 + \frac{13525}{55296}k_4 + \frac{277}{14336}k_5 + \frac{1}{4}k_6\right) \tag{4.19}$$

where k_1, k_2, k_3, k_4, k_5, and k_6 are defined as

$$k_1 = f(t_n, \mathbf{A}_n)$$

$$k_2 = f(t_n + \frac{h}{5}, \mathbf{A}_n + \frac{h}{5}k_1)$$

$$k_3 = f(t_n + \frac{3h}{10}, \mathbf{A}_n + \frac{3h}{40}k_1 + \frac{9h}{40}k_2)$$

$$k_4 = f(t_n + \frac{3h}{5}, \mathbf{A}_n + \frac{3h}{10}k_1 - \frac{9h}{10}k_2 + \frac{6h}{5}\mathrm{k}_3) \tag{4.20}$$

$$k_5 = f(t_n + h, \mathbf{A}_n - \frac{11h}{54}k_1 + \frac{5h}{2}k_2 - \frac{70h}{27}\mathrm{k}_3 + \frac{35h}{27}k_4)$$

$$k_6 = f(t_n + \frac{7h}{8}, \mathbf{A}_n + \frac{1631h}{55296}k_1 + \frac{175h}{512}k_2 + \frac{575h}{13824}\mathrm{k}_3 + \frac{44275h}{110592}k_4 + \frac{253h}{4096}k_5)$$

In equation (4.18) and (4.19) $\boldsymbol{A}$ is a vector containing 5 components of the orientation tensor $\boldsymbol{A}$, and h is the time step. For the adaptive Runge-Kutta the time step h is checked at each step. Error at each time step is calculated as

$$Err_P = \left\| \mathbf{A}^{5\mathrm{RK}} - \mathbf{A}^{4\mathrm{RK}} \right\| \tag{4.21}$$

where $\boldsymbol{A}^{5RK}$ is the solution to the fifth order Runge-Kutta, and $\boldsymbol{A}^{4RK}$ is the solution for a fourth order Runge-Kutta. If the error is equal to zero the original time step is used, if the error, Err_P, is greater than the minimum error, Err_{min}, the new time step is given as

$$h_{new} = h\left(\frac{Err_{min}}{Err_P}\right)^{\frac{1}{4}} \tag{4.22}$$

and if the error, Err_P, is less than the minimum error, Err_{min}, the new time step is given as

$$h_{new} = h\left(\frac{Err_{min}}{Err_P}\right)^{\frac{1}{5}} \tag{4.23}$$

A maximum step size is defined for the Runge-Kutta method so the method does not increase to too large of a step which can cause oscillations. If h_{new} is greater than the max time step, h_{max}, the new time step is set to the defined maximum time step.

Oscillatory results can occur when large velocity gradients exist along a streamline. Note that the k values in equation (4.19) calculate the slope at different points in the time interval. Oscillations can occur if the values of k differ significantly in a time step. The time step size is therefore found using a brute force method of increasing and decreasing the maximum step size. The maximum step size is set as a large value and slowly reduced until smooth accurate results are reached.

Since orientation tensors are symmetric and the trace of $\boldsymbol{A}$ is unity, only five components are computed, i.e. $A_{21} = A_{12}$, $A_{31} = A_{13}$, and $A_{23} = A_{32}$; therefore, only A_{11}, A_{22}, A_{12}, A_{13}, and A_{23} are calculated for the following models. A sixth orientation tensor component, A_{33}, is shown in the results to aid in understanding of the orientation state and is given as

$$A_{33} = 1 - A_{11} - A_{22} \tag{4.24}$$

In the following studies the orientation tensor $\boldsymbol{A}$ and $\boldsymbol{B}$ are defined as

$$\boldsymbol{A} = \begin{bmatrix} A_{rr} & A_{r\theta} & A_{rz} \\ A_{\theta r} & A_{\theta\theta} & A_{\theta z} \\ A_{zr} & A_{\theta z} & A_{zz} \end{bmatrix} \text{ and } \boldsymbol{B} = \begin{bmatrix} B_{rr} & B_{r\theta} & B_{rz} \\ B_{\theta r} & B_{\theta\theta} & B_{\theta z} \\ B_{zr} & B_{\theta z} & B_{zz} \end{bmatrix} \tag{4.25}$$

4.2 Pure Shear Steady State Fiber Orientation Calculation

The pure shear steady state fiber orientation was calculated to provide a more accurate inlet condition for the fiber orientation problems studied in this thesis. Using the pure shear steady state value of A_{ij} as the inlet condition allows for a shortened inlet geometry in the fiber orientation calculation since a transient solution to pure shear steady state can be avoided. To find the pure shear steady state fiber orientation, a large aspect ratio tube was modeled for radii of the two problems considered below. The

straight tube extrudate swell having an inlet diameter equal to that of a typical desktop FDM nozzle exit, and the FDM nozzle having an inlet with a diameter of a typical desktop FDM filament. The geometry and boundary conditions are shown in Figure 4.2.

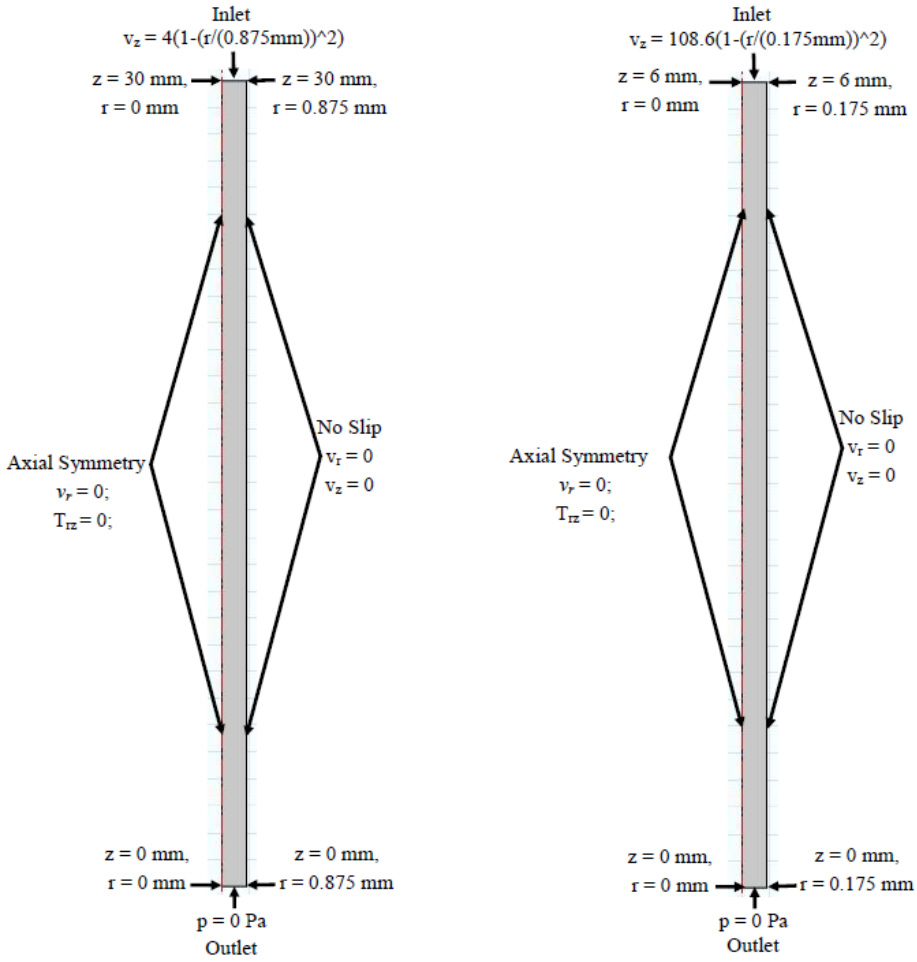

Figure 4.2. Geometry and Boundary Conditions for the Pure Shear Steady State Fiber Orientation Calculation

The mesh for the pure shear steady state fiber orientation tube geometry is shown in Figure 4.3. The mesh contains 202,664 domain elements, 5,418 boundary elements, and 1,837,524 degrees of freedom.

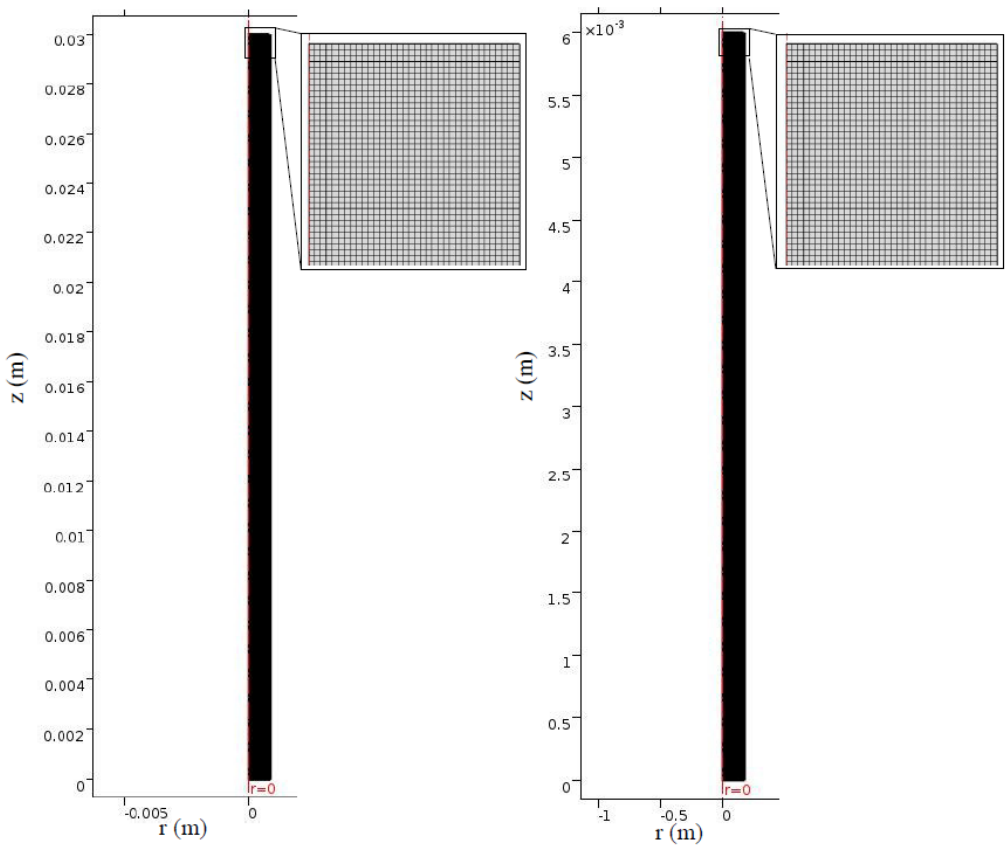

Figure 4.3. Mesh for the Pure Shear Steady State Fiber Orientation Calculation Geometries

The ten equally spaced streamlines used in the velocity pressure solution are shown in Figure 4.4. The computation time for the pure shear steady state fiber orientation tube problem is 139 seconds.

For this fiber orientation model the calculation is initialized with an isotropic orientation state; therefore, $\boldsymbol{A}$ and $\boldsymbol{B}$ are defined as the following

$$\boldsymbol{A} = \begin{bmatrix} 1/3 & 0 & 0 \\ 0 & 1/3 & 0 \\ 0 & 0 & 1/3 \end{bmatrix} \text{ and } \boldsymbol{B} = \begin{bmatrix} 1 & 0 & 0 \\ 0 & 1 & 0 \\ 0 & 0 & 1 \end{bmatrix} \tag{4.7}$$

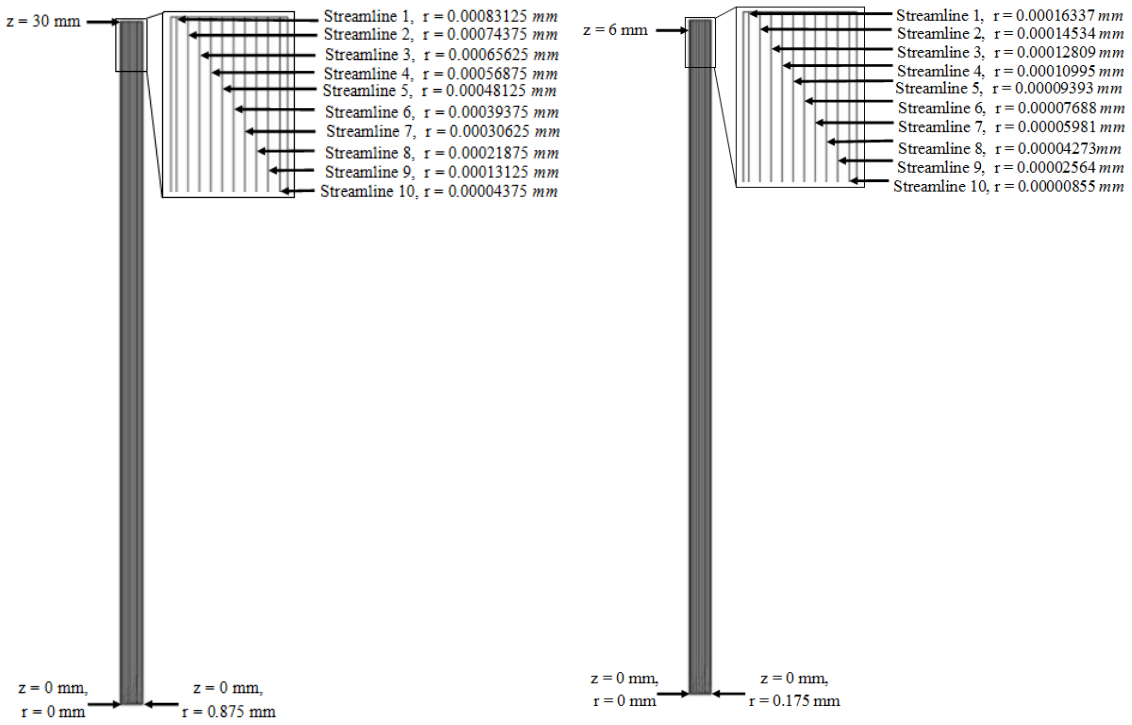

Figure 4.4. Streamlines for Solution of Pure Shear Steady State Calculation

The interaction coefficient C_I is set to 0.0075 which is in an acceptable range for a concentrated fiber suspension (see e.g. [40, 36]) and the coefficient $\lambda = 1$ which describes an infinite fiber aspect ratio.

The pure shear steady state fiber orientation was then calculated for both the 1.75 *mm* and 0.35 *mm* diameter tubes. The calculated pure shear steady state fiber orientation for both tubes values were identical. It was also found that as long as the laminar profile was maintained that the magnitude of the velocity or velocity gradients did not affect the pure shear steady state orientation. Changing the inlet velocity was found to affect the rate of change of alignment of the fibers, where an increase in mean velocity would increase the rate of alignment. The results from the pure shear transient calculation of the extrudate swell and FDM nozzle are shown in Figure 4.5 and Figure 4.6 below.

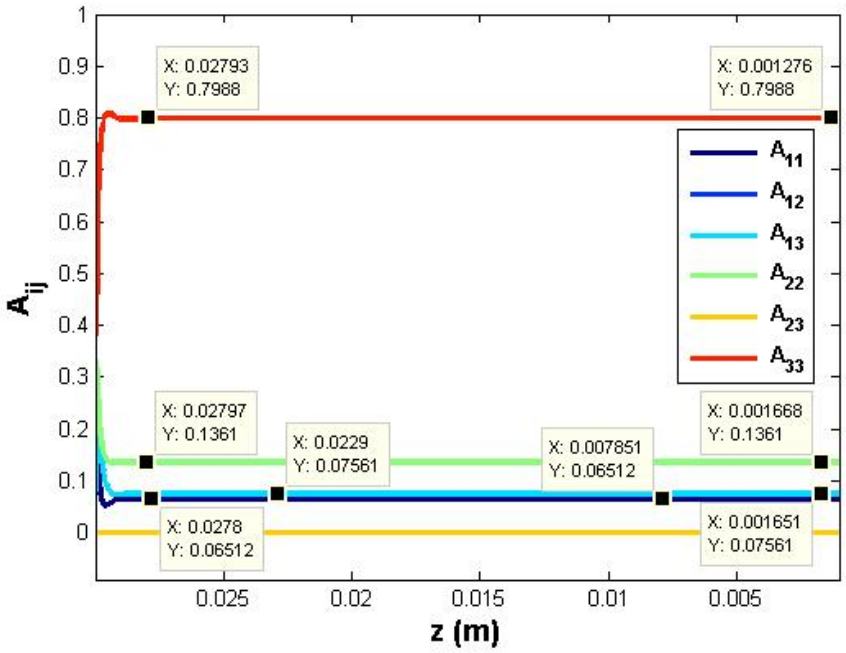

Figure 4.5. Pure Shear Steady State Values for **A** along Streamline 1, x values in bulleted points correspond to values of z, y values correspond to values of A_{ij}

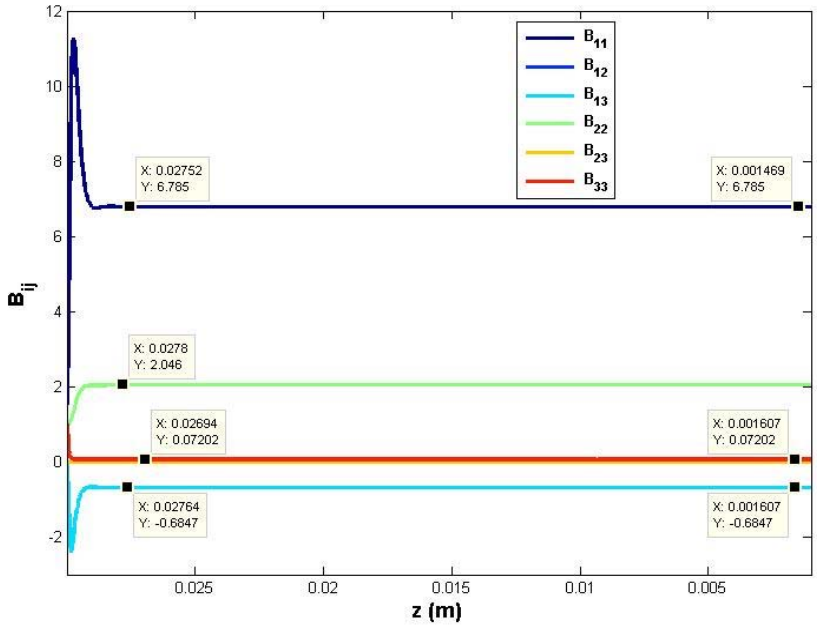

Figure 4.6. Pure Shear Steady State Values for ***B*** Tensor along Streamline 1, x values in bulleted points correspond to values of z, y values correspond to values of B_{ij}

The ‘y’ values of the points captured in Figure 4.6 are the pure shear steady state values of each component of the orientation tensor $\boldsymbol{A}$ and the associated tensor $\boldsymbol{B}$. The tensor forms of the steady state values shown in Figure 4.6 are calculated as

$$\boldsymbol{A} = \begin{bmatrix} 0.06512 & 0 & 0.07561 \\ 0 & 0.1361 & 0 \\ 0.07561 & 0 & 0.7988 \end{bmatrix} \quad \boldsymbol{B} = \begin{bmatrix} 6.785 & 0 & -0.6847 \\ 0 & 2.046 & 0 \\ -0.6847 & 0 & 0.07202 \end{bmatrix} \tag{4.26}$$

To verify the calculated pure shear steady state values in equation (4.26), for $\boldsymbol{A}$ and $\boldsymbol{B}$ in the simulation of straight tube flow where the tube is long compared to its diameter. The results for the pure shear steady state calculation agreed exactly with the previously calculated pure shear steady state inlet values shown in Figure 4.7.

The pure shear steady state values shown in equation (4.26) will be used as the inlet orientation for all of the following fiber orientation calculations.

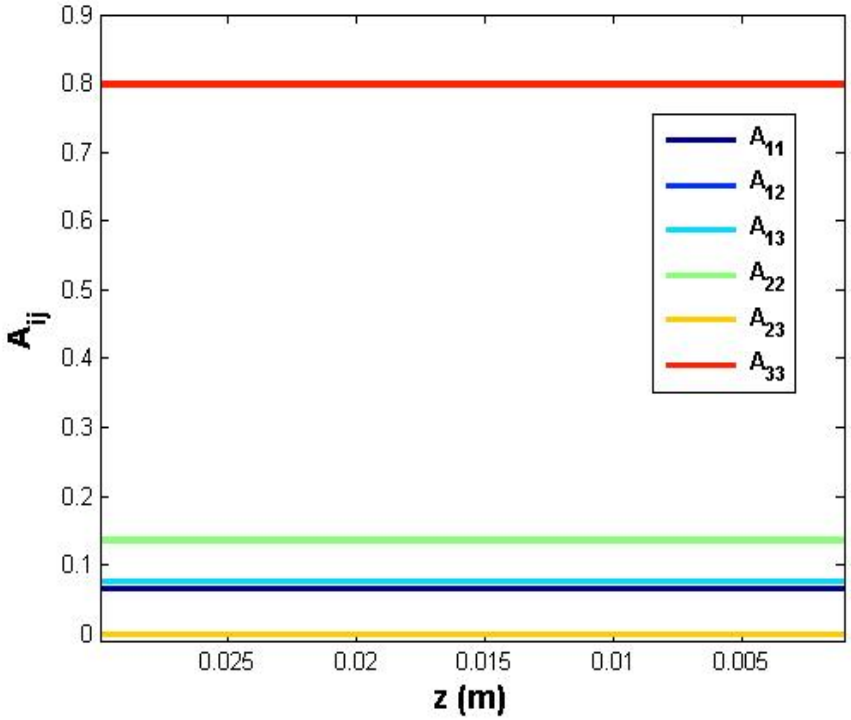

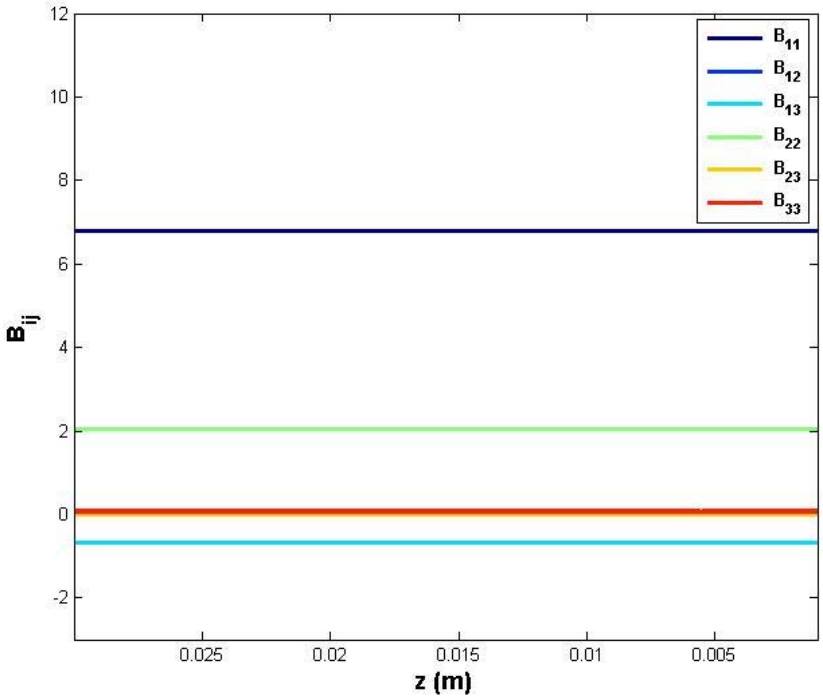

Figure 4.7. Pure Shear Steady State Inlet Orientation Values Check

4.3 Fiber Orientation Results in the Straight Tube Model

The first fluid domain geometry considered in this study is a straight 0.175 *mm* diameter tube that includes extrudate swell at its exit. This study was run to see the effects of the expansion flow in the extrudate swell region on the fiber orientation. The optimum extrudate swell free surface was computed using the minimization process described in Chapter Three. In post processing ten streamlines were added that originate at the outlet boundary and are equally spaced at the outlet only as is seen in Figure 4.8.

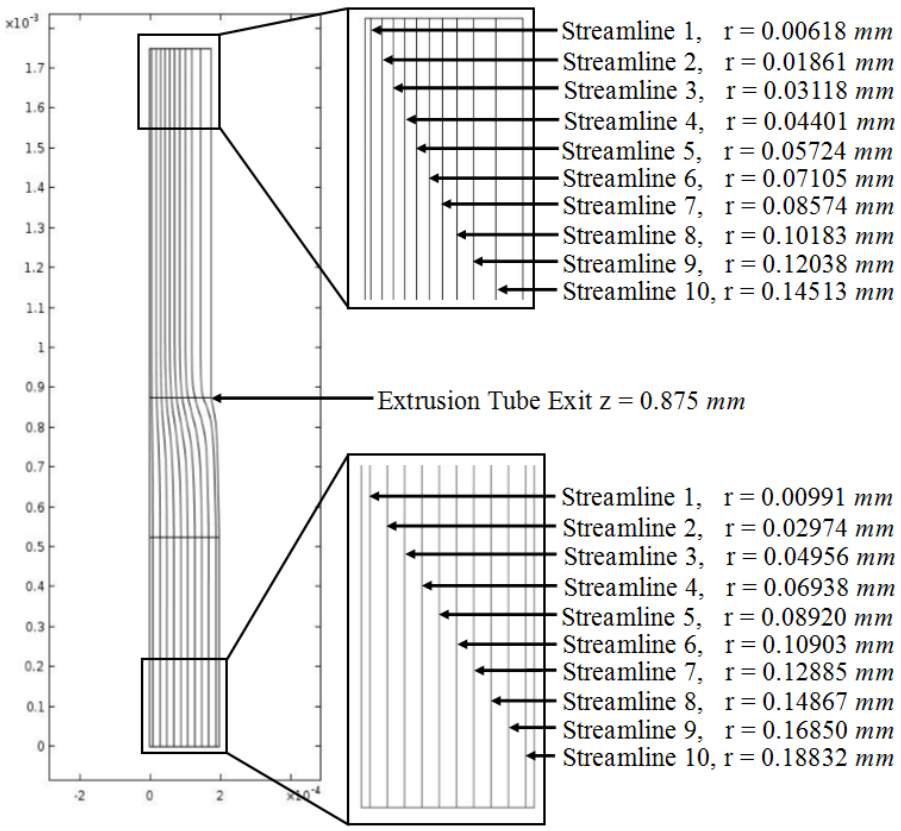

Figure 4.8. Streamlines Defined in Straight Tube Extrudate Swell Problem

Figures 4.10-15 illustrate the effect of extrudate swell on fiber orientation in the polymer melt. In Figures 4.10-15 **NE** represents the beginning of the extrudate swell at the exit of the extrusion tube.

In Figure 4.9, the components of the orientation tensor ***A*** are shown along the length of Streamline 1. Streamline 1 was chosen as an example of the fiber orientation tensor components along the interior of the fluid domain.

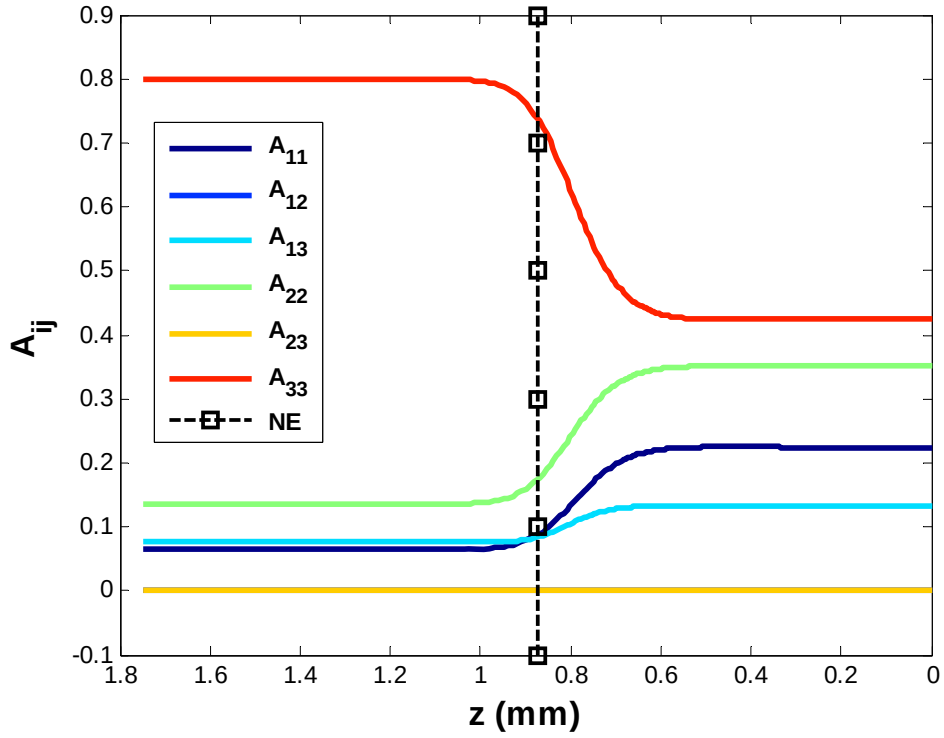

Figure 4.9. Fiber Orientation Tensor Components along Streamline 1

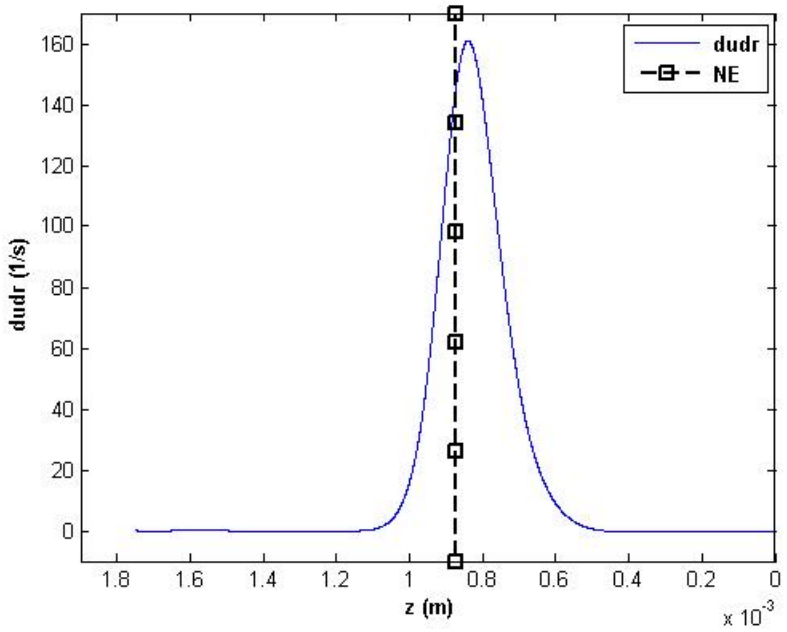

(a)

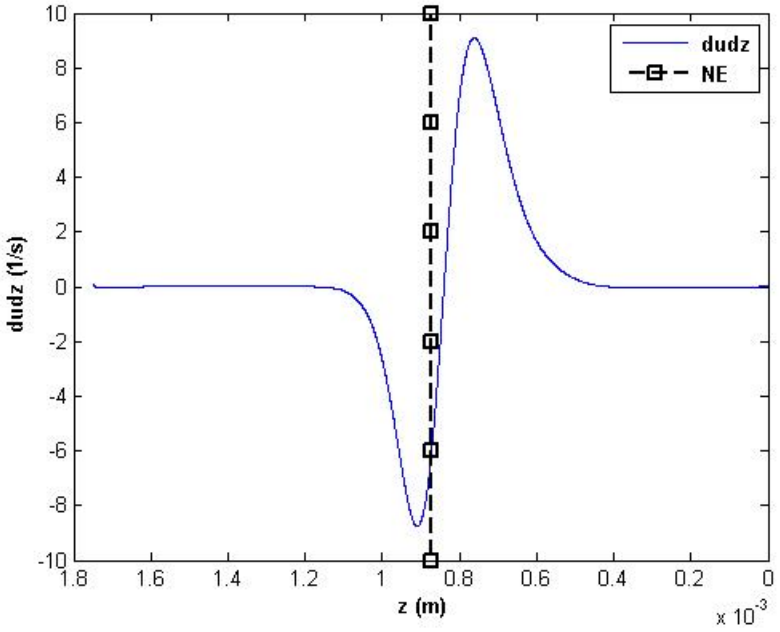

(b)

Figure 4.10. Velocity Gradients for Streamline 1

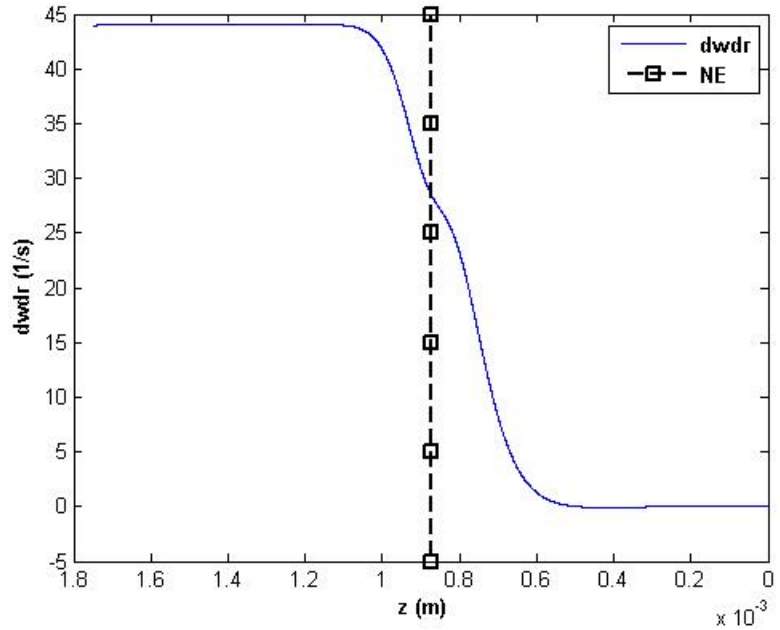

(c)

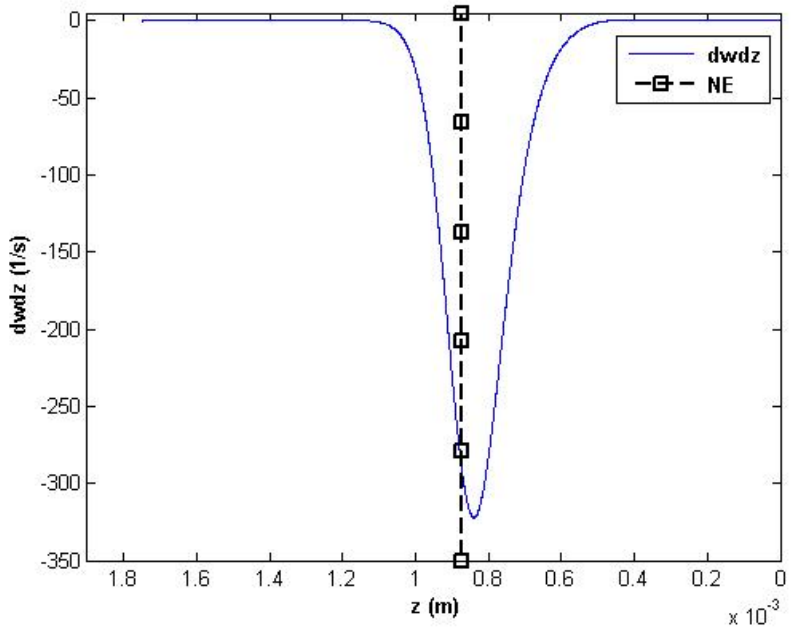

(d)

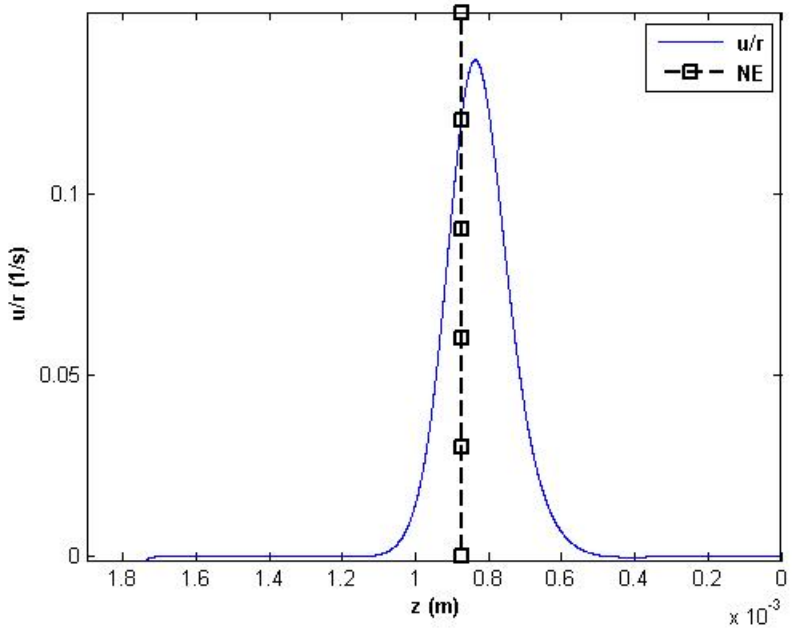

(e)

Figure 4.11. Velocity Gradients for Streamline 1

Figure 4.9 shows that the fiber orientation within the tube remains at the pure shear steady state value calculated in Section 4.3.2 with $A_{33} = 0.7988$. This orientation defines a highly aligned state in the z direction. Near z = 0.875 *mm* where the extrudate

swells after leaving the extrusion tube (see Figure 4.8) there is a significant decrease in the A_{33} component. The decrease in the A_{33} component can be explained by looking at the velocity gradients in the polymer melt flow. The velocity gradients along Streamline 1 are shown in Figure 4.10 and Figure 4.11. Figure 4.11 (d) shows a rapid decrease in the $\frac{\partial w}{\partial z}$ component caused by a flow that is slowing in the z direction at the extrusion tube exit. This is called a contraction flow and causes a decrease in alignment transverse to the flow [42, 43, 44]. Figure 4.9 (a) shows that $\frac{\partial u}{\partial r}$ increases at the exit which increases a fibers tendency to orient in the direction transverse to the flow. This results from the condition that expansion flows also serves to decrease fiber alignment in the direction of the flow. The increase in the alignment transverse to the flow caused by the contraction flow is recognized also by the increase in the A_{11} and A_{22} component's which indicate the amount of alignment in the r and z directions, respectively.

The velocity gradients seen along the outer edge of the extrusion tube are much different than those in the interior of the extrusion tube flow. To understand the effects of the outer edge of the extrusion tube the components of the fiber orientation tensor for streamline 10, shown in Figure 4.10, are studied.

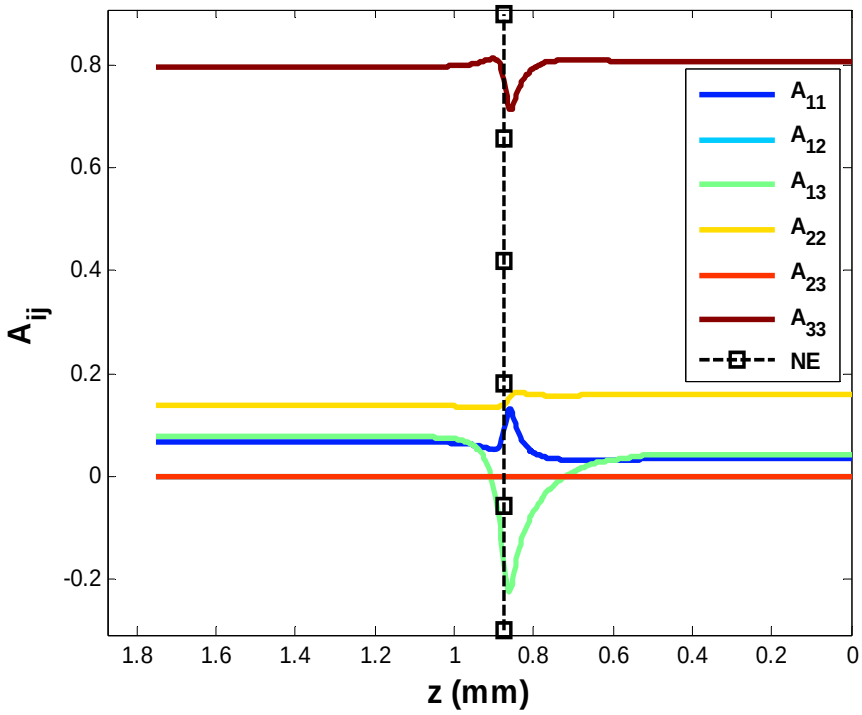

Figure 4.12. Fiber Orientation Tensor Components along Streamline 10

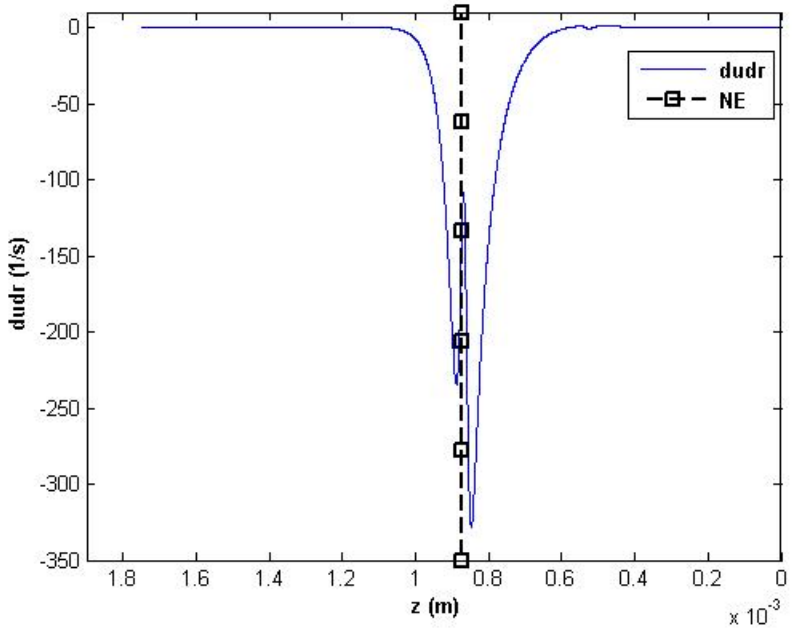

(a)

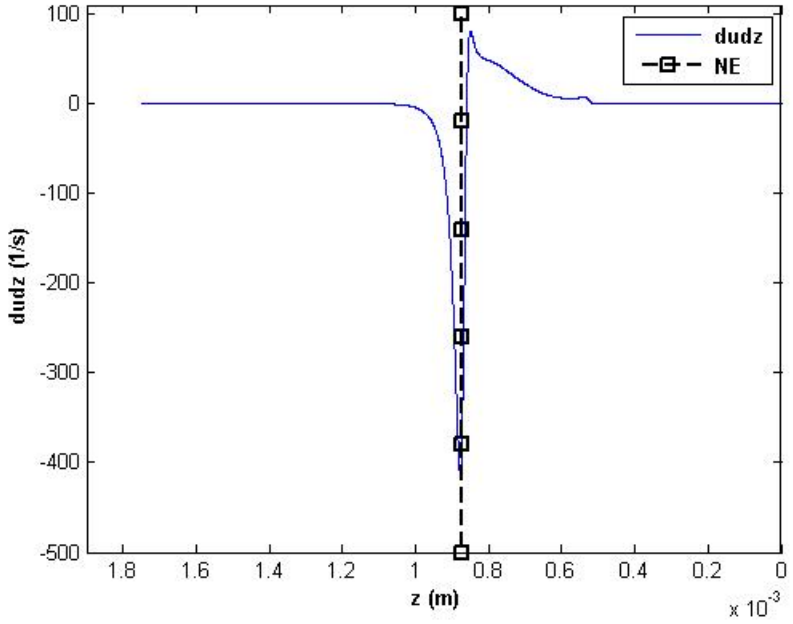

(b)

Figure 4.13. Velocity Gradients for Streamline 10

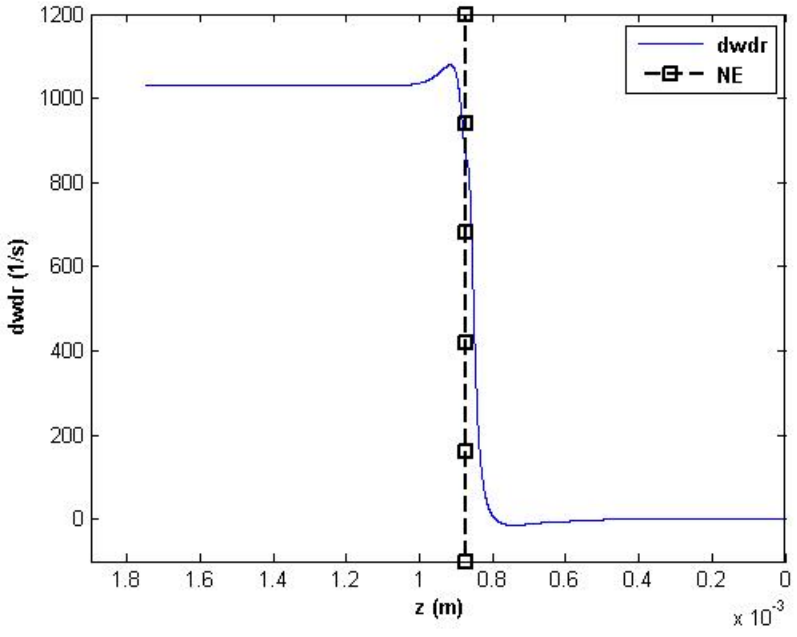

(c)

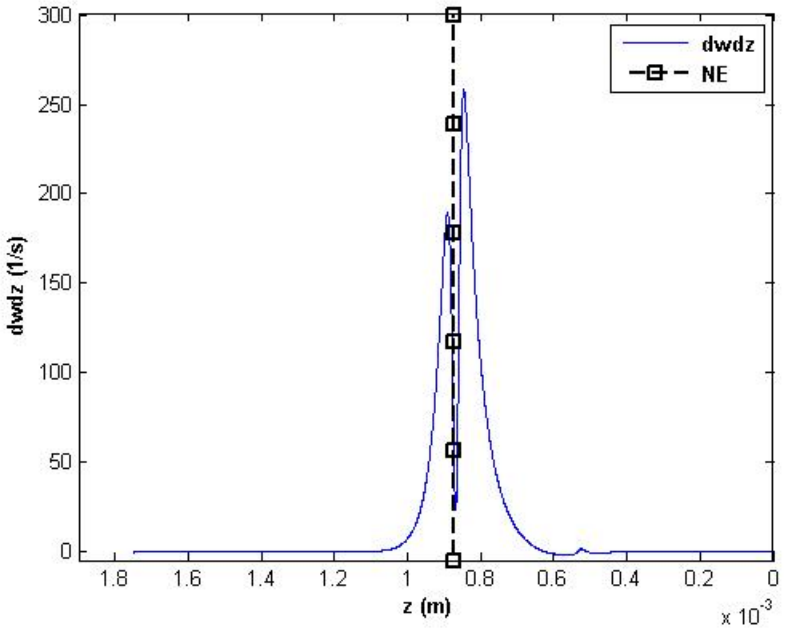

(d)

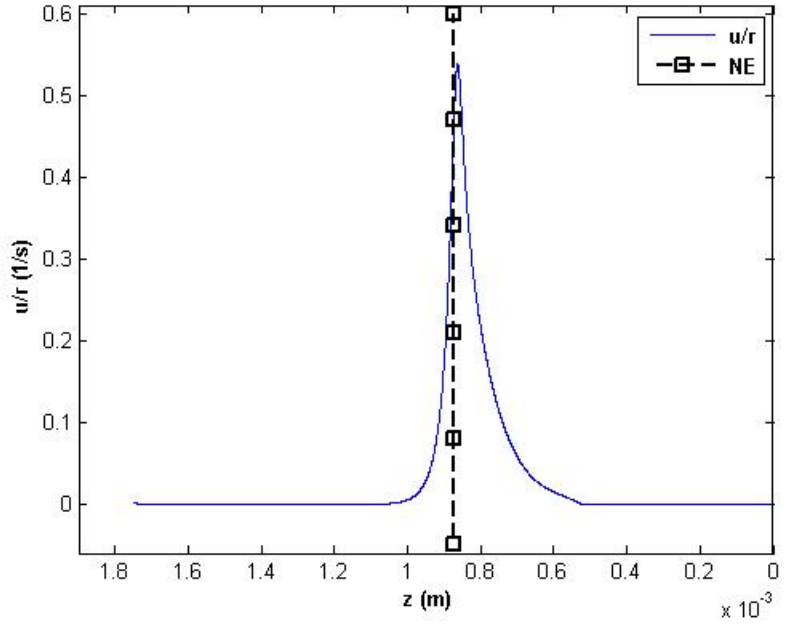

(e)

Figure 4.14. Velocity Gradients for Streamline 10

Figure 4.12 shows the effects at the outer wall of the nozzle. An increase in A_{33} followed by a large decrease is seen near the extrusion tube exit, which is then followed by a return to a value near the pure shear steady state. The changes in the A_{33} component

can be explained by looking at the velocity gradients in the polymer melt flow. The velocity gradients along Streamline 1 are shown in Figure 4.13 and Figure 4.14. The effects seen in Figure 4.12 are caused by a flow that is first driven by a large shear rate, shown in Figure 4.14 (c), which increases as does A_{33} right before the extrusion nozzle exit. Immediately before and for a small distance after the extrusion exit the flow becomes mostly an expansion flow defined by $\frac{\partial u}{\partial r}$. Because the magnitude of $\frac{\partial w}{\partial z}$ is smaller than $\frac{\partial u}{\partial r}$ the expansion flow causes a decrease in alignment in the direction of the flow and increases the alignment transverse to the flow. This is seen by a decrease in A_{33} and an increase in A_{11} at the nozzle exit. The orientation tensor then returns to an alignment value near the pure shear steady state due to the $\frac{\partial u}{\partial z}$ and $\frac{\partial w}{\partial r}$shear components that remain shortly after gradients that define elongation $\frac{\partial w}{\partial z}$ and expansion $\frac{\partial u}{\partial r}$ flow return to zero.

Figure 4.15 illustrates the A_{33} component for all ten streamlines that define the velocities and velocity gradients along each streamline from the flow domain entrance to exit. Figure 4.15 provides insight into the amount of fiber alignment along the length of the nozzle and across the width of the nozzle at the 10 discrete streamlines that are plotted.

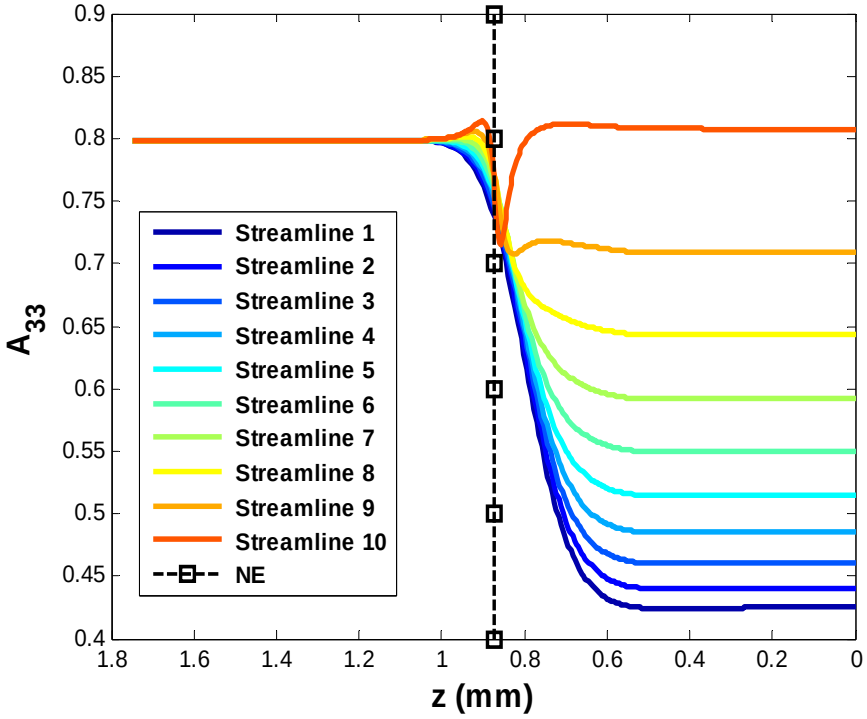

Figure 4.15. A_{33} Component of the Orientation Tensor along Streamlines in the Fluid Domain

Figure 4.15 shows that a decrease in the A_{33} component of fiber orientation at the extrusion tube exit occurs for streamlines 1-9. This is due to the large expansion velocity gradients in the polymer melt as it leaves the extrusion tube exit and becomes a free jet. The velocity in the tube is greatest at the center near streamline 1; therefore, the effect of the velocity decrease on fiber orientation is strongest along this streamline. The velocity gradients decrease in the radial direction from streamline 1 to streamline 9. The behavior of streamline 10 is different from the others in the fluid domain. This effect appears to result from a small but rapid increase in the A_{33} component followed by a larger rapid decrease and finally a return to a value near the pure shear steady state A_{33} value. This behavior is also seen to effect streamline 9 but the effect is much smaller.

The fiber orientation state along streamline 10 returns to approximately the pure shear steady state orientation value calculated in Section 4.3. Due to the low velocity and high velocity gradients at the edge of the extrusion tube there is little change in the fiber orientation due to a change in velocity gradient from the no slip wall to the free stream flow.

The most important part of the fiber orientation study is the final orientation state after the polymer melt has left the nozzle. Figure 4.15 illustrates that the fiber orientation reaches a steady state after exiting the extrusion tube due to the absence of velocity gradients in the free stream flow. Figure 4.16 shows the value of the A_{33} component of the orientation tensor immediately after the orientation reaches steady state in the swollen polymer melt. This figure shows what is expected to be the orientation of the fibers in the printed bead.

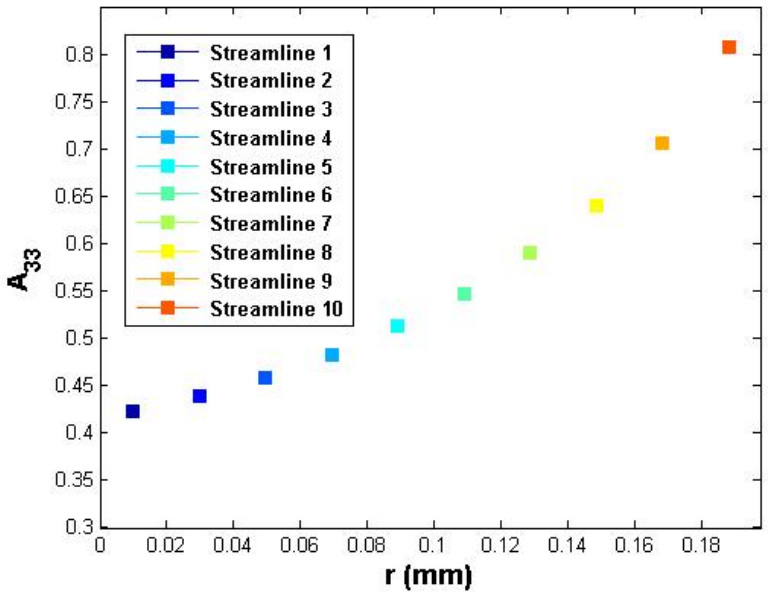

Figure 4.16. Fiber Orientation for the Straight Tube A_{33} Component at the Extrusion Tube Exit

The orientation state for the defined fluid flow is shown in Figure 4.16. It can be seen that the orientation of the fibers decreases from streamline 10 to streamline 1. This decrease can be attributed to the change in velocity gradients previously discussed.

4.4 Fiber Orientation Results in an FDM Nozzle

This section considers the fiber orientation as polymer melt passes through the fluid domain of a FDM nozzle. The common nozzle geometry and the extrudate swell free surface shape described in Section 3.4.2 will be used in this study. Ten streamlines that are evenly spaced at the outlet are evaluated in COMSOL where the velocity, and velocity gradients are obtained for further analysis. The fluid domain showing the streamlines of a typical analysis is shown in Figure 4.17. The fiber orientation calculation described above is used to compute the second-order fiber orientation tensor at points along each streamline.

Results from the solution to the fiber orientation equation appearing in Figure 4.18-22 show the effects of the converging nozzle and the extrudate swell free surface. For this study the fluid domain is extended 5 radii beyond the extrusion nozzle exit to allow for the calculation of the effect of extrudate swell to be included. In Figure 4.18-22 **CZS** represents the start of the convergence zone of the nozzle, **CZE** represents the end of the convergence zone, and **NE** represents the extrusion nozzle exit. The location of **CZS**, **CZE**, and **NE** are shown in Figure 4.17. In Figure 4.18, the components of the orientation tensor $\boldsymbol{A}$ are shown along the length of Streamline 1. Streamline 1 was chosen as an example of the fiber orientation tensor components along the interior of the fluid domain.

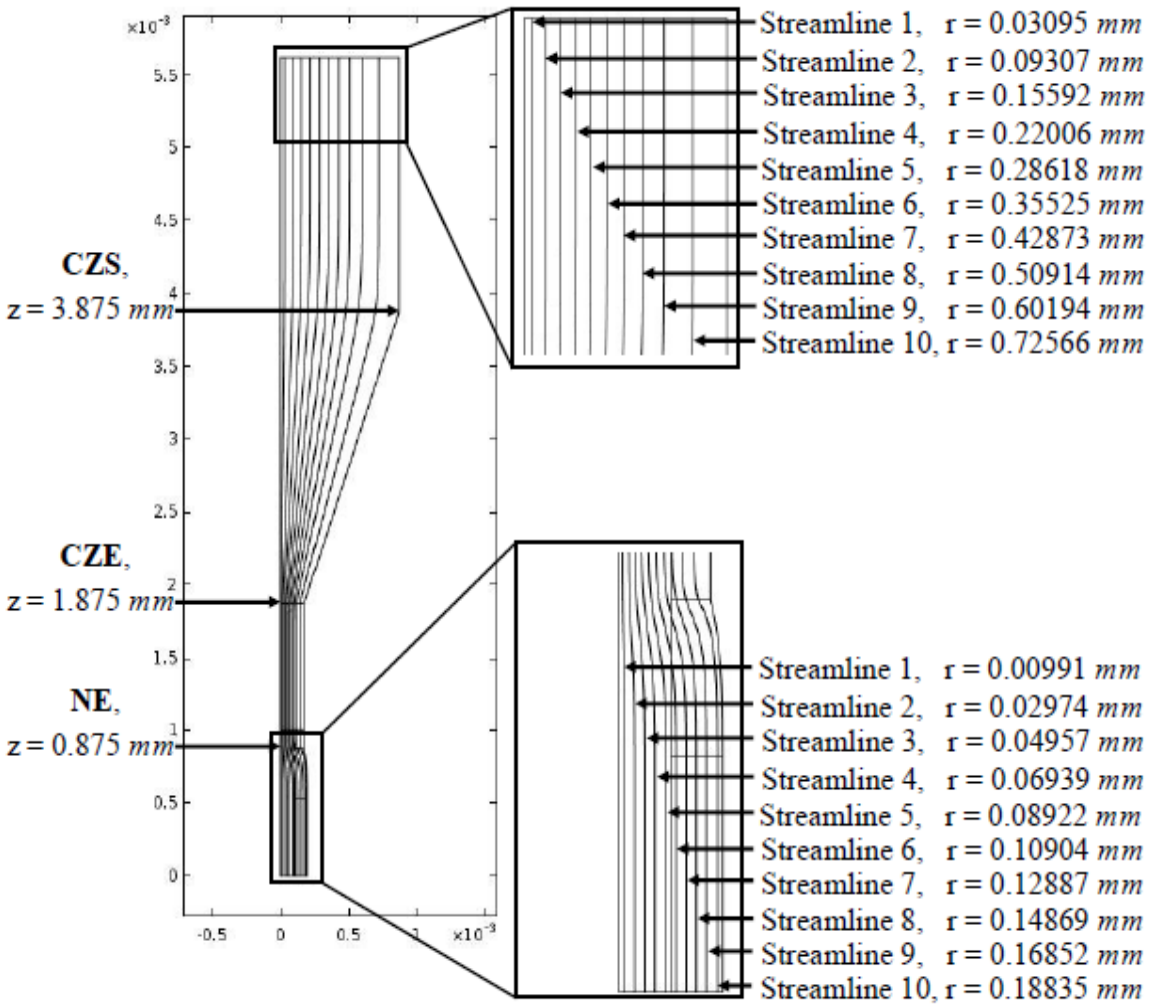

Figure 4.17. Streamlines for the FDM Nozzle Fluid Domain

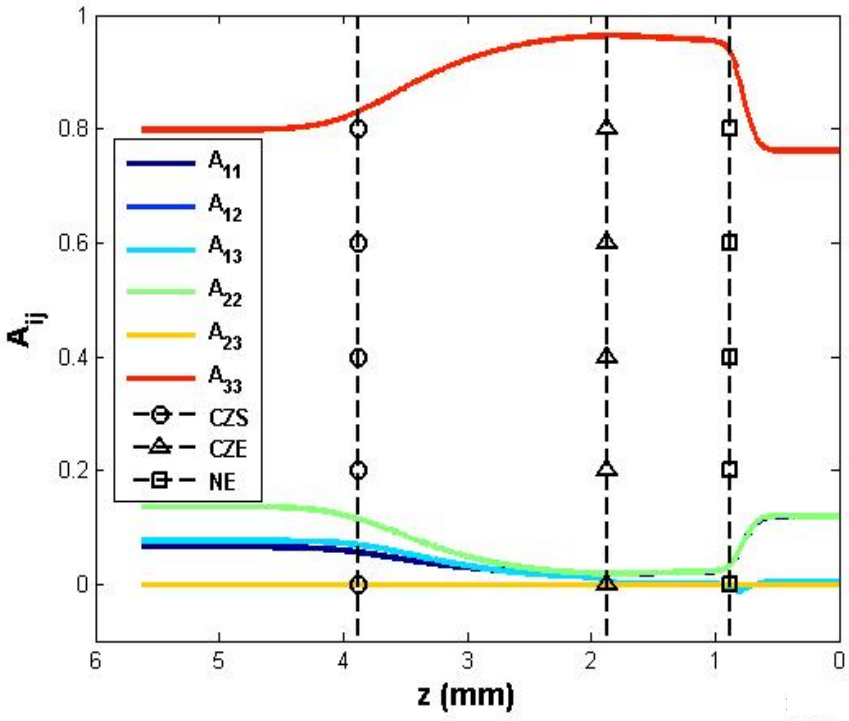

Figure 4.18. Components of the Fiber Orientation Tensor A along Streamline 1 for FDM nozzle

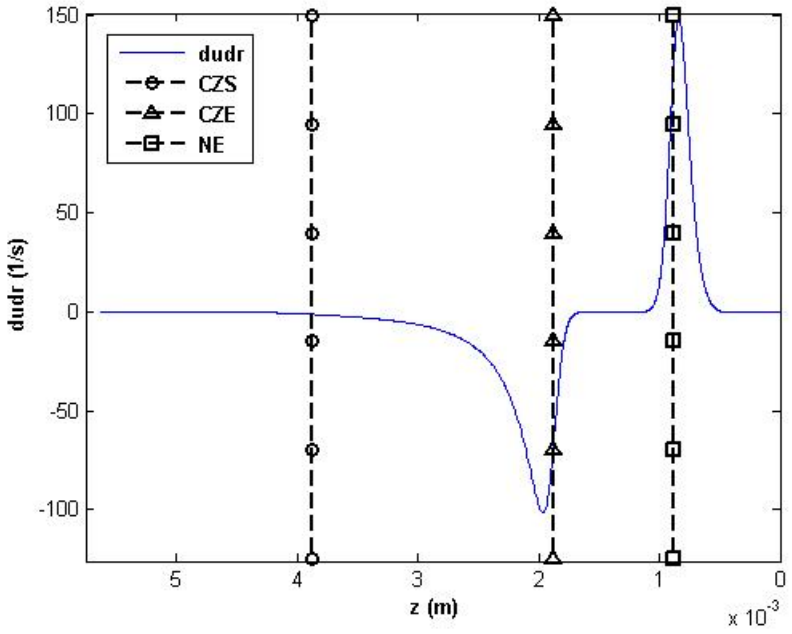

(a)

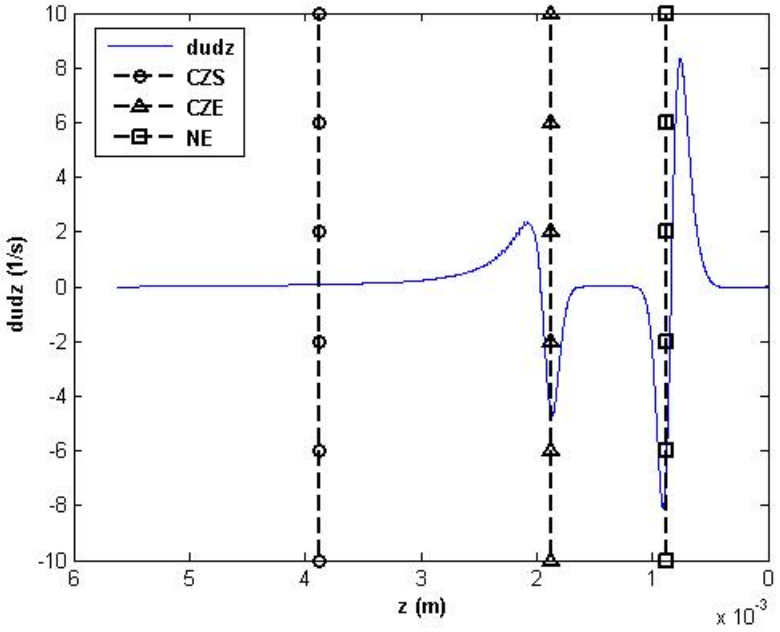

(b)

Figure 4.19. Velocity Gradietns for Streamline 1 of the FDM Nozzle Flow

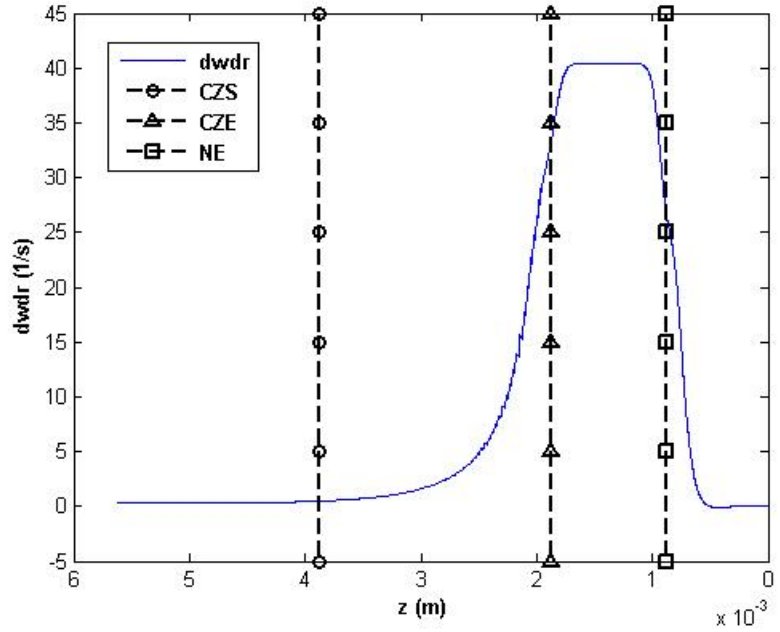

(c)

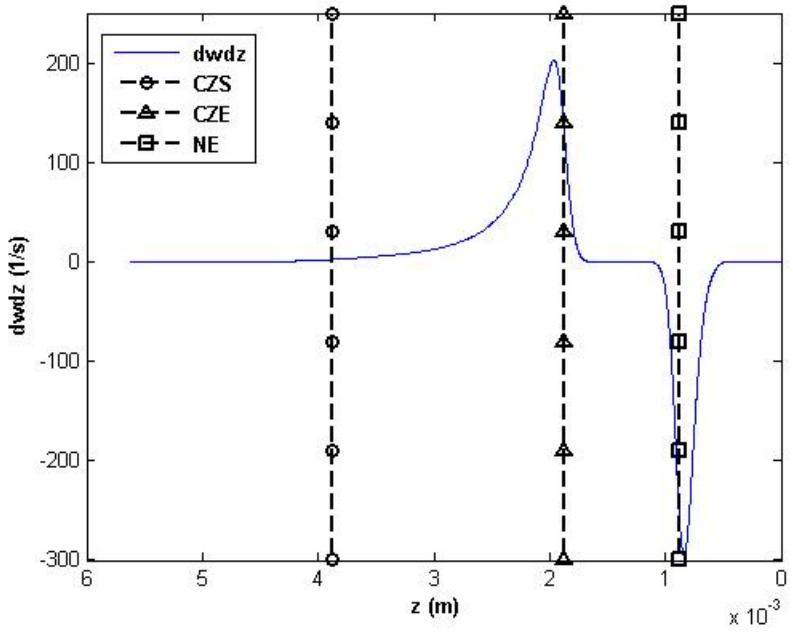

(d)

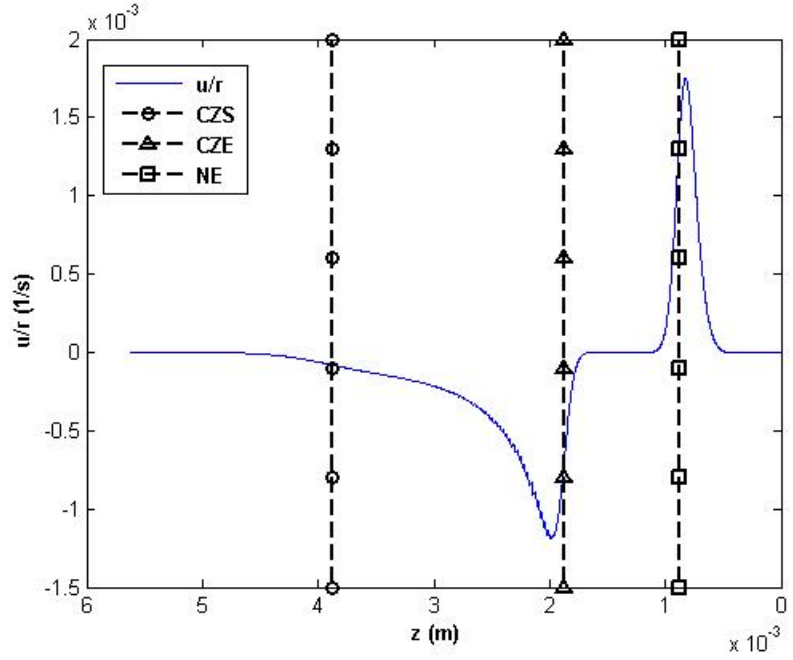

(e)

Figure 4.20. Velocity Gradients for Streamline 1 of the FDM Nozzle Flow

Figure 4.18 shows the effects of the interior of the FDM nozzle geometry on the fiber orientation tensor ***A*** at Streamline 1. Figure 4.18 shows that the A_{33} component of the orientation tensor increases in the convergence zone which spans from **CZS** to **CZE**.

This increase in fiber orientation is due to elongation flow which is defined by an increase in $\frac{\partial w}{\partial z}$ as seen in Figure 4.20 (d). The velocity gradient,$\frac{\partial w}{\partial z}$ starts to increase before the convergence zone begins which causes a similar increase in the A_{33} component slightly before the convergence zone. Immediately after the end of the convergence zone, in the straight portion of the nozzle, there is a decrease in the A_{33} component which can be related to the velocity gradients shown in Figure 4.20 (a-e). All velocity gradients return to their steady state values in this region of the nozzle which results in the fibers orientation beginning a return to pure shear steady state orientation. After the nozzle exit, **NE**, there is a decrease in the A_{33} component of the fiber orientation which is due to the negative elongation component, $\frac{\partial w}{\partial z}$, and an expansion flow, $\frac{\partial u}{\partial r}$, both of which decrease the alignment in the A_{33} component.

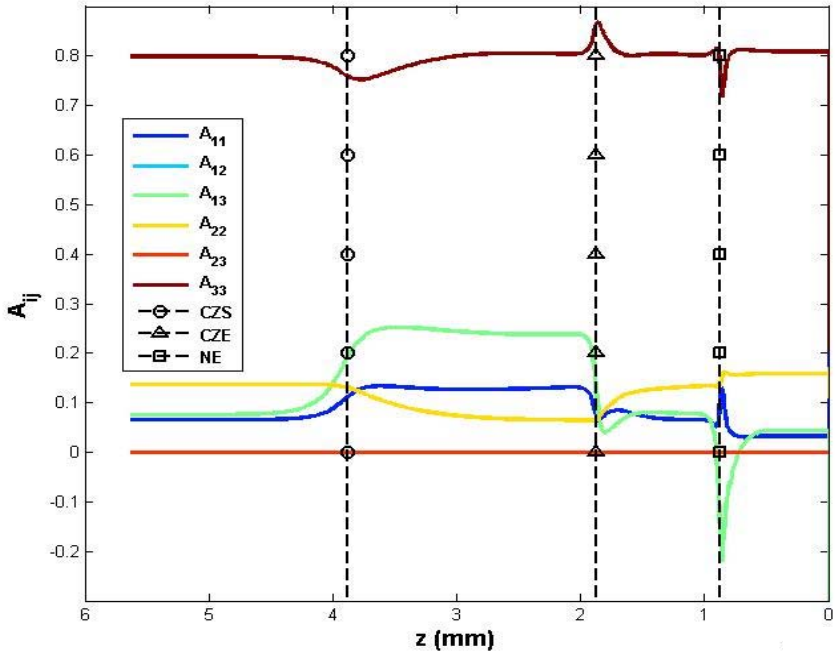

Figure 4.21. Components of the Fiber Orientation Tensor A along Streamline 10 for the FDM Nozzle

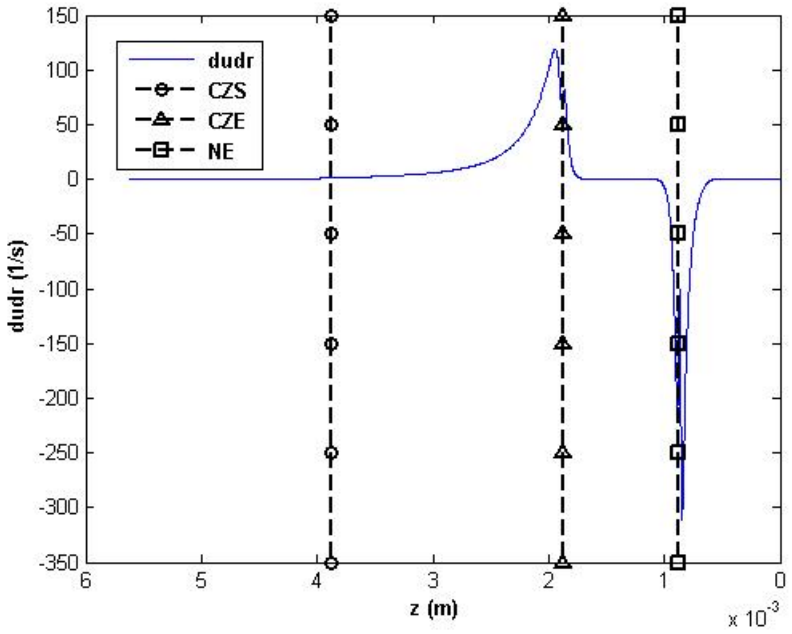

(a)

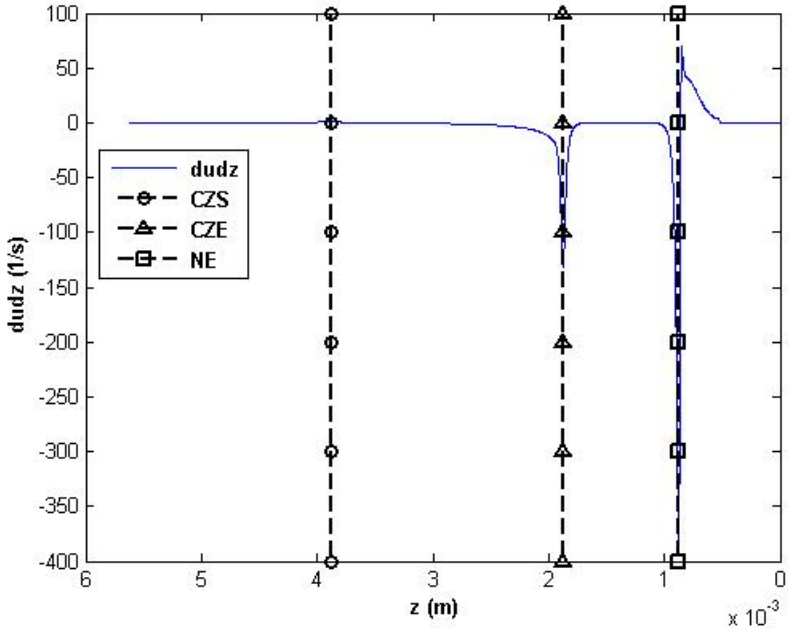

(b)

Figure 4.22. Velocity Gradients along Streamline 10 for the FDM Nozzle

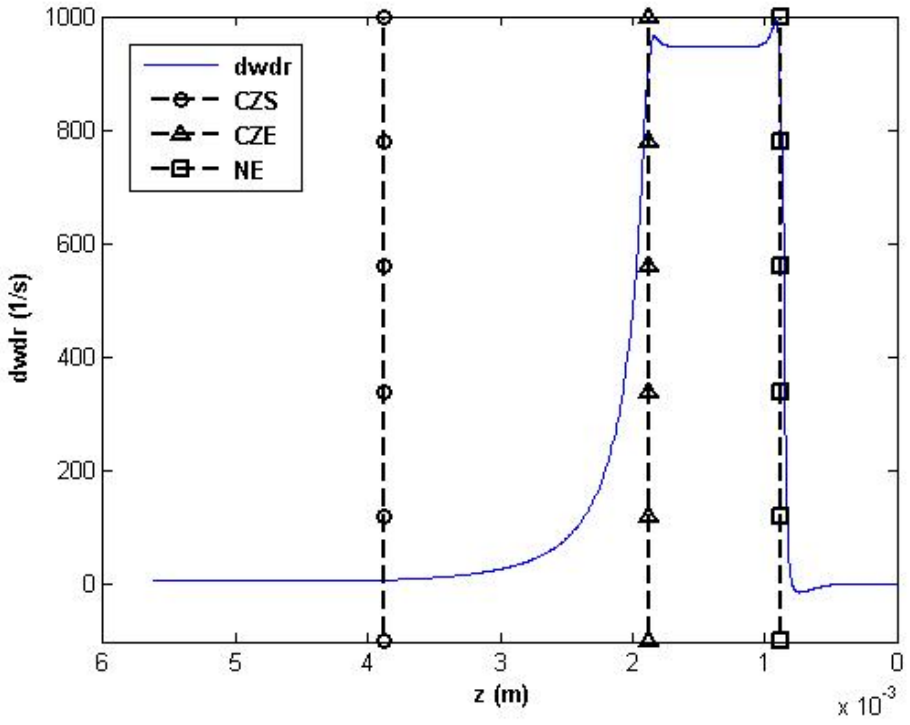

(c)

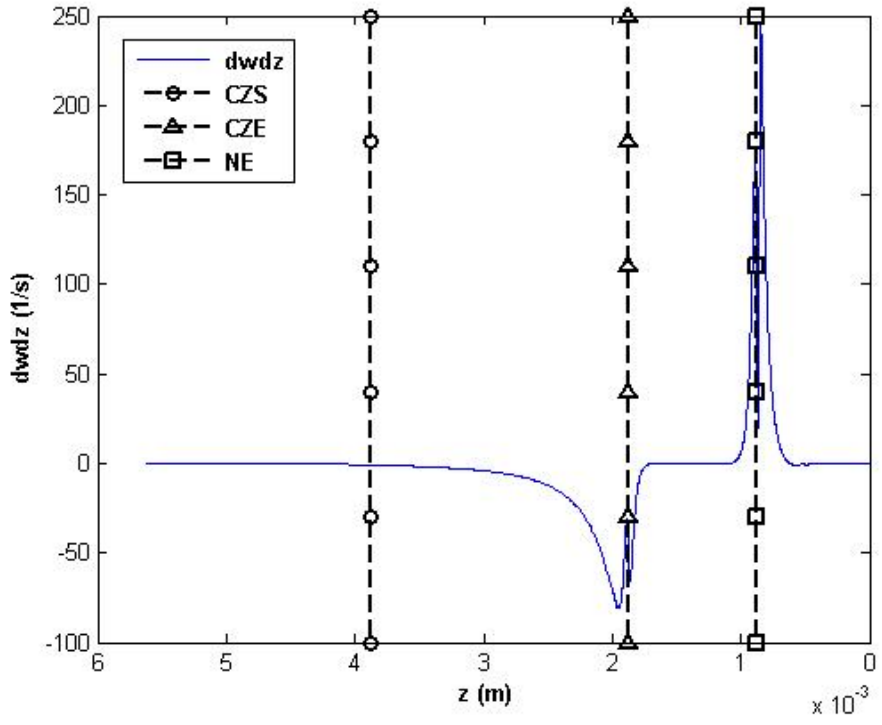

(d)

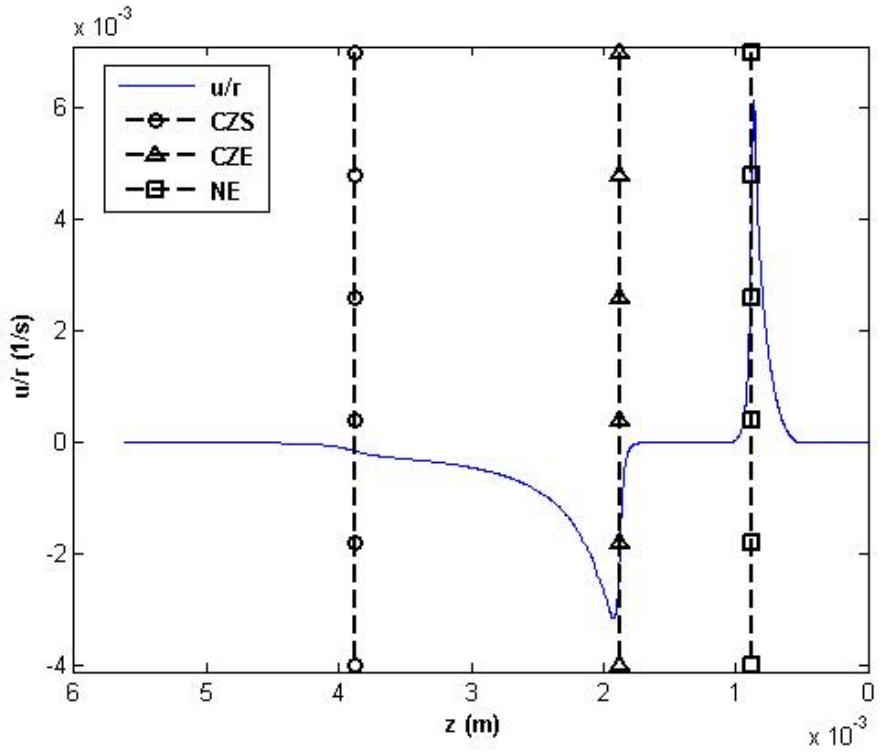

(e)

Figure 4.23. Velocity Gradients along Streamline 10 for the FDM Nozzle

The velocity gradients seen along the outer edge of the FDM nozzle differ significantly from those near the center of the nozzle. To understand the effects of the outer edge of the nozzle the components of the fiber orientation tensor for streamline 10, shown in Figure 4.21, are studied.

Six of the 9 components of the orientation tensor ***A*** are shown along the length of Streamline 10. These results indicate that there is a decrease in the A_{33} component immediately before and for a short distance after the start of the convergence zone, **CZS**, along streamline 10. This is due to an increase in the expansion flow, $\frac{\partial u}{\partial r}$, and a decrease of elongation flow, $\frac{\partial w}{\partial z}$, both of which reduce the alignment in the direction of flow, as indicated by the lower values of the A_{33} component. The expansion flow and elongation flow terms continue to increase from **CZS** to **CZE**, but the A_{33} component does not

continue to decrease. At this point the magnitude of shear in the flow increases to a point where it becomes dominant in the fluid domain. At the end of the convergence zone, **CZE**, there is a peak in the shear flow component near the maximum value of the A_{33} component of the fiber orientation tensor. Immediately after the nozzle exit there is a decrease in the A_{33} component which is caused by a decrease in the shear component in the flow. Once the polymer has passed the nozzle exit, there is a return to a value near pure shear steady state. This occurs due to the shear velocity gradients $\left(\frac{\partial u}{\partial z} \text{ and } \frac{\partial w}{\partial r}\right)$ that exist after the velocity gradients that represent elongation$\frac{\partial w}{\partial z}$ and expansion$\frac{\partial u}{\partial r}$ flow. As the extrudate travels further out of the nozzle exit and reaches a constant velocity through all of the flow field.

Figure 4.24 illustrates the amount of alignment along the z direction throughout the length of the nozzle and over the width of the nozzle along the ten streamlines that are plotted. Note that in the convergence zone of the nozzle, A_{33} reaches a value near unity, which represents a nearly uniaxial alignment in the z-direction. The maximum value of A_{33} at its peak is $A_{33} = 0.9775$ along streamline 1. It is also seen that in the straight region of the nozzle after the convergence zone that the orientation decreases towards a pure shear steady state value which is defined by the C_I and λ coefficients. At the exit of the nozzle in the region of extrudate swell there is a substantial decrease in alignment. This rapid decrease in alignment is caused by the expansion flow in the area of the extrudate swell.

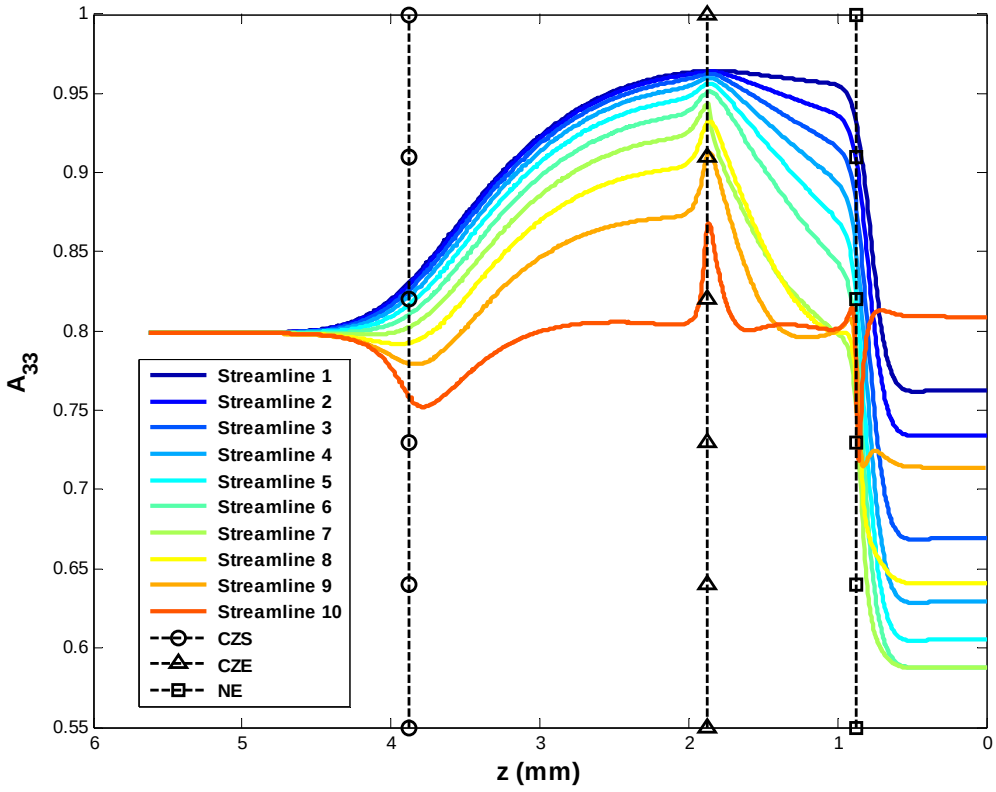

Figure 4.24. A_{33} Component of the Orientation Tensor ***A*** along All Streamlines

Figure 4.24 shows that streamlines 7-10 exhibits a slight decrease in alignment in the convergence zone of the nozzle while the remainder of the streamlines have the same increase in alignment as discussed earlier in this section. The decreasing alignment in the z direction occurs due to the expansion flow in the convergence zone of the nozzle. This is a negative expansion or contraction in the convergence zone of the nozzle which effects the alignment of the fibers. Due to the fluid moving inward in the convergence zone the fibers are influenced and the orientation in the z direction is shown to decrease. The region close to the outside wall of the nozzle has a decrease in alignment caused by the contracting flow. The decrease in the A_{33} component of the fiber orientation caused

by the expansion flow in the extrudate swell is similar to that seen in the straight tube extrudate swell model in Section 4.3.

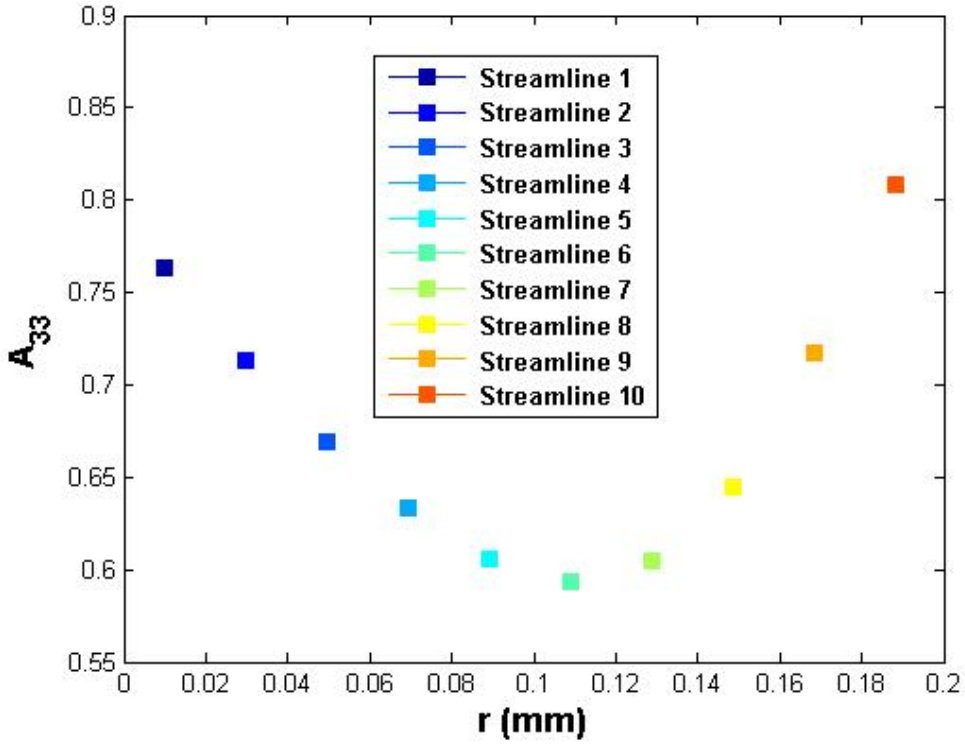

Figure 4.25. A_{33} Component of the Fiber Orientation Tensor at Steady State After Nozzle Exit

Figure 4.25 shows the value of the A_{33} immediately after the orientation reaches steady state in the expanded polymer melt. This figure is of the highest interest in this study because it shows the amount of alignment of the fibers in the polymer melt that forms the deposited bead in the FDM process.

Figure 4.25 shows that the fiber orientation is highly aligned at all radial values, with A_{33} values greater than 0.55. It is also seen that there is high alignment near the wall of the die along streamline 10 and also high degree of alignment at the center of the flow along streamline 1. There is also an obvious decline of alignment between the wall and the center of the flow.

It is interesting to consider differences between Figure 4.25 for the FDM nozzle flow and Figure 4.16 for the straight tube flow. Both results show that the extrudate swell expansion has a significant effect on the fiber orientation which decreases the A_{33} component over the entire flow front. It is noticed however that the alignment is higher for the FDM nozzle than for the straight tube flow. This is due to the increased alignment in the convergence zone of the FDM nozzle that occurs just before the straight tube portion that forms the nozzle exit, both of which serve to decrease A_{33}. As a result, the FDM nozzle geometry has a significant impact on the final orientation state of the fiber filled polymer melt that exits an FDM nozzle. Further, these results indicate that the geometry of the FDM nozzle can be changed to create a desired final orientation state in an FDM printed part.

CHAPTER FIVE

Nozzle Geometry Parametric Study

A computational approach was presented in Chapter Three to obtain the extrudate swell surface and the fiber orientation through the fluid domain for an axisymmetric polymer melt flow. In addition, calculations in Chapter Four shows that the geometry of a standard FDM nozzle can be modified to influence the fiber orientation in the extruded bead. This is important to the mechanical performance of an FDM printed short fiber composite since the fiber orientation in an extruded bead defines the material properties of the final printed part. Highly aligned fibers provide high stiffness and strength in the direction of alignment, but add little or no strength in other planes, whereas an isotropic orientation state increases the strength in all planes but by a lesser amount. The ability to define the final orientation of the fiber suspension by changing the nozzle flow field geometry is of interest. In this chapter, a parametric study is presented to show the effects of nozzle geometry on fiber orientation at the exit of an FDM nozzle.

5.1 Calculation of Average Exit Fiber Orientation

To compare the results for various FDM nozzle geometries, a single valued orientation metric is needed to quantify the fiber orientation state downstream of the nozzle exit. In this study, the average value of the A_{33} component of the orientation tensor at steady state after the nozzle exit will be used to define the amount of alignment in the extruded polymer bead. Values of A_{33} downstream of the nozzle exit appeared in Chapter Four, Figure 4.16 and Figure 4.25, as a single value for each of the ten

streamlines. These ten values are used here to compute the average $\bar{A}_{33}$ across the extruded bead using numerical integration along the radial dimension of the axisymmetric flow domain. The integrated A_{33} across the melt flow area is divided by the area of the circular extrudate to obtain the average $\bar{A}_{33}$. The numerical integration used here is a Simpson's 3/8 rule for 10 points and nine segments and is given as

$$\bar{A}_{33} = \frac{2}{(r_{outer}^2 - r_{inner}^2)} I \tag{5.1}$$

where r_{outer} is the radial value of streamline 10, r_{inner} is the radial value of streamline 1, and I is the numerically integrated area under the curve given as

$$I = \frac{3}{8} h[F_1 + 3F_2 + 3F_3 + 2F_4 + 3F_5 + 3F_6 + 2F_7 + 3F_8 + 3F_9 + F_{10}] \tag{5.2}$$

For equation (5.2) F_i is defined as

$$F_i = A_{33,i} r_i \; for \; i = 1{:}\,10 \tag{5.3}$$

and h is defined as

$$h = \frac{r_{outer} - r_{inner}}{n} \tag{5.4}$$

where n is the number of segments being integrated.

Figure 4.16 and Figure 4.25, as well as equation (5.1), show that the integration is not performed over the entire exit cross section. A small section near the interior axisymmetric boundary and near the exterior free surface boundary of the domain is not considered. As a result, equation (5.1) only approximates the average A_{33} over a portion of the flow domain, but the change in value is expected to be small. In addition, all of the results given below use the same $\bar{A}_{33}$ integration domain which provides for a good comparison for the geometric parameters considered.

5.2 Parametric Studies

Two parametric studies were conducted to evaluate the effect of nozzle geometry on the average alignment value, $\bar{A}_{33}$, at a steady state downstream of the nozzle exit. Four parameters that define the shape of the inner nozzle geometry in Figure 5.1 are used for the parametric study: length of the convergence zone (A), length of the straight portion of the nozzle (B), length of the expanding nozzle (C), and amount of expansion of the nozzle exit (D).

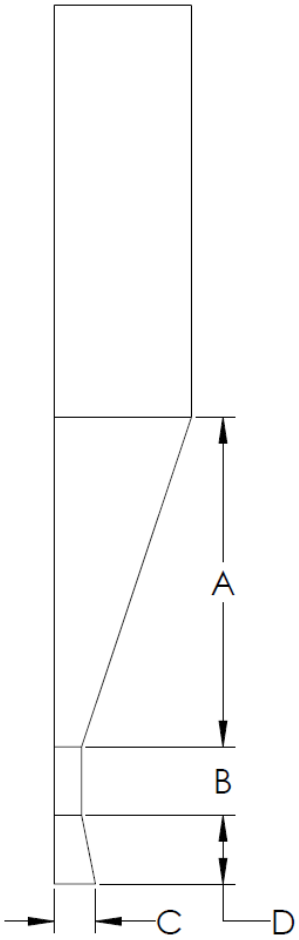

Figure 5.1. Definition of Nozzle Geometry Shape Parameters

5.2.1 Parametric Study of Nozzle Upstream Shape

The first parametric study evaluates the effect of the length of the convergence zone (A) and the length of the straight portion of the nozzle (B) on the amount of fiber alignment. Values of parameters A and B used for this study are

$$A = 5, 7, 9, 11, 13, and\ 15\ radii$$
$$B = 0.1, 2, 4, 6, 8, and\ 10\ radii \quad (5.5)$$

This allows for thirty-six different nozzle geometry tests to be run. Other dimensions for the nozzle geometry include C = 0, D = 0, an inlet and outlet diameter of 0.875 *mm* and 0.175 *mm* respectively.

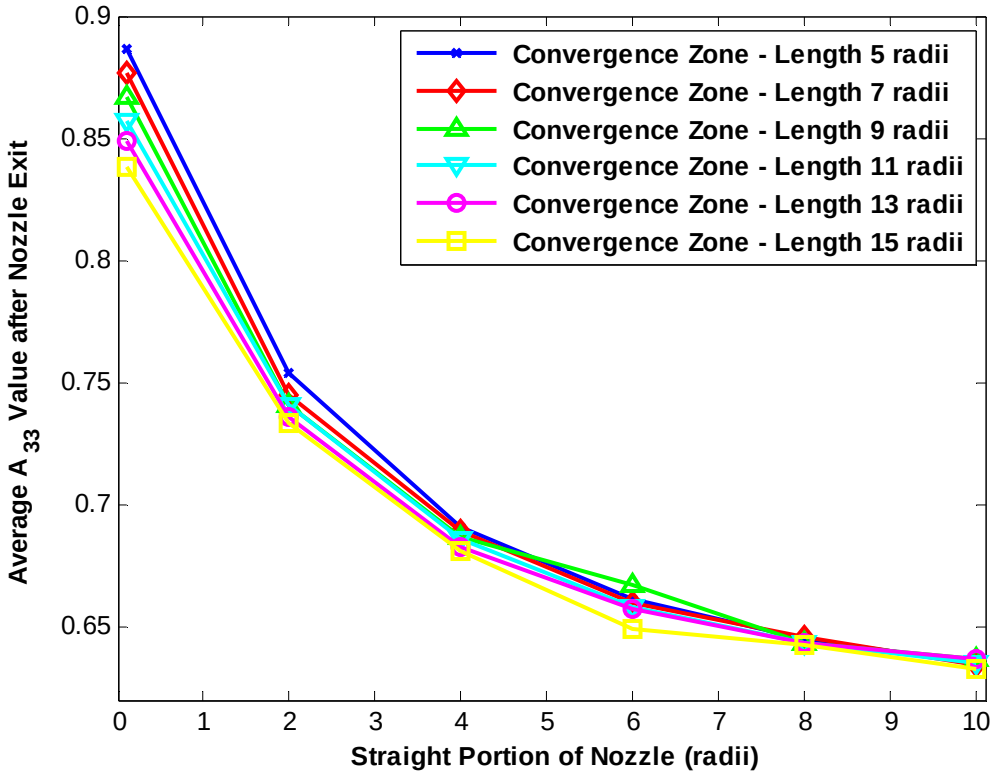

Figure 5.2. Average $\overline{A}_{33}$ Value Downstream of the Nozzle Exit for Values of A and B

Figure 5.2 shows that the average amount of fiber alignment in the direction of the flow can be altered with the A and B geometry parameters. The effect of changing the length of the nozzle convergence zone is seen to be little in comparison to changing the length of the straight portion of the nozzle. This is due to the effects discussed in Chapter Four for each of the zones in the nozzle geometry. Increasing the length of the convergence zone increases fiber alignment due to elongation flow in the z-direction. Figure 5.2 shows that the alignment of the fibers downstream of the nozzle exit is high for all convergence zone lengths in the study and little variation is seen as the nozzle length is changed. These results show that the fiber alignment is only slightly affected by convergence zone length. Figure 5.2 also shows that the length of the straight portion of the nozzle has a significant effect on the fiber alignment in the polymer melt. Fiber alignment along the direction of flow decreases considerably as the straight portion of the tube is increased. This effect is due to the lack of velocity gradients in the straight portion of the nozzle. The pure shear flow which is dominant in the straight section of the nozzle directs the fibers towards their pure shear steady state fiber orientation as calculated in section 4.3.2. Indeed, if the straight portion of the nozzle was made to be long enough, the pure shear steady state A_{33} value of 0.799 found in section 4.3.2 would be reached. By analyzing the slope of the plots in Figure 5.2, it can be seen that the length of the straight portion of the nozzle is approaching the pure shear steady state value.

The fiber alignment is decreased in the extrudate swell for all upstream geometry changes; therefore, the $\bar{A}_{33}$ value immediately before the nozzle exit will dictate the orientation state in the extruded bead. Changes in the nozzle geometry upstream from the nozzle exit are seen to change the fiber alignment before the nozzle exit, and thus the

values of $\bar{A}_{33}$ in Figure 5.2. In addition, Figure 5.2 indicates that a maximum $\bar{A}_{33}$ is obtained with the nozzle exit being at the end of the convergence zone with no straight portion present. For this study a long straight portion in which the orientation state returns to the pure shear steady state gives the minimum fiber alignment in the direction flow.

Nozzle geometries that result in a maximum and minimum fiber alignment are further discussed to provide an increased understanding of nozzle geometry effects on the fiber orientation. The nozzle geometry that provides a maximum fiber alignment in Figure 5.2 has A = 5 radii and B = 0.1 radii. The geometry and streamlines for this flow appear in Figure 5.3.

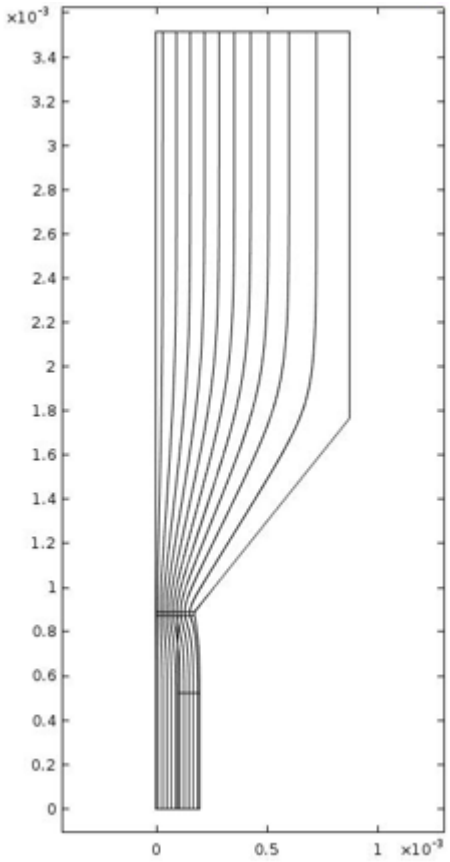

Figure 5.3. Geometry and Streamlines for Maximum Fiber Alignment Model, Dimensions in Meters (m)

Figure 5.4 shows the A_{33} component along the 10 streamlines described in Chapter Four for the nozzle geometry having A = 5 radii and B = 0.1 radii that yielded the maximum $\bar{A}_{33}$. In Figure 5.4, **CZS** indicates the beginning of the convergence zone of the nozzle, **CZE** shows the end of the convergence zone, and **NE** is at the location of the extrusion nozzle exit.

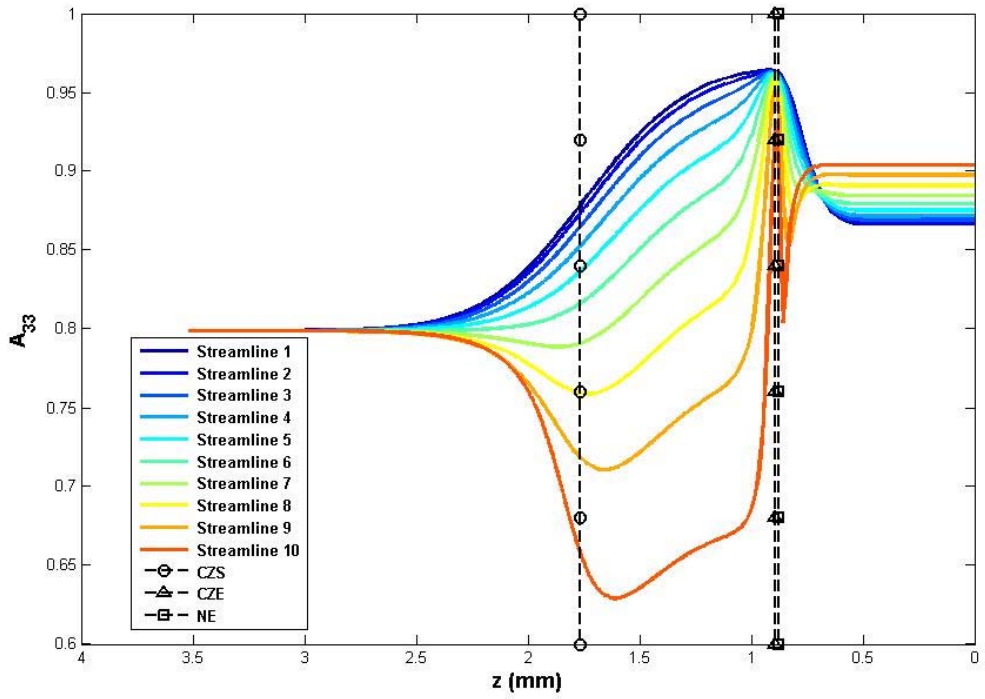

Figure 5.4. A_{33} Component of the Orientation Tensor **A** along All Streamlines for Maximum Fiber Alignment Model

Figure 5.4 shows similar effects as those discussed in Chapter Four. The elongation flow in the convergence zone increases the fiber alignment to a value near unity. The decrease in the fiber alignment seen along streamlines 7-10 is due to the contraction flow where fluid travels inward towards the centerline of the nozzle. This causes the fibers to align more transverse to the flow direction, decreasing the A_{33}

component. The decrease in fiber alignment seen along streamlines 7-10, is greater for the geometry defined by this set of parameters than that computed for the geometry evaluated in Chapter Four, where A = 5 and B = 10. This decrease results from the shorter convergence zone in the earlier simulation than that considered here. At the nozzle exit, **NE**, in Figure 5.4, the decrease in fiber alignment due to the expansion flow in the extrudate swell is still evident in this nozzle design, however, fiber alignment remains high due to the short straight section of the nozzle. The average $\bar{A}_{33}$ value at steady state downstream of the nozzle exit is $\bar{A}_{33}$ = 0.886, which indicates a very high alignment of fibers in the polymer bead.

The nozzle geometry which yields the minimum fiber alignment (i.e. the geometry defined by A = 5 and B = 10) is also considered here for further analysis. The values for the minimum fiber alignment are very close for all values of B. However, to provide a better comparison between the minimum and maximum fiber alignment cases, the convergence zone length A was chosen to be the same as that for the nozzle geometry giving the maximum fiber alignment. The geometry and streamlines for the minimum fiber alignment model are shown in Figure 5.5.

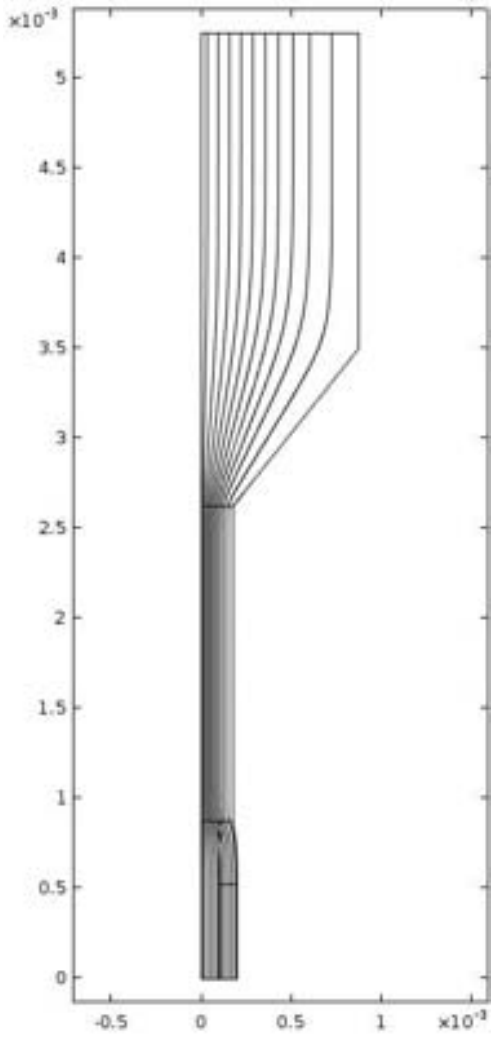

Figure 5.5. Geometry and Streamlines for Minimum Fiber Alignment Model, Dimensions in Meters (m)

Figure 5.6 shows the effects of the nozzle geometry and extrudate swell for the maximum fiber alignment model. In Figure 5.6, **CZS** represents the beginning of the convergence zone of the nozzle, **CZE** represents the end of the convergence zone, and **NE** represents the extrusion nozzle exit.

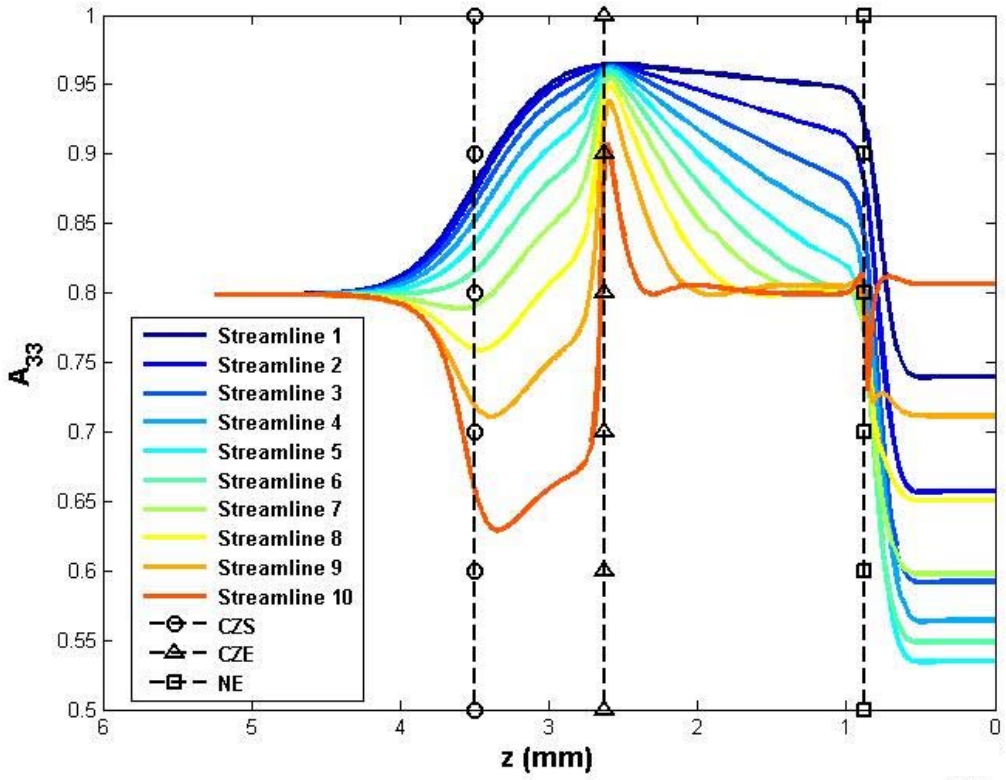

Figure 5.6. A_{33} Component of the Orientation Tensor **A** along All Streamlines for Minimum Fiber Alignment Model

Figure 5.6 shows similar effects to those discussed for the maximum fiber alignment case. The effects seen on the fiber alignment from the inlet to **CZE** are exactly the same as those discussed for Figure 5.4 and do not need to be repeated. The flow field from **CZE** to **NE** is defined by the straight portion of the nozzle. There is a decrease in fiber alignment seen in the straight portion of the nozzle between **CZE** and **NE**. This decrease is due to the lack of velocity gradients in the straight portion of the nozzle and a pure shear driven flow. The fibers begin to return to the pure shear steady state fiber orientation discussed in Section 4.3.2. At the nozzle exit, **NE** in Figure 5.6, the expansion flow in the extrudate swell causes a further decrease in the fiber alignment from the

straight portion of the nozzle. The average A_{33} value at steady state after the nozzle exit is calculated as, $\bar{A}_{33} = 0.635$, which defines a highly aligned fiber filled polymer bead.

The parametric study of the convergence zone length (A) and the length of the straight portion of the nozzle (B) shows that the fiber alignment can be changed by changing the upstream nozzle geometry. It was seen that the length of the straight portion of the nozzle has a larger effect on the fiber alignment that the convergence zone length and will return the fiber orientation to pure shear steady state if it is made to be long enough.

5.2.2 Parametric Study of Nozzle Exit Shape

The second parametric study of the nozzle includes the amount of nozzle exit expansion (C) and the length of the nozzle exit expansion (D). A maximum nozzle expansion angle that is expected to return a correct result was defined by calculating the slope tanget to the extrudate swell surface. The derivative of the fourth order polynomial defining the extrudate swell free surface was calculated at the extrudate swell start to find the slope of the tangent line. The maximum nozzle expansion angle is then calculated as the inverse tangent of the tangent line slope. The maximum nozzle expansion was found to be 13.65 degrees. The reason for defining the maximum nozzle expansion is to ensure that the fluid is not pulling away from the nozzle wall. Our model does not include the calculation of capillary effects; therefore, large expansion values could cause issues in the finite element calculation if the expansion was too great and the fluid pulled away from the nozzle wall. Four of the six expansion values (C) were set inside this angle for the smallest expansion length (D) and the other two were set slightly above. These variables are calculated with a set minimum A and B combination from the previous studies. The

values chosen are again A = 5 and B = 10 to provide an accurate comparison. The values for the new variables used in this study are

$$C = 1.025, 1.05, 1.075, 1.1, 1.125, and\ 1.15\ radii$$
$$D = 1, 2, and\ 3\ radii \tag{5.6}$$

This allows for eighteen different nozzle geometry tests to be run. The number of tests run for this parametric study was thirty-six originally to match the first parametric study, but for two results there existed numerical issues that stemmed from the Fast Exact Closure. The case when two eigenvalues are equal, which is mentioned in Chapter Four, occurred for the two inconsistent results and caused numerical issues. For this reason a smaller set of C and D values was created which contained only consistent and correct results. Results were found for all expansion values which means that the max expansion value is conservative and could be increased in future studies. The results of the parametric study of C and D are shown in Figure 5.7.

Figure 5.7 shows the effects of the amount of nozzle exit expansion (C) and the length of the nozzle exit expansion (D) on the average fiber alignment. There is little change in the average fiber alignment for the nozzle geometry changes defined by C and D. It is shown that the amount of nozzle exit expansion (C) has a greater effect on the average fiber alignment than the length of the nozzle expansion (D). Figure 5.7 shows that as the nozzle expansion increases the average fiber alignment decreases. This is because nozzle expansion introduces expansion flow inside the nozzle which has been shown to decrease fiber alignment. The nozzle expansion length (D) by itself can be compared to increasing the length of the straight portion of the nozzle (B). It is discussed in Section 5.2.1 that at a length of 10 radii the effect on fiber alignment of increasing the

straight portion length is beginning to plateau; therefore, it would take large values of (D) to show a significant decrease in the fiber alignment.

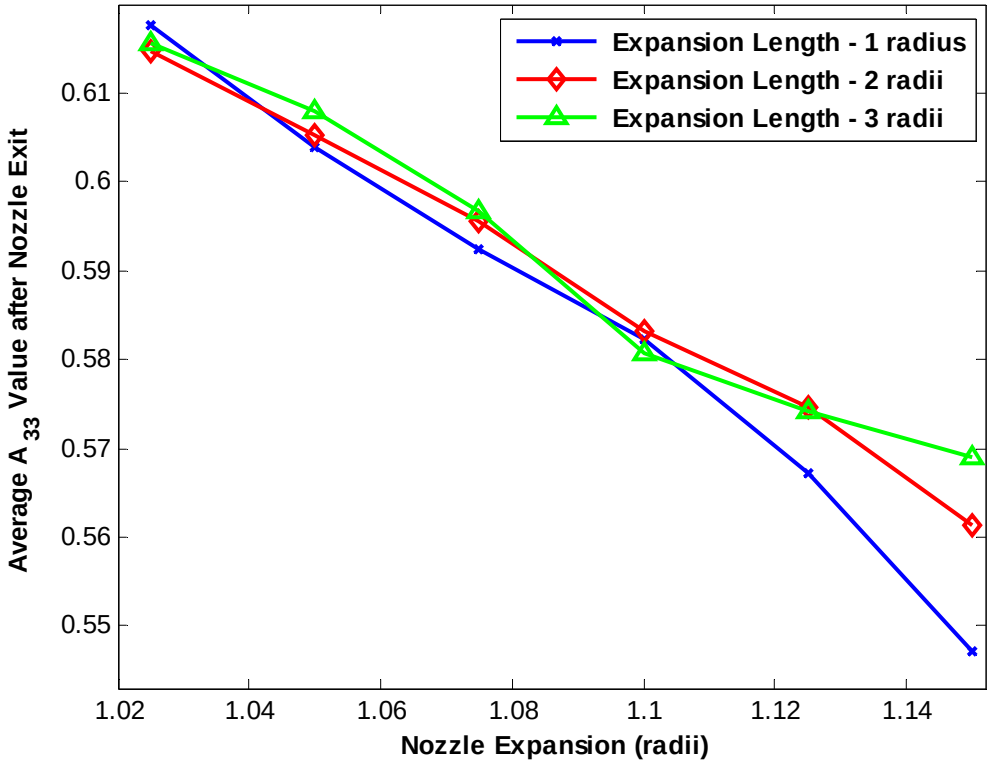

Figure 5.7. Average A_{33} Value after Nozzle Exit for Values of C and D

The maximum expansion and expansion length fiber alignment model is selected from Figure 5.7 as C = 1.15 radii and D = 10 radii. The values for the maximum expansion and expansion length are combined with the A and B values defining the minimum orientation from section 5.2.1. The geometry and streamlines for the maximum expansion fiber alignment model are shown in Figure 5.8.

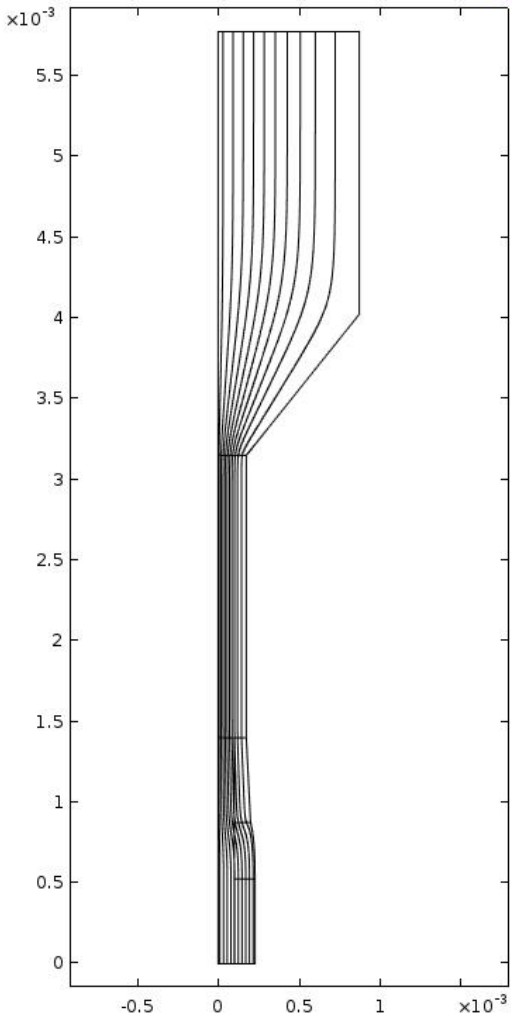

Figure 5.8. Geometry and Streamlines for Minimum Fiber Alignment Model, Dimensions in Meters (m)

Figure 5.9 shows the effects of the nozzle geometry and extrudate swell for the maximum fiber alignment model. In Figure 5.9, **CZS** represents the beginning of the convergence zone of the nozzle, **CZE** represents the end of the convergence zone, **STE** represents the straight tube end, and **NE** represents the extrusion nozzle exit.

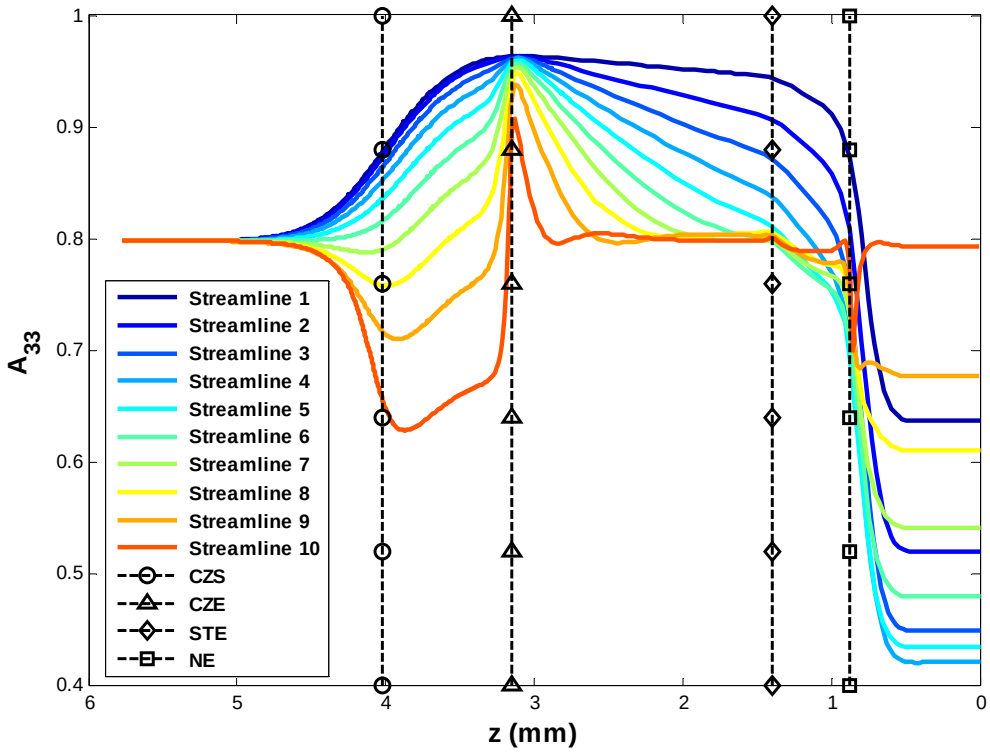

Figure 5.9. A_{33} Component of the Orientation Tensor **A** along All Streamlines for Maximum Expansion and Expansion Length Fiber Alignment Model

Figure 5.9 shows similar effects to those discussed for the minimum fiber alignment case. The effects seen on the fiber alignment from the inlet to **STE** are exactly the same as those discussed for Figure 5.6 and do not need to be repeated. The flow field from **STE** to **NE** is defined by the nozzle expansion. There is a decrease in fiber alignment seen in the nozzle expansion between **STE** to **NE**. This decrease in fiber alignment is due to the introduction of expansion flow in the nozzle. The expansion flow immediately after the nozzle exit in the extrudate swell further decreases the fiber alignment. The average A_{33} value for the maximum nozzle expansion and nozzle expansion length is calculated as $\bar{A}_{33} = 0.5689$.

The parametric study of the nozzle expansion (C) and the nozzle expansion length (D) shows that the fiber alignment can be changed by changing the geometry immediately before the nozzle exit. It was seen that the nozzle expansion has a larger effect on the fiber alignment than the nozzle expansion length. Larger expansion values could further decrease the fiber alignment, but a model for the capillary effect of the fluid being extruded would be needed to ensure the fluid could pull away from the wall at an expansion value that is too large.

The parametric studies show that the nozzle geometry can be designed to produce a certain average fiber orientation. This is an important result that can be used to increase the number of moldable parameters used in FDM printing for the optimization of FDM printed part structure.

CHAPTER SIX

Conclusions and Future Work

6.1 Conclusions

Fused deposition modeling technology is a popular additive manufacturing technique in the three-dimensional printing industry, but some issues need to be addressed before FDM printing can be industrially viable, particularly as composites are introduced as a viable FDM material. Virgin polymers currently used for print material have relatively low mechanical properties such as strength, toughness, and stiffness. As is common in other plastic processing methods, the addition of discrete fibers to the virgin polymer increases these mechanical properties. The material properties of the discrete fiber composite will vary depending on the orientation state of the fibers; therefore, understanding the orientation state is critical to the use of discrete fiber composites in the FDM process. The calculation of fiber orientation is a well-known subject and has been studied extensively, particularly for injection molding and extrusion. However, research on fiber orientation in the complex geometry of a FDM printer nozzle is a new topic and no prior work has been found on predicting fiber orientation in the extrudate swell region of FDM nozzle flow.

The objective of this thesis is to increase the understanding of the fiber orientation of discrete fibers in a polymer melt extruded by an FDM printing nozzle. A secondary motivation is to define the fluid domain of a fused deposition modeling nozzle by calculating the extrudate swell surface of material exiting the FDM nozzle. In addition to

the previous two objectives the effect of the fluid domain on the orientation state of a fiber filled polymer melt is also evaluated. The final objective of the thesis is to analyze the effects of changing the nozzle geometry on the final fiber orientation state.

The first step in this research was to calculate the extrudate swell free surface extending from the nozzle exit to fully define the fluid domain. The calculation of the extrudate swell free surface was completed by minimizing the stress state along the free surface. This calculation was done for both a straight extrusion tube and an FDM nozzle geometry. The straight extrusion tube problem was solved for several polynomial and one exponential representation of the free surface. Results showed that the fourth and fifth order representations could repeatedly and accurately calculated the expected Newtonian swell of 13% (see Georgiou [29, 30] and Elwood [32]), and approximate the extrudate swell free surface as defined by minimizing the integrated free surface stress. The fourth order representation was then used to calculate the extrudate swell free surface for the FDM nozzle. The extrudate swell was calculated to be very close to the 13% swell given in literature varying at most by 0.29% which is within the range of values published by several authors [26, 27, 29, 30].

The second step was to calculate fiber orientation in the fluid domain which includes the nozzle geometry and extrudate swell regions. The fiber orientation was calculated using Advani-Tucker [10] orientation tensors with the Fast Exact Closure from Montgomery-Smith, et al. [17] assuming the Folgar-Tucker [7] isotropic rotary diffusion model for fiber-fiber interactions. The fiber orientation was found to be highly aligned for both the straight extrusion tube and for the FDM nozzle. The average orientation in the

flow direction for the straight extrusion tube is calculated as $\bar{A}_{33}$ = 0.6082, and for the FDM nozzle, the average orientation in the flow direction is $\bar{A}_{33}$ = 0.6612.

The last step was to study the effect of changing the FDM nozzle geometry. A parametric study was run by changing four variables (length of convergence zone, length of the straight portion, length of exit expansion, and percentage of exit expansion) to find a minimum and maximum fiber orientation state. The maximum fiber orientation state that was found was $\bar{A}_{33}$ = 0.8858 and the minimum orientation state that was found was $\bar{A}_{33}$ = 0.5689.

The analysis in this thesis was done using a code written in MATLAB (MathWorks, Inc., Natick, Massachusetts) that was used to control COMSOL Multiphysics through LiveLink. The MATLAB fmincon function was used to minimize the extrudate swell free surface stress which was calculated in COMSOL for each iteration. After the optimum extrudate swell free surface was calculated, the finite element problem would be run one more time in COMSOL. Streamlines were added in post processing and exported to a MATLAB code which then calculated the fiber orientation using a fourth order Runge-Kutta ODE solver. The average orientation was calculated using an expanded Simpsons 1/3 rule numerical integration technique in a MATLAB code that used a single point with the value of A_{33} in the post nozzle steady state region from each streamline.

The important findings of this thesis are:

- The 13% extrudate swell free surface can be defined by minimizing the integrated stress along the free surface boundary.
- The nozzle geometry and extrudate swell effect the fiber orientation in the extruded bead.

- Fiber alignment is shown to
  - Increase in the convergence zone due to elongation flow.
  - Decrease in the extrudate swell expansion and contraction flow.

- The nozzle geometry can be changed to provide different fiber alignment values for specific printing purposes.

- Fiber alignment is shown to
  - Be affected little by the convergence zone length and nozzle exit expansion length.
  - Decrease as the length of the straight portion of the nozzle and the nozzle exit expansion value increase.

6.2 Future Work

Modeling of the FDM printing process is a growing area of research that has many issues and opportunities for future study. Interlayer voids, interlayer adhesion, porosity interior to the printed strand, and several other issues need to be solved to increase the usefulness of fused deposition modeling printing as an industrial tool. The possibilities for future study are quite significant as well due to the many factors defining print quality that have yet to be studied.

In this thesis many assumptions were made to reduce the complexity of the problem and make this initial study feasible. There are many improvements that need to be made to the model presented here but the scope is large. In the future, the true effect of omitted variables will need to be studied to fully define the inherent behavior and also the possible uses of the FDM process.

The variables with respect to the flow field calculation have a large effect on the FDM process and need to be addressed before further modeling can be pursued. The effect of gravity and inertia on the extrudate swell has been studied by Mistoulis et al. [33], and is shown to have a large effect on the amount of extrudate swell seen at the

nozzle exit. The extrudate swell has been shown to affect the final fiber orientation state; therefore, changes in the extrudate swell are of great importance.

For this thesis, the fluid was defined as a Newtonian fluid, whereas ABS and other FDM print materials are viscoelastic polymers which behave much differently. Polymers are shear thinning materials; therefore, a large shear stress will change the local viscosity and the respective velocities and velocity gradients. Methods exist for the modeling of Non-Newtonian, including viscoelastic materials [5]; however, this work was outside of the scope of the given study.

The fiber orientation calculations were done using the velocities and velocity gradients of a virgin ABS that had a singular viscosity value as the fluid moves through the printing nozzle. This is a common practice, but does not fully define the fiber orientation problem. The viscosity of a fiber filled polymer is highly dependent on the current orientation state of the fibers filling the polymer making the use of a fully coupled calculation an important task. This dependent viscosity will again change the velocities and velocity gradients [42].

The problem presented in this thesis was also run as an isothermal fluid flow. This again is an acceptable simplification but does not fully define the problem. The filament feedstock begins as a fiber filled solid which is liquefied and extruded, but from the moment the plastic leaves the nozzle exit it begins cooling and hardening in the ambient conditions. The rate of cooling and the time required before the pliability of the molten polymer ceases to exist are of interest to those studying interlayer adhesion, delaminations, and warping. An understanding of the when the polymer solidifies will also give an idea when the fibers reach the final orientation state.

The modeling of the extrudate swell and fiber orientation can also be improved in future studies to improve accuracy and decrease computation time. To decrease computation time, it is of interest to apply a shape optimization to the extrudate swell free surface calculation. The current model relies completely on gradients calculated by MATLAB (MathWorks, Inc., Natick, Massachusetts) through fmincon by the finite difference method. Exact gradients and Hessians can be calculated for the flow problem considered, which can significantly increase the rate of convergence and decrease function calls and iterations to reach the minimum solution. This would also allow for the use of more points to define the boundary without becoming computationally inefficient.

Singular finite elements are discussed in the literature review, but are not used in the current study. The implementation of a different element type in a pre-packaged software such as COMSOL Multiphysics was not feasible for the given study. If a finite element code was written using MATLAB (MathWorks, Inc., Natick, Massachusetts) the singular finite elements could be employed [12, 13, 14]. This would minimize or completely remove the effects of singularities which proved to be problematic in the current study. Two singularities occurred in this study and affected the abilities of the stress minimization and fiber orientation calculations.

A planar and three dimensional model should be created for the FDM extrudate swell problem studied. The axisymmetric model is a good representation of the three dimensional model but the full three dimensional model may show some small differences. It would also be of interest to run a planar model of the extrudate swell problem. Mistoulis et al. [33] show values for both the axisymmetric model and the

planar model which would provide a good metric for the further validation of the model presented in this thesis.

A study of different fiber orientation models for this given problem would be of interest. The Folgar-Tucker IRD model is used in this thesis because it is what is understood to be used in most of the mold filling software such as MoldFlow and Moldex3D (Core Tech Systems Co., Ltd., Chupei City, Taiwan). The Folgar-Tucker IRD model is known to over predict the rate of alignment of fibers and there exists newer, arguably more accurate, fiber orientation models that may better define the final fiber orientation state in the printed strand [8, 36].

FDM printing is an exciting and wide open field of study that needs more work before it is perfected. Many ideas for future study have been presented here and will hopefully be accomplished for the purpose of improving a technology with great potential.

BIBLIOGRAPHY

[1] Chua, C.K., Leong, K. F., and Lim, C. S., *Rapid Prototyping: Principles and Applications in Manufacturing 2*. World Scientific Publishing Co., Inc., River Edge, New Jersey, 2003.

[2] 2014, "How Green Is My 3D Printer? Scientists Warn of Heavy Metal Pollution," http://3dprint.com/6388/green-3d-printing/ [Accessed: 29-Jun-2015]

[3] Love, L. J., Kunc, V., Rios, O., Duty, C. E., Elliot, A. M., The Importance of Carbon Fiber to Polymer Additive Manufacturing, *Journal of Materials Research, suppl. Focus Issue: The Materials Science of Additive Manufacturing*, **29**(17):1893-1898, 2014.

[4] Bibbo, M. A., Dinh, S. M., and Armstrong, R. C., Shear Flow Properties of Semiconcentrated Fiber Suspensions, *Journal of Rheology*, **29**(6): 905-929, 1985

[5] Quari, N., Kaci, A., Tahakourt, A., Chaouche, M., Rheological Behaviour of Fibre Suspensions in Non-Newtonian Fluids, *Journal of Applied Rheology*, **21**(5), 2011

[6] Dinh, S.M., Armstrong, R.C., A Rheological Equation of State for Semiconcentrated Fiber Suspensions, *Journal of Rheology*, **28**(3):207–227, 1984.

[7] Folgar, F.P., and Tucker III C.L., Orientation Behavior of Fibers in Concentrated Suspensions, *Journal of Reinforced Plastics and Composites*, **3**:98–119, 1984.

[8] Wang, J., O'Gara, J.F., Tucker III, C.L., An Objective Model for Slow Orientation Kinetics in Concentrated Fiber Suspensions: Theory and Rheological Evidence, *Journal of Rheology*, **52**(5):1179-1200, 2008.

[9] Jeffery, G.B., The Motion of Ellipsoidal Particles Immersed in a Viscous Fluid, *International Journal For Numerical Methods in Fluids*, **29**:363-371,1999.

[10] Advani, S.G. and Tucker III, C.L., The Use of Tensors to Describe and Predict Fiber Orientation in Short Fiber Composites. *Journal of Rheology*, **31**(8):751–784, 1987.

[11] Zhang, D., *Flow-Induced Micro- and Nano-Fiber Suspensions in Short-Fiber Reinforced Composite Materials Processing*, PhD thesis, University of Missouri, 2013.

[12] Georgiou, G.C., Olson, L.G., Schultz, W.W., and Sagan, S., A Singular Finite Element For Stokes Flow: The Stick Slip Problem, *International Journal For Numerical Methods in Fluids*, **9**:1353-1367, 1989.

[13] Georgiou, G.C., Olson, L.G., and Schultz, W.W., Singular Finite Elements for the Sudden-Expansion and the Die-Swell Problems, *International Journal For Numerical Methods in Fluids*, **10**:357-372, 1990.

[14] Finlayson, B.A., Using COMSOL Multiphysics to Model Viscoelastic Fluid Flow, *Proceedings of the COMSOL Users Conference (2006)*

[15] Nixon, J., Dryer, B., Lempert, I., and Bigio, I., Three Parameter Analysis of Fiber Orientation in Fused Deposition Modeling Geometries, *Proceedings of PPS-30(2014)*

[16] Nixon, J., Dryer, B., Lempert, I., and Bigio, I., Three Parameter Analysis of Fiber Orientation in Fused Deposition Modeling Geometries, *Proceedings of SPE ANTEC (2014)*

[17] Montgomery-Smith, S.J., D.A. Jack, and D.E. Smith. The Fast Exact Closure for Jeffery's Equation with Diffusion. *Journal of Non-Newtonian Fluid Mechanics*, **166**:343–353, 2011.

[18] Mohamed, O.A., Masood, S. H., Bhowmik, J.L. Optimization of Fused Deposition Modeling Process Parameters: A Review of Current Research and Future Prospects. *Advances in Manufacturing*, **3**(1):42-53, 2015.

[19] Tekinalp, H.L., Kunc, V., Velez-Garcia, G.M., Duty, C.E., Love, L.J., Naskar, A.K., Blue, C.A., and Ozcan, S., Highly Oriented Carbon Fiber-Polymer Composites via Additive Manufacturing, *Composites Science and Technology*, **105**:144-150, 2014.

[20] Thrimurthulu, K., Pandey, P.M., and Reddy, N.V., Optimum Part Deposition Orientation in Fused Deposition Modeling, *International Journal of Machine Tools & Manufacture*, **44:**585-594, 2004.

[21] Sood, A.K., Ohdar, R.K., and Hahapatra, S.S., Parametric Appraisal of Mechanical Property of Fused Deposition Modeling, *Materials and Design*, **31**:287-295, 2010.

[22] Nikzad, M., Masood, S.H., Sbarski, I., Thermo-mechanical Properties of a Highly Filled Polymeric Composites for Fused Deposition Modeling, *Materials and Design*, **30**:3448-3456, 2011.

[23] Zhong, W., Li, F., Zhang, Z., Song, L., and Li, Z., Short Fiber Reinforced Composites for Fused Deposition Modeling, *Materials Science and Engineering*, **A301**:125-130, 2001.

[24] Cintra J.S. and C.L. Tucker III. Orthotropic closure approximations for flow-induced fiber orientation, *Journal of Rheology*, **39**(6):1095-1122, 1995.

[25] Wong, A.C.Y, Factors Affecting Extrudate Swell and Melt Flow Rate, *Journal of Materials Processing Technology*, **79**:163-169, 1998.

[26] Tanner, R.I, A Theory of Die Swell, *Journal of Polymer Science: Part A-2*, **8:**2067-2078, 1970.

[27] Tanner, R.I, A Theory of Die Swell Revisited, *Journal of Non-Newtonian Fluid Mechanics*, **129**:85-87, 2005.

[28] Dealy, J.M., Wang, J., *Melt Rheology and its Applications in the Plastics Industry*, Springer Publishing Co., New York, New York, 2013.

[29] Georgiou, G.C., The Compressible Newtonian Extrudate Swell Problem, *International Journal For Numerical Methods in Fluids*, **20**:255-261, 1995.

[30] Georgiou, G.C., Boudouvis, A.G., Converged Solutions of the Newtonian Extrudate-Swell Problem, *International Journal For Numerical Methods in Fluids*, **29**:363-371, 1999.

[31] Reddy, K.R., Tanner, R.I., Finite Element Solution of Viscous Jet Flows with Surface Tension, *Journal of Computers and Fluids*, **6**:83-91, 1978.

[32] Elwood, K.R.J., Papanastasiou, T.C., and Wilkes, J.O., Three-Dimensional Streamlined Finite Elements: Design of Extrusion Dies, *International Journal for Numerical Methods in Fluids*, **14**:13-24, 1992.

[33] Mitsoulis, E., Georgiou, G.C., and Kountouriotis, Z., A Study of Various Factors Affecting Newtonian Extrudate Swell, *Computers & Fluids*, **57**:195-207, 2012.

[34] Einstein, A. Eine neue Bestimmung der Molekuldimensionen, *Annalen der Physik*, **19**:289-306,1896.

[35] Koch, D.L., A Model for Orientational Diffusion in Fiber Suspensions, *Physics of Fluids*, **7**(8):2086-2088, 1995.

[36] J.H. Phelps and C.L. Tucker III. An anisotropic rotary diffusion model for fiber orientation in short- and long fiber thermoplastics. *Journal of Non-Newtonian Fluid Mechanics*, **156**:165–176, 2009.

[37] Hand, G.L., Theory of Anisotropic Fluids*, Journal of Fluid Mechanics*, **13**:33-46, 1962.

[38] Lipscomb, G.G., Denn, M.M., Hur, D.U., and Boger, D., The Flow of Fiber Suspensions in Complex Geometries, *Journal of Non-Newtonian Fluid Mechanics*, **26**:297-325, 1988.

[39] V. Verleye and F. Dupret. Prediction of Fiber Orientation in Complex Injection Molded Parts*. Developments in Non-Newtonian Flows,* pages 139–163, 1993.

[40] Chung, D.H., and Kwon, T.H., Invariant-Based Optimal Fitting Closure Approximation for the Numerical Prediction of Flow-Induced Fiber Orientation, *Journal of Rheology*, **46**:169–194, 2002.

[41] Montgomery-Smith, S.J., Wei He, D.A. Jack, and D.E. Smith. Exact Tensor Closures for the Three Dimensional Jeffery's Equation. *Journal of Fluid Mechanics*, **680**:321–335, 2011.

[42] VerWeyst, B.E., Tucker, C.L., Fiber Suspensions in Complex Geometries: Flow-Orientation Coupling. *The Canadian Journal of Chemical Engineering*, **80**:1093–1106, 2002.

[43] Baloch, A., Webster, M.F., A Computer Simulation of Complex Flows of Fibre Suspensions, *Computers & Fluids*, **24**:135-151, 1995.

[44] Yasuda, K., Henmi, S., and Mori, N., Effects of Abrupt Expansion Geometries on Flow-Induced Fiber Orientation and Concentration Distributions in Slit Channel Flows of Fiber Suspensions, *Journal of Polymer Composites*, **26**(5):660-670, 2005.

[45] Montgomery-Smith, S, Jack, D.A., Smith, D.E., A systematic approach to obtaining numerical solutions of Jeffery's type equations using Spherical Harmonics, *Journal of Composites: Part A*, **41**:827-835, 2010.